METAL - ALUMINUM OXIDE INTERACTIONS: EFFECTS OF SURFACE HYDROXYLATION AND HIGH ELECTRIC FIELDS

Chengyu Niu, B.S., M.S.

Dissertation Prepared for the Degree of

DOCTOR OF PHILOSOPHY

UNIVERSITY OF NORTH TEXAS

December 2001

APPROVED:

Jeffry A. Kelber, Major Professor
Paul S. Braterman, Committee Member
Oliver M.R. Chyan, Committee Member
Teresa D. Golden, Committee Member
David A. Golden, Committee Member
Ruthanne D. Thomas, Chair of the Department of Chemistry
C. Neal Tate, Dean of the Robert B. Toulouse School of Graduate Studies

Niu, Chengyu, Metal-Aluminum Oxide Interactions: Effects of Surface Hydroxylation and High Electric Fields. Doctor of Philosophy (Chemistry), December 2001, 131 pp., 8 tables, 44 illustrations, reference list, 174 titles.

Metal and oxide interactions are of broad scientific and technological interest in areas such as heterogeneous catalysis, microelectronics, composite materials, and corrosion. In the real world, such interactions are often complicated by the presence of interfacial impurities and/or high electric fields that may change the thermodynamic and kinetic behaviors of the metal/oxide interfaces. This research includes: (1) the surface hydroxylation effects on the aluminum oxide interactions with copper adlayers, and (2) effects of high electric fields on the interface of thin aluminum oxide films and Ni_3Al substrate.

X-ray photoelectron spectroscopy (XPS) studies and first principles calculations have been carried out to compare copper adsorption on heavily hydroxylated α-$Al_2O_3(0001)$ with dehydroxylated surfaces produced by Argon ion sputtering followed by annealing in oxygen. For a heavily hydroxylated surface with OH coverage of 0.47 monolayer (ML), sputter deposition of copper at 300 K results in a maximum Cu(I) coverage of ~0.35 ML, in agreement with theoretical predictions. Maximum Cu(I) coverage at 300 K decreases with decreasing surface hydroxylation. Exposure of a partially dehydroxylated α-$Al_2O_3(0001)$ surface to either air or 2 Torr water vapor results in recovery of surface hydroxylation, which in turn increases the maximum Cu(I) coverage. The ability of surface hydroxyl groups to enhance copper binding suggests a

reason for contradictory experimental results reported in the literature for copper wetting of aluminum oxide.

Scanning tunneling microscopy (STM) was used to study the high electric field effects on thermally grown ultrathin Al_2O_3 and the interface of Al_2O_3 and Ni_3Al substrate. Under STM induced high electric fields, dielectric breakdown of thin Al_2O_3 occurs at 12.3 ± 1.0 MV/cm. At lower electric fields, small voids that are 2-8 Å deep are initiated at the oxide/metal interface and grow wider and deeper into the metal substrate, which eventually leads to either physical collapse or dielectric breakdown of the oxide film on top.

ACKNOWLEDGEMENTS

The author gratefully acknowledges Dr. Jeffry A. Kelber for his guidance. Special thanks are extended to Dr. Dwight R. Jennison and Dr. Noel P. Magtoto for informative discussions. Financial support for this research was provided by the Welch foundation, National Science Foundation, and the U.S. Department of Energy (Office of Basic Energy Sciences).

TABLE OF CONTENTS

Page

LIST OF TABLES

LIST OF ILLUSTRATIONS

Figure Page

CHAPTER 1

INTRODUCTION

Metal–oxide interaction is of broad scientific and technological interest in areas such as heterogeneous catalysis, microelectronics, composite materials, and corrosion. Most commercial catalysts consist of small metal particles supported on high-surface-area oxide powders, commonly SiO_2 and Al_2O_3 (1, 2). Metal-oxide interactions have direct effects on the mechanical stability and catalytic behaviors of metal catalysts (1, 3, 4). Metal-oxide interfacial behavior is also a critical concern in microelectronics. Metal peeling, interfacial charging and diffusion can easily lead to device failure (5, 6). Furthermore, most metal corrosion starts from the metal/oxide interface. Examples include iron, nickel, aluminum, chromium, and their alloys with other elements (7-11).

In the real world, metal-oxide interactions are often complicated by the existence of interface impurities resulting either from adsorption or from segregation. Such factors, from a thermodynamic point of view, will influence the interface free energy and can cause changes in morphology and the degree of wetting at the interface. Effects of some interface impurities, such as carbon (12) and sulfur (13-16), have been studied extensively. Surface hydroxylation, on the other hand, has not attracted much attention. Part of the reason is that it has not been generally realized that hydroxyl groups on certain oxide surfaces may persist in ultrahigh vacuum and at high annealing temperatures (17-19). In addition, specifically adsorbed ions (Cl^-, OH^-, H^+, etc.) can induce electric fields

greater than 1 MV/cm across a thin oxide film grown on a metal surface (20). However, to the knowledge of the author, high electric field effects on metal/oxide interface have not been systematically studied for most metal/oxide systems.

This study was intended to provide an in-depth understanding of surface hydroxylation and high electric field effects on the metal/oxide interactions. Aluminum oxide was selected because of its technological importance. This dissertation is divided into four chapters. The current chapter provides background information on the fundamental concepts of the metal/oxide interactions, and a review of surface analysis methods employed in this research. Chapter 2 presents experimental and theoretical studies of copper wetting of hydroxylated α-Al_2O_3(0001) surface. Chapter 3 is a description of dehydroxylation effects on copper interactions with the α-Al_2O_3(0001) surface. In Chapter 4, scanning tunneling microscopy (STM) is used to study the high electric field effects on well-ordered thin aluminum oxide film grown on Ni_3Al(111) surface.

1.1. FUNDAMENTAL CONCEPTS OF METAL/OXIDE INTERACTIONS

1.1.1. Types of Metal/Oxide Interface

Metal-on-oxide and oxide-on-metal systems are commonly found in heterogeneous catalysis, microelectronics, composite materials, and corrosion. In order for the metal phase and oxide phase to exist in contact, there must be a region through which the intensive properties of the system change from those of one phase to those of the other. Such a region is defined as the metal/oxide interface.

According to the nature of the reaction products formed when the metal and oxide are placed in contact, the metal/oxide interfaces can be classified as the following (12):

(1) *Abrupt interface*. No chemical reactions are involved during the formation of the interface, and the interface is characteristic with an abrupt change from one phase to the other. Cu/TiO_2 is a typical example (21, 22).

(2) *Intermetallic interface*. Metal alloy is formed at the interface, which can be represented with $R/M\text{-}R/MO_y$. At Aluminum NiO interface, a Ni_3Al layer is generally observed (23).

(3) *Oxide interface.* Redox reactions occurred between metal and oxide at the interface. The interface can be binary oxide, ternary oxide, and oxide solid solution. Examples are $Al/Al_2O_3/TiO_2$ (24), $Ni/NiAl_2O_4/Al_2O_3$ (25, 26), and Ni/MgO-NiO/MgO (27), respectively.

1.1.2. Metal Growth on Oxide

Metal growth on oxide substrates plays a key role in a vast array of technologically important applications, including novel structural materials based on metal/ceramic composites, metal/oxide contacts in microelectronics and photovoltaic devices, and oxide-supported transition metal catalysts (28). The atomic-level structure, the electronic characters, and the thermal stability of the supported metal and metal/oxide interface are critical issues that will affect parameters such as the hardness of the composite materials, the peel strength of metal/oxide contacts, the efficiency of photovoltaic devices, the speed

and size of microelectronics, the sensitivity and lifetime of sensors, and the catalytic activity and selectivity of oxide-supported particles or cations.

During metal growth on an oxide substrate, the energy change ($\Delta\gamma$) to form metal/oxide interface can be calculated using the following equation (12, 29):

$$\Delta\gamma = \gamma_m + \gamma_{m/ox} - \gamma_{ox} \qquad (1.1)$$

where $\gamma_{m/ox}$ is the metal/oxide interfacial energy, γ_m and γ_{ox} are surface energies of clean metal and oxide, respectively. Physically, equation 1.1 represents the free energy change by removing atoms from a metal island and placing it onto the oxide substrate to create new metal/oxide interface and metal surface area.

Depending on the value of $\Delta\gamma$, three metal growth modes can be predicted: (1) *Frank-van der Merwe (FM) mode*, where $\Delta\gamma < 0$ so that it is favorable for the metal overlayer to spread and wet the oxide surface, and metal film grows in a layer-by-layer manner; (2) *Volmer-Weber (VW) mode*, where the opposite is true and three dimensional (3D) islanding growth is preferred; and (3) *Stranski-Krastanov (SK) mode*, in which the first monolayer (or a few layers) completely wets the oxide, followed by formation of 3D islands. SK mode usually occurs in epitaxial systems that have large lattice misfit strain energies (12).

The term $\gamma_{m/ox}$ includes contribution from both interfacial chemical reactions and physical interactions. Since metals generally have greater surface energy than oxides (28), equation 1.1 requires a large and negative $\gamma_{m/ox}$ for metal wetting to occur ($\Delta\gamma < 0$). Physical interactions (electrostatic interactions and van der Waals forces) alone, however,

are often too weak to fulfill this requirement. Thus metal wetting of an oxide surface is typically accompanied by charge transfer from metal to the substrate (30).

To determine what interfacial products might exist, the first step is to find out what bulk phases should form if the metal and the oxide are to react. Take the reaction in (1.2) as an example,

$$MO + R \rightarrow M + RO \qquad (1.2)$$

if this reaction would result in a negative free energy change, metal M should reduce the surface of RO to metallic R and itself become oxidized to MO. Since the formation entropies of oxides are usually negligible (31), reaction (1.2) can be predicted if the standard heat of formation of RO is less negative than that of MO. Some oxide substrates can be readily reduced to a lower oxide. $2TiO_2 \rightarrow Ti_2O_3 + ½\ O_2$ is a typical example. Then the following reaction must be taken into consideration

$$M + 2TiO_2 \rightarrow MO + Ti_2O_3 \qquad (1.3)$$

which has been reported in multiple papers (32-36). Intermetallic compounds (23, 37, 38) and mixed oxides (27) are also possible interfacial reaction products. Due to kinetic limitations, experiments carried out at room temperature may not result in the thermodynamically expected bulk phases. Such limitations include activation barriers for the chemical reactions and lateral diffusion. However, when only diffusion limitations exist, the thermodynamically stable phases can still be observed in the thin interfacial layers (35, 37, 38).

During a typical vapor deposition, the first important step is the adsorption of the incoming metal atoms onto the oxide surface. Previous studies have shown that at room

temperature initial sticking coefficient of any metal is close to 1 (28, 39). However, at higher substrate temperature, a sticking coefficient less than 1 may be obtained due to re-evaporation (i.e. desorption) of metal atoms from the surface.

After adsorption, the metal atoms can move across the oxide surface at an average speed (***S***) depending on their diffusion coefficient (***D***):

$$\boldsymbol{S} = 4\boldsymbol{D}/a \qquad (1.4)$$

$$\boldsymbol{D} = \tfrac{1}{4}(\nu_0\, \alpha^2) \exp(-\varepsilon_{Diff}/kT) \qquad (1.5)$$

where ε_{Diff} is the activation energy for diffusion, ν_0 is the pre-factor, α is the distance between two adjacent adsorption sites, T is the temperature in Kelvin, and k is the Boltzmann constant.

With defects present on the surface, the metal atoms may be trapped at these sites to form nuclei for subsequent growth. This process is called *heterogeneous nucleation*. For example, if the adatom diffusion lengths are long compared to the mean terrace width on an oxide surface, adatom condensation will occur preferentially at steps rather than on terraces. Step-flow growth is a specialized sub case of the above in which there is preferential adatom attachment from lower terraces adjacent to steps. Step flow leads to step-step annihilation and a gradual reduction in step density with increasing film thickness. In contrast to the heterogeneous nucleation, *homogeneous nucleation* refers to the formation of stable nuclei by aggregation of several adatoms on regular surface sites. After reaching the maximum density of surface nuclei (saturation nuclei density), only growth processes occur, i.e. all diffusing adatoms are captured by existing islands (either 2- or 3-dimensional). The growth mode thereafter can be determined using equation 1.1.

1.1.3. Oxide Growth on Metal Substrates

The oxidizing properties of the atmospheric environment cause the vast majority of all "real-world" metals to be covered by a thin native oxide film. In most cases, it is this oxide skin that governs the surface reactivity of the metal rather than the surface properties of the metal itself. Thin native oxides strongly influence the lubricating properties of metals (40) as well as the adhesion of plastic coatings (41). Oxide films can also be exploited as protective coatings on metal (42). Al and Al alloys owe their corrosion resistance to a thin amorphous Al_2O_3 layer grown naturally on the metal surface (43).

In an oxidation process, the reactants, a metal having delocalized bonding and an oxidizing regent having covalent bonding, are converted into a compound, i.e., an oxide having partially ionic, partially covalent bonding. Because most metal oxides are solids, if the oxide products remain on the metal surface, the two reactants will be separated. Further oxide growth requires that a species of metal and/or oxidant dissolves in and moves through the growing oxide to continue the reaction.

Depending on the metal and time-temperature-pressure relationship during oxidation, the oxidation processes can be divided into two categories, high-temperature vs. low-temperature oxidation. The products of high-temperature oxidation are often polycrystalline and contain paths (grain boundaries) for easy ion diffusion. In high-temperature oxidation, thermal energy is sufficient for ion generation and movement through the oxide even though a small electric field may be present. A parabolic growth

rate is generally followed. In low-temperature oxidation, the thermal energy is not enough to allow existing ions or electrons (or holes) to surmount the energy barrier and therefore, the driving force for the formation of oxides is an electric field (42). A logarithmic growth rate is typical for this case. The actual temperature of transition from low- to high-temperature oxidation is a function of the material, its perfection, and purity. Single crystal and amorphous metal differ from polycrystalline in that no grain boundaries are present. Impurities often concentrate at grain boundaries, leading to defect regions in the oxide grown from polycrystalline metal. These regions provide paths for easy ion movement and thus, fast oxide growth. Single crystal and amorphous metals minimize such defects and should, therefore, produce higher quality oxides that result in a slower rate of oxidation (44).

According to Wagner's oxidation theory (42, 45), the growth of oxide films obey a parabolic kinetics

$$x^2 = k_p t \qquad (1.6)$$

where x is the film thickness and k_p the parabolic rate constant. The parabolic kinetics is consistent with the rate of growth being controlled by transport down a gradient of driving force, which becomes proportionally smaller as the film thickness increases. The species being transported during oxide growth include ions and electrons or holes. In the presence of an electric field, the current $\boldsymbol{J}_i$ of mobile particles becomes

$$\boldsymbol{J}_i = -\boldsymbol{D}_i \frac{\partial \boldsymbol{C}_i(x,t)}{\partial x} + \mu_i \boldsymbol{E} \boldsymbol{C}_i(x,t), \qquad (1.7)$$

where $\boldsymbol{E}$ is the electric field and μ_i is the mobility of the charged species related to the diffusion coefficient $\boldsymbol{D}$i by the Einstein relationship (42):

$$Ze\boldsymbol{D}_i = \boldsymbol{\mu}_i kT \qquad (1.8)$$

The electric field developed during film growth can be regarded as arising from diffusion of opposite charges within the oxide. If metal ions are more mobile in the oxide than oxygen ions, new oxide is formed at the oxide/oxygen interface. Since electrons have a higher mobility than the metal ions and therefore, an electric field will develop to speed up the ions and slow down the electrons until the electric currents carried by the two types of charged particles are equal. Thus, the oxide/gas interface develops a negative electrical potential with respect to the oxide/metal interface. The same is true if the film grow mainly by diffusion of oxygen ions.

Oxide films can be grown by oxidation of a metal single crystal or by evaporation (MBE) of a metal on an inert metallic substrate in the presence of oxygen. The lattice constant of the inert substrate has to be chosen properly in order to prepare a less strained layer with long-range order. A third technique is based on the oxidation of alloy surfaces. Most of the recent studies were performed by oxidation of surfaces of binary intermetallic alloys like NiAl (46-51), FeAl (52) and CoGa (53, 54) as substrates. The oxide layers grow after adsorption of oxygen and the preferential segregation of one of the metallic components (Al, Ga) at the surface. In general, adsorption of oxygen at room temperature leads to the formation of amorphous oxide layers. Subsequent annealing to elevated temperatures orders the oxide films. One of the advantages of using alloys as substrate is that higher annealing temperatures can be used for ordering of the oxide films without melting of the substrate. Very often the temperature of the ordering of an oxide film is much higher as the melting temperature of the pure metal. This is crucially

important for ordering the grown oxide layers. Of course, if there is a large mismatch between the alloy surface and the oxide lattice constants, the film may be defect rich.

1.2. EXPERIMENTAL ASPECTS

Various surface analysis techniques were used in this study: Low-Energy Electron Diffraction (LEED) and Scanning Tunneling Microscopy (STM) were used to determine the surface structure and topography; Auger Electron Spectroscopy (AES) and X-Ray Photoelectron Spectroscopy (XPS) were employed in surface composition analysis; and Scanning Tunneling Spectroscopy (STS) was applied in the study of surface electronic states. The following is a brief review of these widely used surface and interface analysis methods.

1.2.1. X-Ray Photoelectron Spectroscopy (XPS)

The excitation process of photoelectrons is illustrated in Fig. 1.1. When a beam of light strikes a surface, photons are absorbed by surface atoms, leading to ionization and the emission of core (inner shell) electrons. The ejected photoelectrons have a kinetic energy $\mathbf{E}_{kin}$ equal to

$$\mathbf{E}_{kin} = h\nu - \mathbf{E}_{B} \qquad (1.9)$$

where *hν* is the energy of the incident X-rays, and $\mathbf{E}_B$ is the binding energy of core level electrons, or energy required to just remove the electron concerned from its initial level to the vacuum level. The photoemission process is inelastic if the photoelectron suffers an energy loss between emission from an atom in a solid sample and detection in the spectrometer (55). Because most photoelectrons are emitted inelastically, the photoelectron peaks shift to the lower kinetic energy side. This effect requires a correction term Φ for equation 1.9 (56), which is usually determined experimentally.

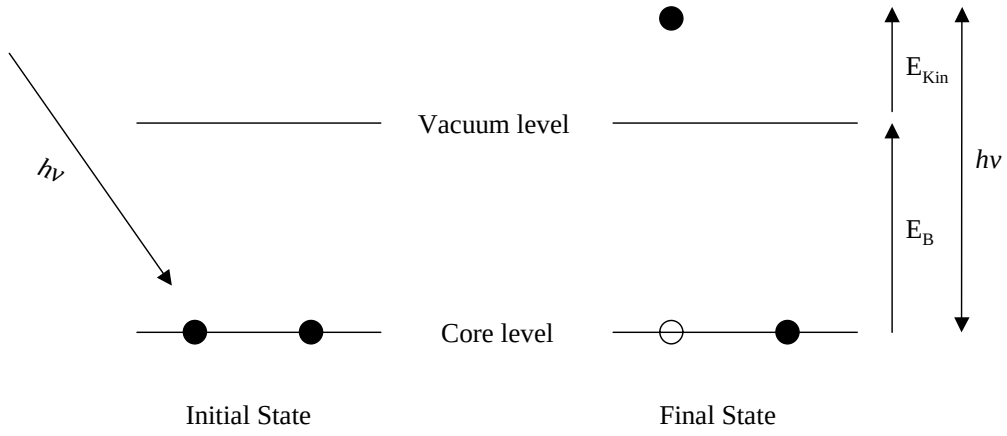

Figure 1.1. Excitation of photoelectrons: a "photon in/electron out" process. Part of the photon energy is used to overcome the electron binding energy, the remaining is transferred to kinetic energy of the photoelectron.

Fig. 1.2 shows the equipment setup for a typical X-ray photoelectron spectrometer. The X-ray source consists of an anode of a suitable material which is bombarded by energetic electrons that are emitted from the cathode. The X-ray radiation can be made monochromatic by using the characteristic emission lines of the anode material. Mg and

Al are commonly used anodes which result in soft X-ray lines with energy of 1253.6 and 1486.6 eV, respectively (57). The emitted photoelectrons will therefore have kinetic energies in the range of 0 - 1250 eV or 0 - 1480 eV. Since such electrons have very short inelastic mean free path (IMFP) in solids, only those that are very close to the surface can be ejected from the sample. Energy-dispersive analysis of the emitted photoelectrons

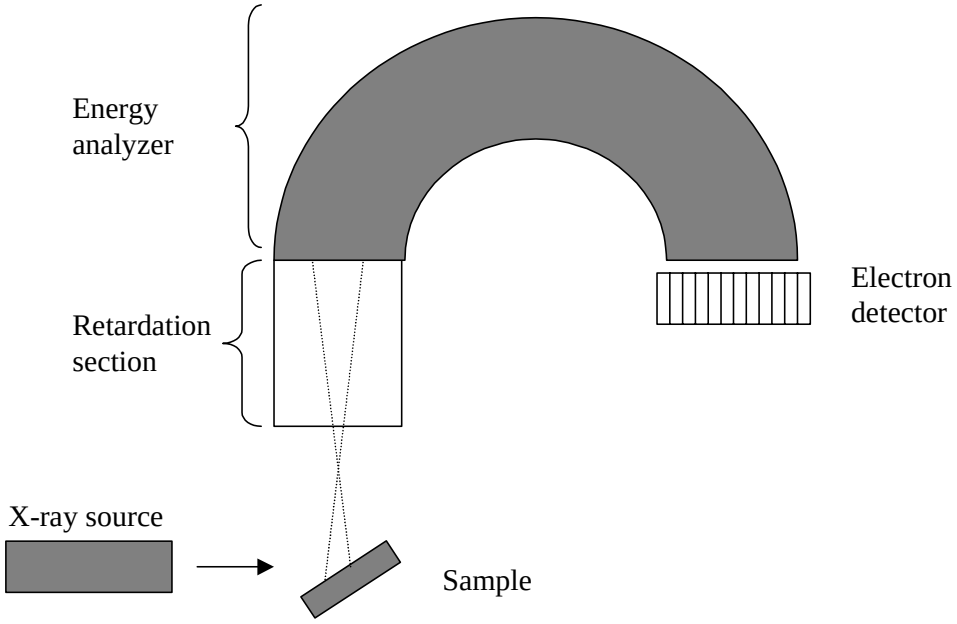

Figure 1.2. Schematic drawing of a X-ray photoelectron spectrometer.

provides information of the surface composition and electronic states. For each and every element, there will be a characteristic binding energy associated with each core atomic orbital. In other words, each element will give rise to a characteristic set of peaks in the photoelectron spectrum at kinetic energies determined by the photon energy and the respective binding energies. The presence of peaks at particular energies therefore indicates the presence of a specific element in the sample under study. In addition, the

intensity of the peaks is proportional to the concentration of the element within the sampled region.

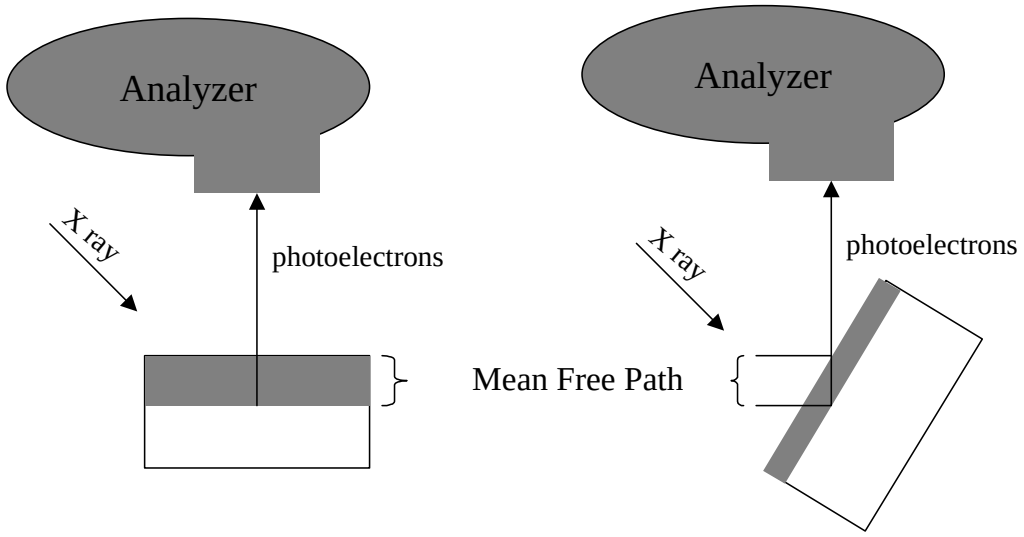

Figure 1.3. Different sampling depth in XPS can be achieved by collecting photoelectrons emitted at different emission angles to the surface plane.

The exact binding energy of an electron depends not only upon the level from which photoemission is occurring, but also upon the formal oxidation state of the atom and the local chemical and physical environment. Changes in either of them give rise to small shifts in the peak positions in the spectrum. This effect is called *the chemical shift*. Such shifts are readily observable and interpretable in XP spectra because the XPS technique is of high intrinsic resolution and is a one-electron process. Atoms of a higher positive oxidation state exhibit a higher binding energy due to the extra coulombic interaction between the photo-emitted electron and the ion core. This ability to

discriminate between different oxidation states and chemical environments is one of the major strengths of the XPS technique.

XPS also has the ability to perform non-destructive analysis of the variation of surface composition with depth (with chemical state specificity). For photoelectrons with certain initial energy, the inelastic mean free path (IMFP) within the solid sample is a constant. However, as shown in Fig. 1.3, the effective sampling depth of the analyzer is decreased if the angle between the sample surface normal and analyzer axis increases. In turn, the degree of surface sensitivity is increased. This technique is called Angle Resolved XPS (or grazing incidence XPS).

1.2.2. Auger Electron Spectroscopy (AES)

Auger Electron Spectroscopy (AES) is one of the most commonly employed surface analytical techniques to determine the composition of the surface layers of a sample. Auger spectroscopy involves three steps: atomic ionization (core level electron ejection), Auger electron emission, and analysis of the emitted Auger electrons.

Fig. 1.4 illustrates a typical Auger process. A beam of high-energy electrons impact the sample surface and causes the excitation of core level electrons; the departure of a core electron leaves behind a core hole in the atom; a electron falls from a higher level to fill the core hole; the energy liberated in this relaxation process is simultaneously transferred to a second electron at a higher level; this second electron uses a fraction of the transferred energy to overcome the binding energy, and the reminder becomes kinetic energy of the emitted Auger electron. We use $KL_1L_{2,3}$ to describe the above transition,

where the initial hole location is given first, followed by the locations of the final two holes in order of decreasing binding energy.

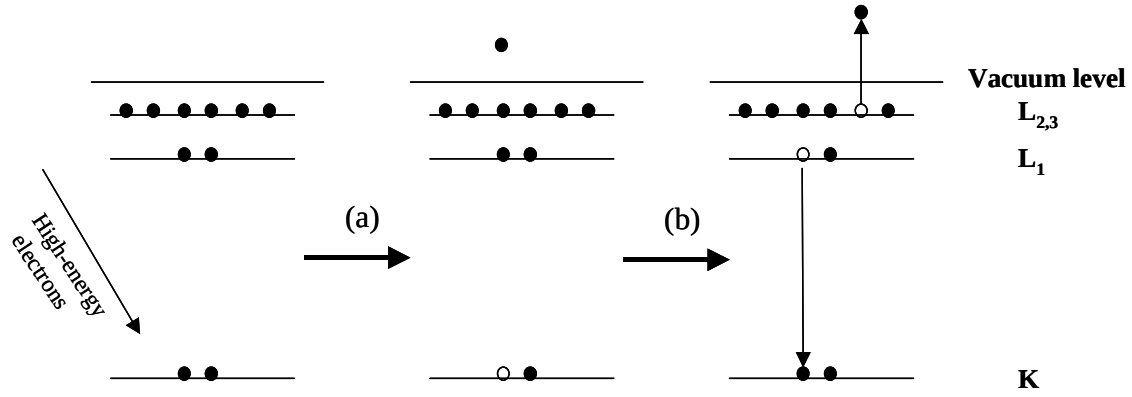

Figure 1.4. A typical Auger process: (a) ejection of a core level electron leaves behind a core hole; (b) a higher level electron fills the core hole, the relaxation energy is transferred to a second electron which is emitted as an Auger electron.

The kinetic energy (E_{kin}) of Auger electrons in the above example can be estimated using

$$E_{kin} = (E_K - E_{L1}) - E_{L2,3} \qquad (1.10)$$

where E_K, E_{L1}, and $E_{L2,3}$ are electron energy at K, L_1, and $L_{2,3}$ levels, respectively. Note that E_{kin} is independent of the formation mechanism of the initial core hole. So X-ray can also be used to induce Auger electrons.

Auger spectroscopy is based on the measurement of emitted electrons at different kinetic energies (Auger spectrum). Since the initial ionization is non-selective and the initial hole may be in various shells, there will be many possible Auger transitions for a

given element. It is a general practice that the Auger spectra being analyzed in a differentiated form. Because each element has its own unique set of binding energies, Auger electron spectroscopy can be used to determine the elemental composition of a given sample surface. The surface concentration of an element can also be derived from the peak-to-peak height in the derivatized Auger spectrum. Furthermore, chemical shift effect (see section 1.2.1) will be reflected in variations in peak shapes (fine structure), and can be used to obtain information pertaining to the chemical environment of the interested elements.

1.2.3. Low Energy Electron Diffraction (LEED)

According to the principles of wave-particle duality, a beam of electrons is also a succession of electron waves. Using de Broglie relation, the wavelength of the electrons (λ_e) can be expressed as (58):

$$\lambda_e\,(\text{Å}) = \sqrt{150 / E(eV)} \qquad (1.11)$$

In order for the atomic diffraction condition (λ not longer than interatomic spacing) to be satisfied, electrons with energies as low as 10 to 200 eV are needed.

Consider the scattering of an electron beam coming to a single crystal from surface normal direction (Fig. 1.5). For two adjacent atoms, there is a difference ($\delta = a \sin\theta$) in the distance the scattered radiation has to travel to the detector at a certain angle θ. This path difference must equal to an integral number of wavelengths for constructive interference to occur when the scattered beams eventually meet at the detector, i.e.

$$a \sin\theta = n \lambda_e \qquad (1.12)$$

which is known as Bragg condition (59). For a surface with two-dimensional array of atoms with primitive interatomic distance of *a* and *b*, Bragg condition requires both $a\sin\theta_a = n\,\lambda_e$ and $b\sin\theta_b = m\,\lambda_e$ for constructive interference to occur, i.e. the incoming electrons can only be scattered along a set of lines dispersed from the surface (60, 61).

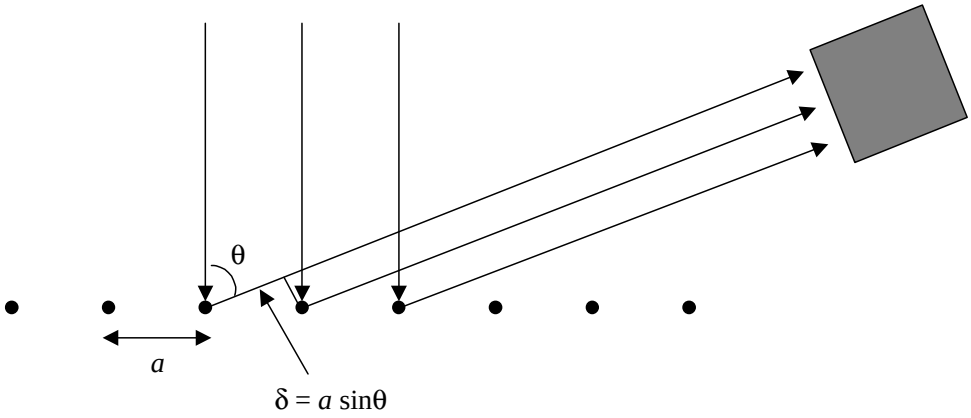

Figure 1.5. Diffraction of electrons from a one-dimension chain of atoms. Constructive interference requires $\delta = n\,\lambda_e$.

In a LEED experiment, a beam of electrons with specific energy (20 to 200 eV) is directed toward the sample surface, where a fraction of the incoming low energy electrons is elastically scattered (Fig. 1.6). To prevent the interference of the inelastically scattered electrons, a set of hemispherical retarding grids are used to filter out these background electrons. After passing through the retarding grids, the elastically scattered (diffracted) electrons are accelerated onto a fluorescent screen by a positive bias. Bombardment of diffracted electrons onto the screen results in bright spots whose pattern reflects the ordered arrangement of surface atoms by reciprocal relationship (59).

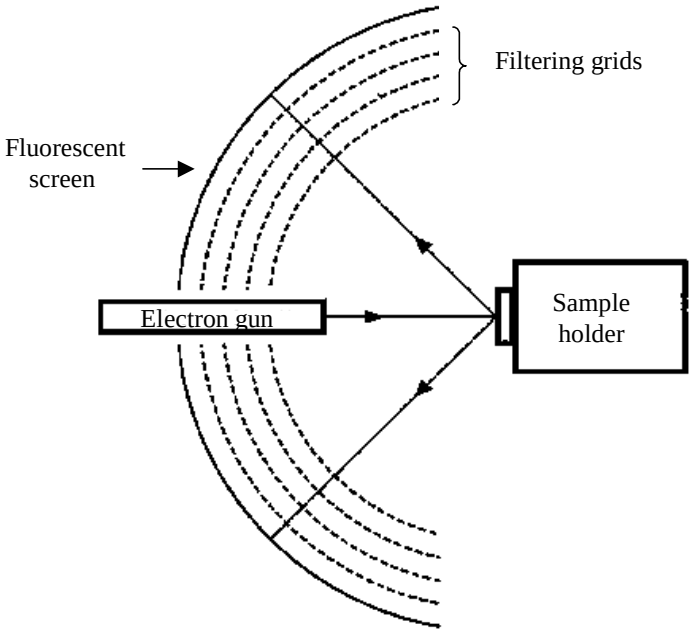

Figure 1.6. Typical Low Energy Electron Diffraction (LEED) set-up. The inelastically scattered electrons are first filtered out by a set of retarding grids, and the elastically scattered electrons are then accelerated onto a fluorescent screen. The whole system is housed in UHV.

Since its invention in 1927 (62), LEED has been developed into a principal technique for determination of surface structures. It has been used to monitor qualitatively the removal of surface contaminants in sample preparation by observing when the lattice structure of the substrate becomes clearly developed; but its major applications has been found in the study of surface reconstruction and adsorbate /substrate unit cell alignment (58, 63).

1.2.4. Scanning Tunneling Microscopy (STM) and Spectroscopy (STS)

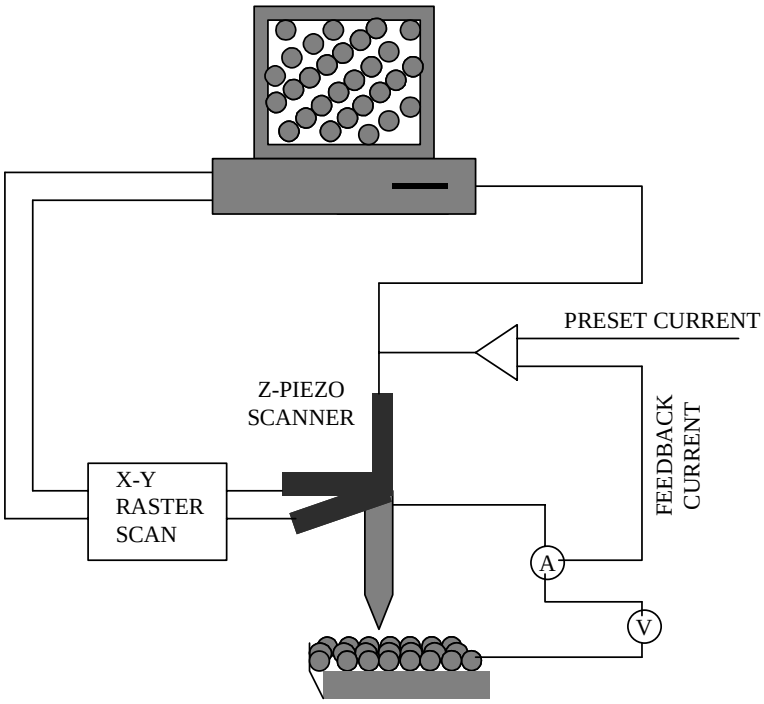

Figure 1.7. Schematic illustration of a scanning tunneling microscope. The tip can be moved in three dimensions using three orthogonal piezoelectric transducers: the *x*, *y* transducers raster scan the tip laterally while the *z* transducer varies the tip-sample distance.

Scanning tunneling microscopy (STM) was developed in the 1980s by Binnig and Rohrer (64, 65). The basic principle of STM is illustrated in figure 1.7. A sharp metal tip, typically W or PtIr, is brought into close proximity to the sample surface, so that an overlap occurs between tip and sample wave functions (66), both of which decaying exponentially into the junction gap. If a bias voltage is applied between the sample and the tip, electrons can then tunnel through the gap. The direction of tunneling current flow is determined by the polarity of the bias: if the sample is positively biased, electrons will

tunnel from the occupied states of the tip into the empty states or conduction band states of the sample; if the sample is negatively biased, electrons will tunnel from the occupied states of the sample into the empty states or conduction band states of the tip.

Since the tunneling current depends exponentially on the distance between the tip and the surface, the individual atoms in the surface will give rise to current variations as the tip is scanned across the corrugated surface in a nominally "constant height" mode. That is, the tunneling current tends to decrease (increase) as the separation between the tip and the surface atoms increases (decreases). A plot of the tunneling current *vs.* the tip position therefore shows a periodic variation which matches that of the surface structure, thus it provides a direct image of the surface.

In practice, a STM is generally operated in the 'constant-current' mode in which the actual tunneling current I_t is compared with a preset constant value (I_0), typically 0.5-5nA, in a feedback circuit. The feedback signal, proportional to the difference between I_t and I_0, provides a correction voltage to the *z* transducer and thus causes the distance *z* between the tip and the surface to change when a protrusion is traversed. Recording the feedback signal or *z* voltage as a function of the lateral tip position during raster scanning yields a map of the surface topography.

Besides imaging a sample surface, STM can also be used to obtain electronic information of the surface by means of scanning tunneling spectroscopy (STS). In fact, STS is generally carried out in the middle of an STM image acquisition so that atom-resolved probing of spectroscopic signals can be achieved (67). *I/V* (tunneling current vs. bias voltage in constant height mode) spectroscopy is the most widely STS method. The

tunnel current *I* is measured as a function of the sample-tip voltage *V*. It is then conventional to compute a *normalized conductance*, $(dI/dV)/(I/V)$, and to compare this quantity to an expected surface density of states (DOS) (67-69). This normalized conductance provides a convenient means of characterizing the observed spectrum, yielding sharp features near the onsets of surface bands which provide a more well-defined indicator of the onset position than the relatively gradual turn-on of the current or differential conductance (dI/dV). By acquisition of an *I-V* curve at every pixel within the topographic image, Hamers and co-workers (70) developed a technique called current imaging tunneling spectroscopy (CITS) in which the tunneling current intensity map can be viewed at different voltages. Using CITS, Hamers and colleagues were able to map the electronic states of Si(111) 7×7 surface with a lateral resolution of 3 Å.

In addition to *I/V* spectroscopy, *Z-V* (tip-sample separation vs. bias voltage in constant current mode) and *I-Z* (tunneling current vs. tip-sample separation in constant bias mode) spectroscopy can also be used in the study of surface electronic states (71) with atom resolved accuracy. Although STS is still at the beginning of its evolution, applications of this powerful tool will be certain to increase as the field of surface science advances.

1.3. CHAPTER REFENCES

(1) Henrich, V. E.; Cox, P. A. *The surface science of metal oxides*; Cambridge university press, 1994.

(2) Baumer, M.; Freund, H.-J. *Prog. Surf. Sci.* **1999,** *61*, 127.

(3) Strongin, D. R.; Bare, S. R.; Somorjai, G. A. *J. Catal.* **1987,** *103*, 289.

(4) Sushumna, I.; Ruckenstein, E. *J. Catal.* **1985,** *94*, 239.

(5) Murarka, S. P. *Metallization: Theory and Practice for VLSI and ULSI*; Butterworth-Heinemann: Stoneham, MA, 1993.

(6) Mayer, J. W.; Lau, S. S. *Electronic Materials Science: for Integrated Circuits in Si and GaAs*; Macmillan Publishing Company: New York, 1990.

(7) Fomino, M.; Hebert, K. R.; Asoka-Kumar, P.; Lynn, K. G. *Electrochemical Society Proceedings* **1998,** *98-17*, 642.

(8) Xu, Y.; Wang, M.; Pickering, H. W. *J. Electrochem. Soc.* **1993,** *140*, 3448.

(9) Lin, L. F.; Chao, C. Y.; MacDonald, D. D. *J. Electrochem. Soc.* **1981,** *128*, 1194.

(10) Wang, M.-H.; Hebert, K. R. *J. Electrochem. Soc.* **1999,** *146*, 3741.

(11) Pint, B. A. *Oxid. Met.* **1997,** *48*, 303.

(12) Lad, R. J. *Surf. Rev. Lett.* **1995,** *2*, 109-126.

(13) Chen, L.; Magtoto, N. P.; Kelber, J. A. *Oxid. Met.* **2000,** *54*, 285.

(14) Addepalli, S. G.; Magtoto, N. P.; Kelber, J. A. *Surf. Sci.* **2000,** *458*, 123.

(15) Addepalli, S. G. L., J.-S.; Kelber, J.A. *Oxid. Met.* **1999,** *52*, 139.

(16) Seshadri, G. X., H.-C.; Kelber, J. A. *J. Electrochem. Soc.* **1999,** *146*, 1762.

(17) Hass, K. C.; Schneider, W. F.; Curioni, A.; Andreoni, W. *Science* **1998,** *282*, 265-268.

(18) Ahn, J.; Rabalais, J. W. *Surf. Sci.* **1997,** *388*, 121-131.

(19) McHale, J. M.; Auroux, A.; Perrotta, A. J.; Navrotsky, A. *Science* **1997,** *277*, 788-791.

(20) Sullivan, J. P.; Dunn, R. G.; Barbour, J. C.; Wall, F. D.; Missert, N.; Buchheit, R. G. , Toronto 2000; The Electrochemical Society, Inc.; 24.

(21) Diebold, U.; Pan, J. M.; Madey, T. E. *Physi. Rev.* **1993,** *B47*, 3868.

(22) Moller, P. J.; Wu, M. C. *Surf. Sci.* **1989,** *224*, 250.

(23) Imaduddin, A.; Lad, R. J. *Sur. Sci.* **1993,** *290*, 35.

(24) Dake, L. S.; Lad, R. J. *Sur. Sci.* **1993,** *289*, 297.

(25) Zhong, Q.; Ohuchi, F. S. *J. Vac. Sci. Technol.* **1990,** *A8*, 2107.

(26) Betrabet, H. S.; Reddy, S. N. S.; Purushothaman, S. *Ceramic Eng. Sci. Proc.* **1989,** *10*, 1531.

(27) Parmaliana, A.; Arena, F.; Frusteri, F. *J. Chem. Soc. Faraday Trans.* **1990,** *86*, 2663.

(28) Campbell, C. T. *Surf. Sci. Rep.* **1997,** *27*, 1.

(29) Zhang, L.; Persaud, R.; Madey, T. E. *Phys. Rev. B* **1997,** *56*, 549.

(30) Varma, S.; Chottiner, G.; Arbab, M. *J. Vac. Sci. Technol. A* **1992,** *10*, 2857-2862.

(31) Nakamura, J.; Rodriguez, J. A.; Campbell, C. T. *J. Condens. Matter* **1989,** *1*, SB149.

(32) Pan, J. M.; Diebold, U.; Zhang, L.; Madey, T. E. *Surf. Sci.* **1993,** *295*, 411.

(33) Pan, J.-M.; Maschhoff, B. L.; Diebold, U.; Madey, T. E. *Surf. Sci.* **1993,** *291*, 381.

(34) Pan, J.-M.; Madey, T. E. *J. Vac. Sci. Technol.* **1993,** *A11*, 1667.

(35) Dake, L. S.; Lad, R. J. *J. Vac. Sci. Technol.* **1995,** *A13*, 122.

(36) Zhang, Z. *Surf. Sci.* **1992,** *277*, 263.

(37) Zhao, X. A.; Kolawa, E.; Nicolet, M. A. *J. Vac. Sci. Technol.* **1986,** *A4*, 3139.

(38) Ohuchi, F. S.; Kohyama, M. *J. Am. Ceram. Soc.* **1991,** *74*, 1163.

(39) Henry, C. R. *Surf. Sci. Rep.* **1998,** *31*, 231.

(40) Keller, D. V. In *Surfaces and Interfaces I*; Burke, J. J., Ed.; Syracuse University Press: New York, 1967, pp 225.

(41) Fowkes, F. M. In *Surfaces and Interfaces I*; Burke, J. J., Ed.; Syracuse University Press: New York, 1967, pp 197.

(42) Franchy, R. *Surf. Sci. Rep.* **2000,** *38*, 195.

(43) Lohrengel, M. M. *Material science and engineering* **1993,** *R11*, 243.

(44) Fan, J. C. C.; Henrich, V. E. *Appl. Phys. Lett.* **1974,** *25*, 410.

(45) Wit, H. d.; Fransen, T. In *The CRC handbook of Solid State Electrochemistry*; Gellings, P. J., Bouwmeester, H. J. M., Eds., 1997.

(46) Freund, H. J.; Kuhlenbeck, H.; Staemmler, V. *Rep. Progr. Phys.* **1996,** *59*, p. 283.

(47) Blum, R. P.; Niehus, H. *Appl. Phys. A* **1998,** *66*, S529.

(48) Blum, R.-P.; Ahlberendt, D.; Niehus, H. *Surf. Sci.* **1998,** *396*, 176.

(49) Jaeger, R. M.; Kuhlenbeck, H.; Freund, H.-J.; Wuttig, M.; Hoffman, W.; Franchy, R.; Ibach, H. *Surf. Sci.* **1991,** *259*, 235.

(50) Libuda, J.; Winkelmann, F.; Baumer, M.; Freund, H.-J.; Bertrams, T.; Neddermeyer, H.; Muller, K. *Surf. Sci.* **1994,** *318*, 61.

(51) Addepalli, S. G.; Ekstrom, B.; Magtoto, N. P.; Lin, J. S.; Kelber, J. A. *Surf. Sci.* **1999,** *442*, 385.

(52) Graupner, H.; Hammer, L.; Heinz, K.; Zehner, D. M. *Surf. Sci.* **1997,** *380*, 335.

(53) Eumann, E.; Schmitz, G.; Franchy, R. *Appl. Phys. Lett.* **1998,** *72*, 3440.

(54) Schmitz, G.; Gassmann, P.; Franchy, R. *J. Appl. Phys.* **1998,** *83*, 2533.

(55) Briggs, D.; Seah, M. P. ; John Wiley & Sons: Chichester, 1983; Vol. 1.

(56) Golden, D. A. *(Personal communication)* .

(57) Somorjai, G. A. *Chemistry in Two Dimensions: Surfaces*; Cornell University Press: Ithaca, NY, 1981.

(58) Somorjai, G. A. *Introduction to surface chemistry and catalysis*; John Wiley & Sons, Inc., 1994.

(59) Nix, R. M. *An Introduction to Surface Chemistry*; http://www.chem.qmw.ac.uk/surfaces/scc/sccinfo.htm, 1997.

(60) Feldman, L. C.; Mayer, J. W. *Fundamentals of Surface and Thin Film Analysis*; P T R Prentice-Hall, Inc.: Englewood Cliffs, NJ, 1986.

(61) Ertl, G.; Kuppers, J. *Low Energy Electrons and Surface Chemistry*; Verlag Chemie: Weinheim, 1974.

(62) Adamson, A. W. *Physical Chemistry of Surfaces*, 3 ed.; John Wiley and Sons: New York, 1976.

(63) Morrison, S. R. *The Chemical Physics of Surfaces*; Plenum Press: New York, 1990.

(64) Binnig, G.; Rohrer, H.; Gerber, C.; Weibel, E. *Phys. Rev. Lett.* **1982,** *49*, 57.

(65) Binnig, G.; Rohrer, H. *IBM J.Res. Dev.* **1986,** *30*, 355.

(66) Besenbacher, F. *Rep. Prog. Phys.* **1996,** *59*, 1737.

(67) Stroscio, J. A.; Kaiser, W. J. In *Methods of Experimental Physics*; Celotta, R., Lucatorto, T., Eds.; Academic Press, Inc.: San Diego, 1993; Vol. 27.

(68) Feenstra, R. M.; Stroscio, J. A.; Fein, A. P. *Surf. Sci.* **1987,** *181*, 295.

(69) Stroscio, J. A.; Feenstra, R. M.; Fein, A. P. *Phys. Rev. Lett.* **1986,** *57*, 2579.

(70) Hamers, R. J.; Tromp, R. M.; Demuth, J. E. *Phys. Rev. Lett.* **1986,** *56*, 1972.

(71) Wiesendanger, R. *Scanning Probe Microscopy and Spectroscopy: Methods and Applications*; Cambridge University Press: Cambridge, UK, 1994.

CHAPTER 2

COPPER WETTING OF HYDROXYLATED α-Al_2O_3(0001) SURFACE

2.1. INTRODUCTION

The interaction of metals with oxides is of basic scientific interest, and has been a subject of controversy regarding the nature of the binding forces (1, 2). Technological motivation includes the long-standing importance of such interactions in heterogeneous catalysis (3), high temperature metallurgy (4), and microelectronics, the latter recently assuming additional practical interest because of the introduction of Cu in modern integrated microcircuits (5). Cu deposition onto diffusion/adhesion barriers or dielectrics under industrial conditions typically involves a partially oxidized metallic substrate. The ability to predict the relative strength of metal interactions with a "real world" oxide and understand growth morphology would have immediate impact on both processing and materials choices in microelectronics fabrication, and the areas of catalysis, adhesion, and corrosion inhibition. Here we combine experiment with first principles theory in an attempt to further such ability.

Metal interactions specifically with alumina substrates present an important area for study because of the use of alumina in supported catalysts (3) and tunneling-based devices (6-8), and the experimental ability to produce ordered substrates in both thin film (4, 9-13) and bulk-truncated forms. Experimental results (14-20) for Cu deposited onto alumina have been inconsistent. XPS studies (14) of Cu deposited by thermal

evaporation onto bulk truncated α-Al_2O_3(0001) indicated ordered layer-by-layer growth for the first 2-3 atomic layers. The initial Cu ad-layer was observed to form "Cu-O bonds" with the substrate (14) and was present as oxidized Cu, in the form of Cu(I) ions. Other studies on polycrystalline Al_2O_3 reported layer-by-layer growth (15, 16) and Cu(I) formation at coverages below 0.5 monolayers (16). In contrast, a study on epitaxial ~ 20 Å Al_2O_3 films formed on refractory metal substrates (17) reported the growth of 3-dimensional clusters of metallic Cu, even at submonolayer Cu coverages. In particular, XPS and low energy ion scattering (LEIS) measurements (17) indicated Cu cluster formation at the lowest observable coverages at both 300 K and 80 K, with no Cu(I) observed. XANES (18, 19) measurements carried out on sapphire substrates have reported no evidence of Cu oxidation, and coverage-dependent shifts in Cu core level and LMM peaks have been interpreted in terms of final state screening (20), rather than ionization of the Cu. Meanwhile, recent ion scattering experiments by Ahn and Rabalais (21) have shown that cut and polished sapphire(0001) surfaces (the basal plane is not a cleavage surface) cannot be made free of hydrogen contamination in the form of hydroxyl even by annealing to 1400K in UHV. In addition, experimental studies of Rh deposited on ultrathin epitaxial Al_2O_3 films (22) suggest that surface hydroxyl binds the Rh to the surface as a cation and serve as nucleation sites for Rh clusters. These studies have raised the issue of the role of surface hydroxyl groups in producing the apparent disagreements summarized above. The experimental results reported below indicate initial layer-by-layer growth of Cu on hydroxylated α-Al_2O_3(0001) at 300K, and the exclusive presence of Cu(I) during the formation of the first layer.

Jennison and co-workers in Sandia National laboratory performed the theoretical study in this chapter. A few ab-initio studies of Cu on Al_2O_3 have been reported earlier (23, 24). These studies indicate a very weak interaction between Cu adatoms and the substrate. Such findings are in marked contrast to the theoretical results reported here, because relaxation of the oxide surface, not possible in small cluster models (23, 24), has been found to critically determine the nature of adsorption (25, 26). Another important difference between the methods used here and in previous studies (23, 24) is the employment of thick slabs, made possible by advances in computing and algorithms (25). The surface relaxation in sapphire(0001) is unusually large and deep (penetrating to the third oxygen layer), and necessitates slabs thicker than about 8 oxygen layers for quantitative reliability.

The first accurate theoretical study of metals on sapphire (25) found two very different adsorption mechanisms, depending on coverage. While isolated adatoms are oxidized and bind strongly as ions, if coordinated to two or more other metal adatoms, the adsorbates are metallic, showing negligible charge transfer to the surface and relatively weak adsorption, mainly by polarization. With a few interesting exceptions not relevant to the present paper, this basic pattern of binding was also found when 11 different metals were studied adsorbed on an ultrathin (~5 Å) Al_2O_3 film (24). In the latter study, Cu was noted to differ qualitatively from metals such as Pd and Pt, in that the strength of the bonding as an oxidized species is stronger due to the smaller ionic radius, while the strength of the metallic Cu-Cu interactions is weaker due to reduced cohesive energy.

Born-Haber cycles can be computed to predict thermodynamically whether a deposited metal would rather spread out on the surface as isolated adatoms or be drawn into 2D islands (25, 26); one can also, of course, compare 2D islands with 3D islands. It is then possible, if the oxidized isolated adatoms are sufficiently bound compared with the metallic atoms in 2D islands, for wetting to occur, even if 3D islands are preferred energetically over the others. In this case, 2D islands would act as kinetic barriers to 3D island formation from isolated adatoms (ions); however, if isolated adatoms are sufficiently mobile, the presence of defect nucleation sites for 3D clusters (vide infra) could then deplete the numbers of isolated adatoms by direct adsorption and thus prevent the observation of a wetted surface. These issues will be discussed below in light of the experimental data.

Recently, defect nucleation sites for Pt clusters on MgO(100) have been studied using first principles calculations (27). The two most common isolated surface defects were investigated: vacancies, both isolated and paired, and water byproducts, as both ad-OH and in-surface OH, the latter produced by the reaction of H^+ with a surface O^{2-} ion. It was found that single surface vacancies in fact destabilize Pt dimers (the first step in nucleation), while in contrast mixed divacancies and ad-OH impurities stabilize same, promoting metal island formation. In addition, it was found that ad-OH increases the adatom binding energy significantly. These results are likely to be quite general for highly ionic oxides, including sapphire. In fact, the above mentioned experimental studies of Rh deposition on hydroxylated ultrathin alumina films (22) clearly show an

increase in the density of nucleation sites. Here, however, the surface is much more hydroxylated and the consequences quite different.

This chapter reports on the binding and growth of Cu on α-Al_2O_3(0001) with a likely presence of 1/3-1/2 ML of hydroxyl impurities. Section 2.2 presents descriptions of the experimental and theoretical methods used in this study. Section 2.3 presents experimental results, while Section 2.4 contains a description of theoretical results. Discussion is presented in Section 2.5, and a summary and conclusions are contained in Section 2.6.

2.2. METHODOLOGIES

2.2.1. Experimental Methods

Experiments were carried out in a combined UHV analysis/sputter deposition system at the University of North Texas. As shown in figure 2.1, the analysis and sputter deposition chambers were independently pumped by turbomolecular pumps to tolerate high gas loadings. Chamber isolation is achieved with differentially pumped Teflon seals against the polished double-walled manipulator rod. This arrangement permits sample transport on the rod between the analysis and sputter deposition environments. The sample, 10 x 10 x 0.5 (mm) of commercially obtained α-Al_2O_3(0001), was mounted on a tantalum sample holder attached to two tantalum leads which were themselves in contact with a liquid nitrogen reservoir. A combination of liquid nitrogen cooling and resistive

heating of the sample holder permits a variation in temperature between 130 K and ~1100 K. All results reported here, however, were obtained at ambient temperature, ~300 K.

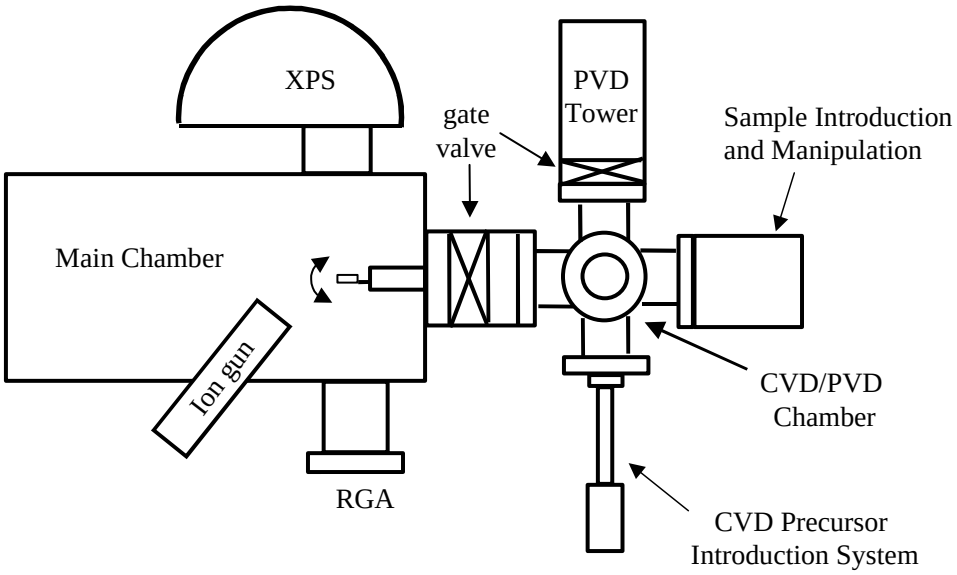

Figure 2.1. Schematic diagram of the ultra-high vacuum (UHV) system used for physical vapor deposition (PVD), chemical vapor deposition (CVD), and X-ray photoelectron spectroscopy (XPS) studies. The system was also equipped with ion gun and residue gas analyzer (RGA).

The sample was cleaned by sonication in acetone, methanol and deionized water prior to insertion in the vacuum system. Working pressures in the analysis chamber were in the range of 1-5 x 10^{-9} Torr, and in the range of 10^{-8}--10^{-7} Torr in the sputter deposition chamber (in the absence of plasma). Pressures in both chambers (in the absence of plasma) were monitored by nude ion gauges in both chambers placed out of line of sight of the sample. Pressures during plasma-induced sputter deposition were monitored with a baratron gauge.

XP spectra were acquired using a commercially available hemispherical sector analyzer (VG100AX) operated at a constant pass energy of 50 eV. Calibration of the

analyzer energy scale was carried out using sputter-cleaned Cu and Au samples, according to established techniques (28). Mg Kα radiation was obtained from a commercial, unmonochromatized source (Physical Electronics, PHI Model 1427) operated at 15 kV and 300 W. Software for data acquisition and analysis has been described elsewhere (29). Elemental atomic sensitivity factors appropriate to this analyzer (obtained from VG Microtech, UK) were used to estimate surface coverages and chemical composition from the integrated intensities of core-level transitions. XPS spectra were acquired with the sample aligned normal to the analyzer axis (normal incidence) and at 60°(with respect to the surface normal - grazing incidence).

The sputter gun (Physical Electronics) was operated by direct Ar gas feed into the ionization chamber with a variable excitation voltage of 1-5 KeV. Sputter deposition of Cu was carried out using a commercial water-cooled magnetron source (MiniMak), and an Ar plasma with a partial pressure of 0.015 Torr. Plasma power was readily maintained so as to give highly reproducible deposition rates as low as 0.01 ML Cu/min. This mechanism resulted in the deposition of Cu free from oxygen contamination, as determined by XPS measurements of films deposited on oxygen-free substrates (e.g., polyethylene). Cu depositions were carried out with the sample temperature initially at 300 K. Negligible increases in sample temperature were observed during plasma deposition. Repeated exposure of the sample to the environment of the sputter deposition chamber resulted in an unavoidable accumulation of adventitious carbon of the sample. Carbon coverage, however, appeared to saturate at ~0.5 monolayers (on a carbon to oxygen atomic basis), and was usually significantly lower (~0.1- 0.3 monolayers). Some

trace contamination due to Ca impurities in the sapphire was also observed. No carbon contamination was observed as a function of Cu deposition. Deliberate variation of carbon coverage between 0.1 and 0.5 monolayers (e.g., by varying sample exposures to the vacuum of the deposition chamber prior to deposition) had no significant effect on Cu nucleation behavior or oxidation state.

2.2.2. Theoretical Methods

The electronic structure calculations were performed by D.R. Jennison and co-

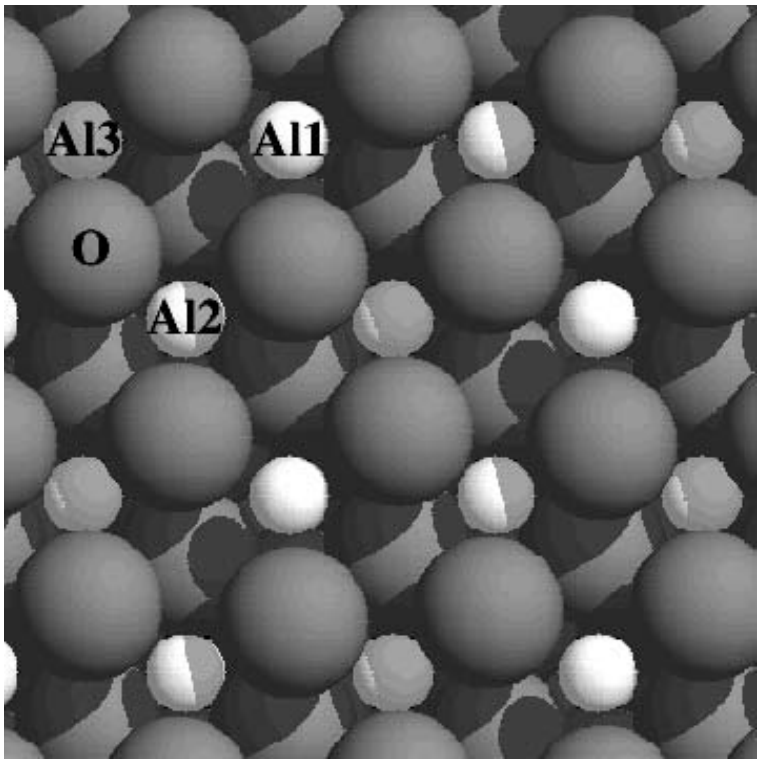

Figure 2.2. Representation of the sapphire(0001) surface showing the most favored sites for 1/3 ML Cu ("Al3", hollow sites above the deepest Al cations) and 1 ML Cu ("O", atop O).

workers at Sandia National Laboratories (Albuquerque, NM), using the Vienna Ab Initio Simulation Package (VASP) (30-32). This plane-wave based density-functional (33, 34) code uses the ultrasoft pseudopotentials of Vanderbilt (35) that permit good convergence at a plane wave cutoff of 270 eV. For sapphire, this value produces excellent agreement with the results of Ref. (25), which used much harder potentials and which agreed with all-electron calculations in the literature. In the case of Cu, this potential results in a lattice constant of 3.53 Å, within 0.8% of the nominal value. For "standard" local density theory, they used the Perdew/Zunger parameterization (36) of the Ceperley/Alder electron gas results (37). Geometric relaxation, to forces < 0.05 eV/Å, was done through a quasi-Newton algorithm. A damped dynamics method was found to speed the final relaxation process. The vacuum between repeating slabs exceeded 18 Å. The slabs had nine layers of three O and two Al atoms per unit cell, with Cu and/or OH added to both sides. The center three Al_2O_3 layers were frozen at the bulk LDA spacing, while all other atoms were geometrically free to relax. The most favored sites were considered, which for 1/3 ML Cu is the hollow site above the deepest Al ion ("Al3" in Fig. 2.2) (23-25), and for 1 ML Cu is atop O (25). The energy of 1/3 ML of ad-OH placed above the shallowest Al ion ("Al1", the obvious site based on electrostatics) was also considered, with and without 1/3 ML and separately 1 ML of Cu in sites O, which maximize the interaction with the OH. (The relaxed adsorbate positions with ad-OH present are distortions of these beginning positions.)

2.3. EXPERIMENTAL RESULTS

2.3.1. Vicinal and Lightly Sputtered Sapphire Surfaces

After insertion into the UHV chamber, XPS survey and core level spectra were obtained for the sapphire surface before annealing, after annealing to 1100 K in 5 x 10^{-6}

Table 2.1. Calculated sapphire(0001) surface O to Al atomic ratio($\pm$0.05) based on XPS data taken after annealing (1 hour at 1100K, in 5×10^{-6} Torr O_2) and Ar^+ sputtering at 1 KeV(6 min), 2 KeV(10 min), and 5 KeV(10 min). (θ is the angle between the analyzer lens and the sample surface normal.)

θ	Initial	Annealed in O2	1 KeV	2 KeV	5 KeV
0°	1.54	1.52	1.52	1.51	1.49
60°	1.73	1.72	1.72	1.61	1.45

Table 2.2. Initial Sapphire sample Core level binding energies (eV) with differential charging indicated within parentheses.

XPS line	Al(2p)	C(1s)	O(1s)
Literature values (*)	74.4	284.5	531.0
Normal incidence	88.9 (14.5)	298.4 (13.9)	543.7 (12.7)
Grazing incidence	87.8 (13.4)	297.6 (13.1)	543.2 (12.2)

* *Handbook of X-Ray Photoelectron Spectroscopy*, Edited by J. Chastain, R.C. King, Jr. (Physical Electronics, Inc. 1995)

Torr O_2, and after subsequent light Ar ion sputtering (1 KeV, 6 min) and annealing to 1100 K in O_2 (pressure = 5.0×10^{-6} Torr) or UHV for 1 hour. Observed O(1s), Al(2p) stoichiometries derived from core-level intensities are shown in Table 2.1. Relative O and Al atomic concentrations in the XPS analysis region can be derived from XPS intensities (38) according to:

$$N_O/N_{Al} = (I_O' \times S_{Al})/(I_{Al}' \times S_O) \qquad (2.1)$$

where N, S and I' are, respectively, the atomic concentrations, atomic sensitivity factors and XPS signal intensity from the very top monolayer. I' can be derived using

$$I' = \int_{x=0}^{1} e^{-x/\lambda} dx \Big/ \int_{x=0}^{\infty} e^{-x/\lambda}\, dx \qquad (2.2)$$

where λ is the mean free path length for O(1s) or Al(2p) photoelectrons in units of monolayers, 5.2 monolayers and 7.2 monolayers, respectively (38).

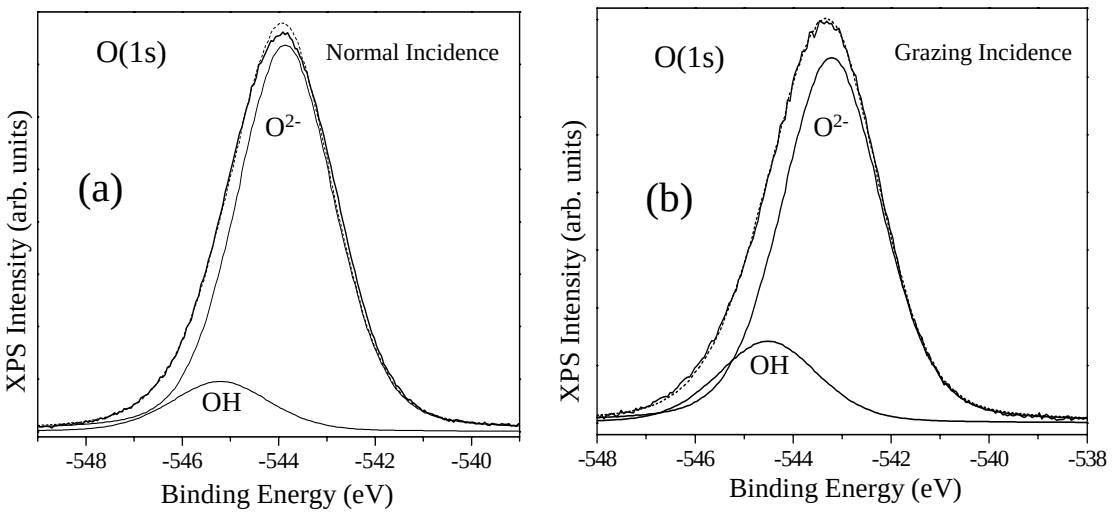

Figure 2.3. O(1s) spectra (without charging correction) of sapphire(0001): (a) normal incidence; (b) 60° grazing incidence. Both are well fit by two components: a major O^{2-} peak and a minor OH peak at 1.3 eV higher binding energy (FWHM 2.4 eV).

As shown in Table 2.1, the light sputtering treatment (which reduces contaminant carbon below observable levels) does not result in significant change in relative O and Al core level XPS intensities. O(1s) and Al(2p) spectra obtained after sputtering are displayed in Figs. 2.3 and 2.4 respectively. Binding energies and peak shapes were unchanged from those observed prior to the final sputter/anneal treatment.

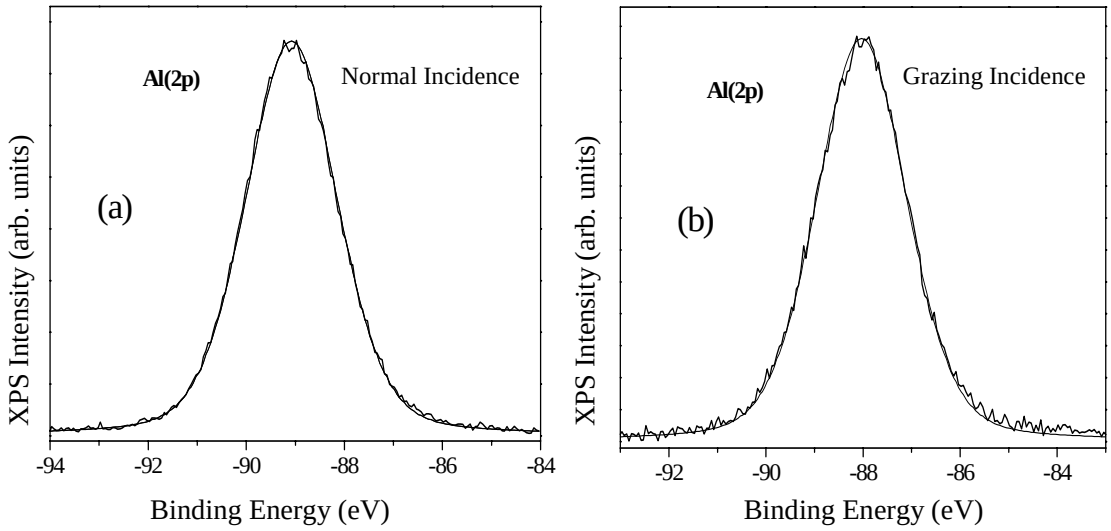

Figure 2.4. Al(2p) spectra (without charging correction) of sapphire(0001): (a) normal incidence; (b) 60° grazing incidence. Both are well fit by a single component with FWHM of 2.2 eV.

Core level binding energies, as observed and compared with corresponding literature values, are summarized in Table 2.2. Deviations in the observed binding energies from the corresponding literature values indicate that the amount of charging increases with binding energy (decreased kinetic energy), as expected if charging is a function of the inelastic mean free path of the photoelectrons. Comparison of normal incidence vs. grazing incidence results shows that differential charging is more

pronounced with greater sampling depth. Such differential charging has been reported previously (14, 39-42) in studies on insulating substrates. Correction for such differential charging effects is obviously more problematic than for uniform charging. The core level spectra listed in Table 2.2 were assigned to the literature values given. This makes it difficult, however, to precisely correct for shifts in the Cu(2p) and Cu(LMM) spectra in order to obtain accurate Cu Auger parameters {Auger Parameter = BE[Cu($2p_{3/2}$)] + KE(Cu_{LMM})}. Therefore, characterization of the deposited copper by values of Cu Auger parameters must be regarded with considerable suspicion in these experiments. For this reason, we rely on well known changes in the Cu(LMM) lineshape (43, 44) to characterize the electronic state of Cu ad-atoms, and avoid making any judgements based on the value of the Cu Auger parameter. The Cu(LMM) lineshape was determined to be independent of sample charging, which could be varied by changing the X-ray source-to-sample distance.

The O(1s) spectra obtained after light sputtering (Fig. 2.3), at grazing and normal incidence, are both well fit by two components (each with FWHM = 2.4 eV) with a minor peak at 1.3 eV higher binding energy than the major peak. Also in agreement with previous reports (14), the relative intensity of the higher binding energy component compared to the main peak is increased in the grazing incidence spectrum, indicating that this component corresponds to a surface species and is assigned to surface hydroxyl groups. The presence of hydrogen in the sapphire surface region, even after extensive annealing in UHV, has been confirmed by ion-scattering experiments (21). The Al(2p) spectra are well fit by a single spectral component. The relative O and Al concentrations

derived from normal incidence measurements (Table 2.1) are as expected for stoichiometric sapphire, for both the initial and 1 KeV sputtered surfaces. Ratios obtained from grazing incidence spectra, however, indicate oxygen enrichment (Table 2.1). These data are again consistent with hydroxylation of the surface.

An estimate of the surface hydroxyl coverage can be obtained as follows (38):

$$I_B = I_B^{\infty}\{1-\Phi_A+ \Phi_A\exp[-a_A/\lambda_A(EB)\cos\theta]\} \qquad (2.3)$$

where I_B is the O(1s) signal intensity from the substrate(covered by –OH), I_B^{∞} is the O(1s) signal from a pure substrate, a_A is the diameter of –OH(~2.8Å (45)), λ_A is the mean free path for O(1s) electrons(~11Å (38, 46)), and θ is the angle between the analyzer lens axis and the surface normal. Using the total O(1s) peak area as I_B^{∞}, an initial –OH surface coverage of 0.47 ML is obtained. This coverage is not affected by either annealing to 1100 K in UHV or O_2, consistent with previously reported results (21).

2.3.2. Cu Growth on Hydroxylated α-Al_2O_3(0001) Surface

Results of Cu deposition were the same on unsputtered and lightly sputtered surfaces, and are shown below for the latter (which is carbon free before deposition). Fig. 2.5a shows X-ray excited Cu(LMM) spectra as a function of Cu deposition time. The evolution of the Auger lineshape indicates that for deposition times < 12 minutes, Cu is present as Cu(I). At longer deposition times (higher coverages), the evolution of a new feature at approximately 3 eV higher kinetic energy (corresponding to a higher Auger parameter) indicates the onset of Cu(0) formation (43, 44). In order to determine that the Cu(I) formation observed at low coverages was not an artifact of contamination from the

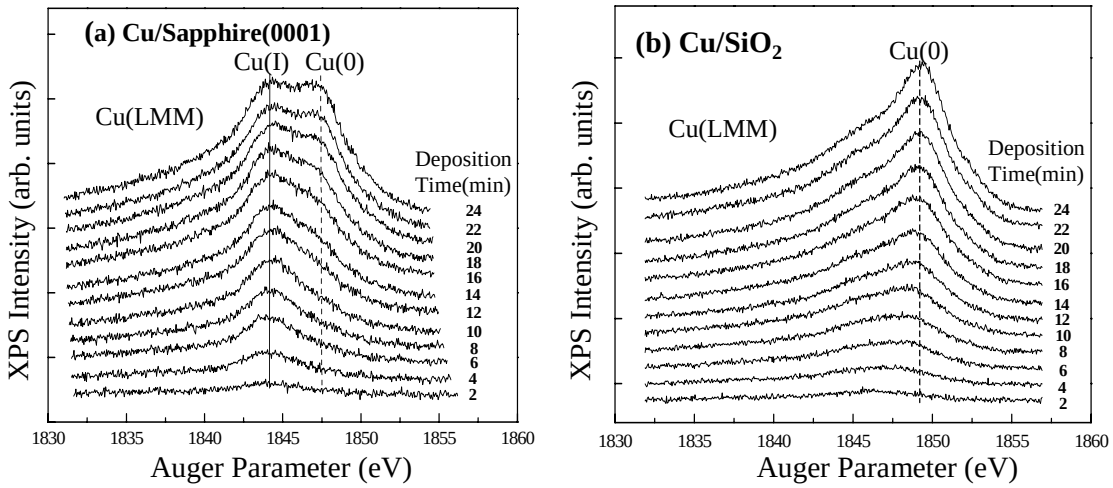

Figure 2.5. Cu(LMM) evolution during Cu deposition on (a) sapphire(0001) and (b) SiO2 with deposition rate at 0.03 ML Cu/minute. Deposition temperature = 300K. Due to differential charging on sapphire surface, the Auger parameter for Cu(0) on sapphire is different from that on SiO_2.

chamber ambient, or in some way due to the use of sputter deposition instead of thermal evaporation, a similar experiment was carried out for Cu deposition on a ~ 1000 Å film of amorphous SiO_2 grown on a Si wafer substrate. Cu is well known to interact only weakly with SiO_2 surfaces (47). The results for Cu/SiO_2 (Fig. 2.5b) indicate the presence of Cu(0) even at the lowest observable coverages. Therefore the presence of Cu(I) on sapphire at low coverages is due to Cu ad-atom interaction with the substrate, and not due to experimental artifacts.

The change in relative Cu(2p3/2) XPS intensity (normalized to the O(1s) intensity) with Cu deposition (the uptake curve) is shown in Fig. 2.6 for Cu on sapphire. The uptake curve on sapphire (Fig. 2.6) shows a sharp change in slope, which is indicative of layer-by-layer growth (wetting) (38).

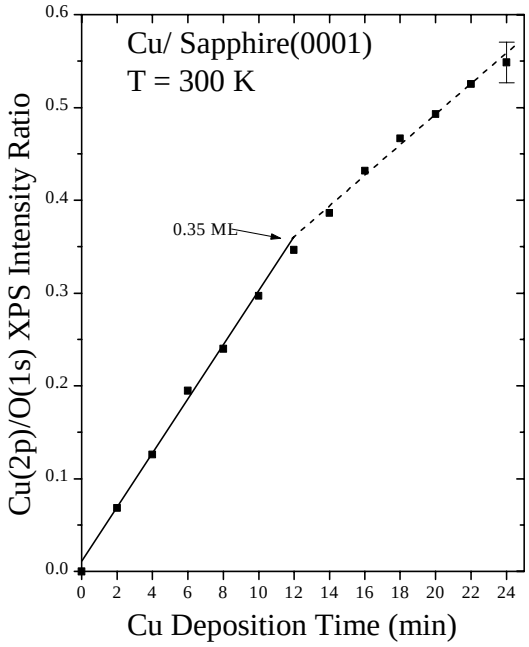

Figure 2.6. Cu(2p)/O(1s) ratio vs. deposition time for Cu on sapphire(0001) (deposition rate at 0.03ML Cu/min). Cu(I) grows to a maximum coverage of ~0.35ML, after which Cu(0) formation was observed. The sharp change in slope indicates a layer-by-layer growth mode.

A comparison of Figs. 2.5a and 6 indicates that the appearance of Cu(0) corresponds to the completion of the first layer; i.e., the first layer consists of Cu(I). The Cu coverage at which this change in slope occurs can be calculated from XPS intensities according to equation (2). Estimating mean free path values from the universal curve (46) yields a value of 9 Å for the Cu(2p3/2) transition, and 11 Å for the O(1s) transition. These data therefore indicate that the initial Cu(I) ad-layer grows to a maximum coverage of ~0.35 monolayer (on a Cu/O atomic basis), at which point formation of Cu(0) occurs on top of the Cu(I) ad-layer.

2.3.3. Thermal Stability of the Cu-Adlayers

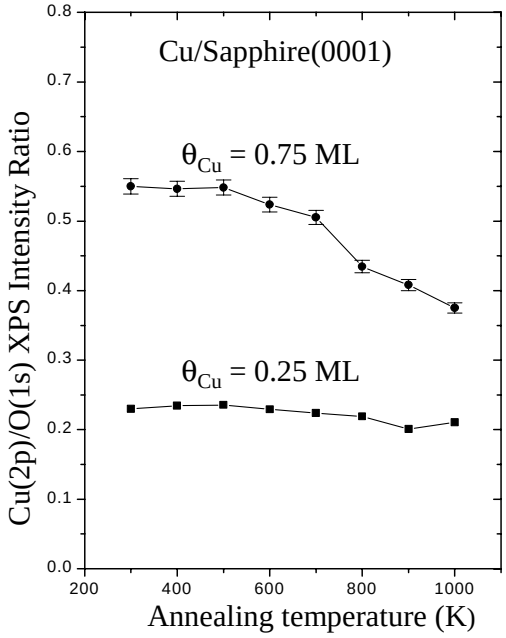

Figure 2.7. Cu(2p)/O(1s) ratio during annealing of 0.25 and 0.75 ML Cu deposited on sapphire(0001). Dewetting of Cu occurred at 500-600K for coverage of 0.75 ML. No dewetting was observed up to 1000K for 0.25 ML coverage.

The thermal stability of the deposited Cu was tested by annealing the Cu-modified surface to temperatures up to 1000 K in UHV. The annealing behavior of Cu strongly depends on total Cu coverage. As shown in Figs. 2.7 and 2.8, a 0.25 ML coverage of Cu [pure Cu(I)] is stable up to 1000 K without significant change in either relative Cu (2p3/2) intensity or change in oxidation state (Fig. 2.8a). At 0.75 ML coverage, however, both Cu(I) and Cu(0) are present. Annealing to elevated temperatures now results in a notable reduction in the total relative Cu intensity (Fig. 2.7). Coincident with this, the portion of the Cu(LMM) spectrum corresponding to Cu(I) shows a marked decrease in

relative intensity compared to the Cu(0) component. (An examination of the Cu(2p) spectrum reveals that no observable amounts of Cu(II) are present at any time during this procedure.)

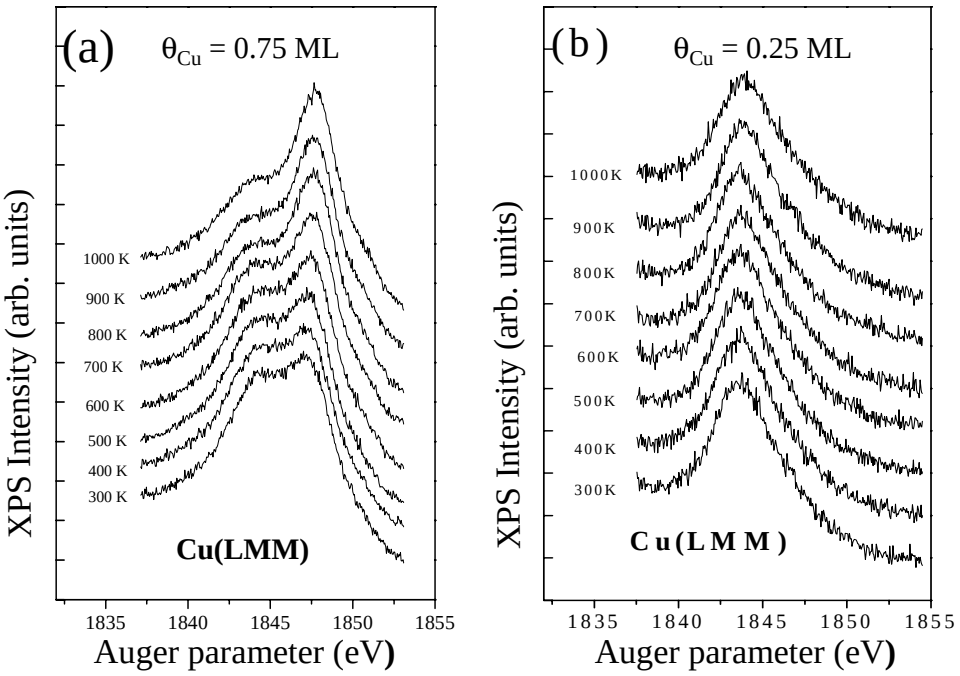

Figure 2.8. Cu(LMM) line shape change during annealing of (a) 0.75 ML (b) 0.25 ML Cu deposited on sapphire(0001) (kept 20 minutes at each temperature). While Cu(I) stable up to 1000K at low coverage(0.25 ML), Cu(I) reduction to Cu(0) was observed as early as 500K at high coverage(0.75 ML).

The data in Figs. 2.7 and 2.8a indicate that, at a Cu coverage of 0.75 ML, annealing to slightly elevated temperatures (~500 K or higher) results in the formation of 3-D nuclei of metallic Cu, including the Cu(I) originally present at the surface. At such low temperatures, desorption of Cu from the surface can be discounted (The Cu sublimation temperature is 1150 K (48)). If only the Cu(0) originally present at 300 K

were involved in the nucleation (de-wetting) process, then one would expect an increase in the relative Cu(I) intensity in the Cu(LMM) spectrum. Therefore, the data in Figs. 2.7 and 2.8 indicate that the presence of Cu(0) causes Cu(I) to dewet from the surface at relatively low temperatures. In the absence of Cu(0), Cu(I) is stable on the surface to at least 1000 K.

2.4. THEORETICAL RESULTS

Table 2.3 shows the LDA adsorption energy of Cu at 1/3 and 1 ML coverage at the strongest binding sites (25) on the sapphire surface. The results indicate that when isolated, Cu adatoms are oxidized and bind strongly. The results of a Born-Haber analysis, where the tendency to form 2D islands is given by a negative value (no wetting) of ΔE = E(1ML Cu) + 2E(clean surface) - 3E(1/3 ML Cu). Cu adatom binding is sufficiently weak on clean sapphire surface so 2D islanding is favored over wetting.

Table 2.3. The LDA adsorption energy of Cu on a per atom basis in eV on clean sapphire(0001), and on hydroxylated sapphire with 1/3 ML of ad -OH. The Born-Haber energy ΔE_{01} is positive when wetting occurs.

Cu coverage	1/3 ML	1 ML	ΔE_{01}
Sapphire	+1.8	+0.5	-4.5
Sapphire + OH	+5.2	+1.1	+3.8
Above with dissociated OH	--	+1.3	+3.1

Similar results for the hydroxylated surface can be seen in Table 2.3. Here, Cu adatom binding is more than doubled, as is also the binding at 1 ML. The relaxed surface with 1/3 ML of both Cu and ad-OH may be seen in Fig. 9a, and details concerning the Cu(I) geometry may be seen in Table 2.4. Now we see that the substantial number of OH groups has reversed the Born-Haber prediction of the clean surface, and wetting is indeed preferred, as observed; the relative total energies used in these calculations may be found in Table 2.5.

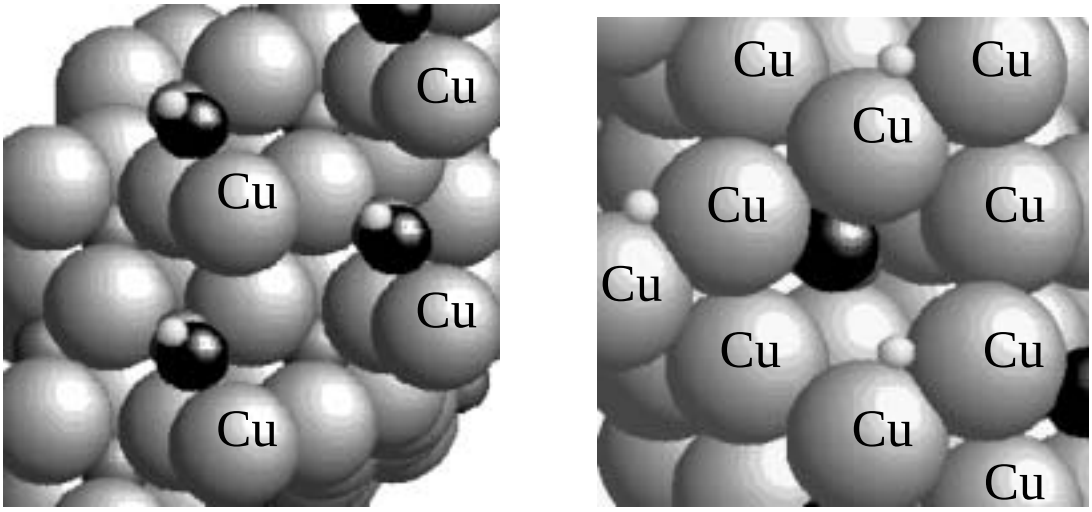

Figure 2.9. (a) The relaxed structure of 1/3 ML of Cu coadsorbed with 1/3 ML of ad-OH on sapphire(0001); (b) the relaxed geometry of 1 ML of Cu coadsorbed with 1/3 ML of ad-OH, which has been dissociated by the presence of the Cu.

Finally, a possible reaction of Cu at 1 ML with OH, leading to OH dissociation, was also examined. This reaction is exothermic by 0.6 eV per unit cell. In the relaxed

geometry in this case, the H is associated with metallic Cu far from the adoxygen left behind, while the latter is closely coordinated to two Cu atoms, as may be seen in Fig. 9b. However, this result does not alter the wetting prediction (Table 2.3).

Table 2.4. Geometry of relaxed 1/3 ML of Cu coadsorbed with 1/3 ML of ad-OH on sapphire (0001) (Fig. 2.9a); since the basal plane buckles by 0.18 Å, the height is to the unbuckled plane.

Height\Bond length	Distance (Å)
Cu to O plane	1.48
Cu to O (of OH)	2.02
O (of OH) to Al	1.78

Table 2.5. Relative energies(for one surface) used in Born-Haber cycle calculations (these do not equate to binding energies because of the lateral interactions between ad-species. Unit: eV).

Structure	Sapphire(0001)	Sapphire(0001) +1/3ML ad-OH
Slab	0.0	0.0
+ 1/3 ML Cu	-2.2	-5.6
+ 1 ML Cu	-11.0	-13.3

2.5. DISCUSSION

The experimental results presented above demonstrate that Cu will wet a substantially hydroxylated α-Al_2O_3(0001) surface at 300 K. The initially deposited Cu forms a conformal Cu(I) ad-layer with a maximum coverage of ~0.35 ML (on a Cu/O basis). At higher coverages, Cu(0) forms over the initial Cu(I) ad-layer. These results are in excellent agreement with theoretical calculations performed on thick slabs, which show that hydroxylation should significantly increase the binding of Cu to the sapphire (0001) surface, and that maximum Cu(I) coverage will be limited by the fact that at higher coverages, Cu-Cu interactions causing metallic Cu would predominate. In fact, the reaction of the additional Cu(0) with the initial Cu(I) is observed to be activated by an increase in temperature.

The experimental and theoretical results strongly suggest a rationale for the wide range of contradictory results (14-20) reported for Cu wetting of alumina surfaces. First, the degree of sapphire surface hydroxylation is not obvious from a routine inspection of the XPS data of the clean surface, and a reading of the relevant reports (14-20) indicates that surface hydroxylation was not a prominent concern for many experimental groups. Second, thin alumina films are much more readily de-hydroxylated by being produced and by annealing in UHV than are sapphire surfaces (21, 49). Therefore, in comparing literature results, one is most likely comparing substantially hydroxylated sapphire surfaces to unhydroxlyated or lightly hydroxylated thin films (polycrystalline or epitaxial). The theoretical and experimental results shown here predict that Cu growth on

alumina should vary greatly with the degree of surface hydroxylation. In this regard, it is useful to note results recently reported for Cu deposited on presumably dehydroxylated epitaxial Al_2O_3 films ~ 20 Å thick (17), which clearly indicate that Cu does not wet the surface. In summary, the Cu/alumina binding is predicted to be significantly affected by both surface hydroxylation and alumina substrate thickness.

The experimental results (Figs. 2.7 and 2.8) also show that the thermal stability of adsorbed Cu(I) species is decreased in the presence of Cu(0). The thermal stability of very low coverages of Cu on sapphire (hydroxyl coverage undetermined) has been previously characterized by Auger spectroscopy (50). Those results indicated that at very low coverages, the Cu ad-layer was stable to at least 700 K (50). These results are in agreement with those presented here, which indicate that the initial layer [Cu(I)] is stable on the hydroxylated basal plane of sapphire to ~1000 K. Subsequently deposited Cu(0), however, will not only nucleate (dewet) at relatively low temperatures, but will also cause the apparently tightly bound Cu(I) to dewet from the surface. Such behavior is quite different from what is observed, for example, in the Cu/W(100) system (51), where the first Cu adlayer is tightly bound to the substrate whether or not a subsequent layer is present. The temperatures at which decreases in Cu(I) coverage are observed (~ 500 K, fig. 2.7) are sufficiently low as to rule out dehydroxylation of the surface as a cause of this behavior.

The hopping energy for Cu(I) on a sapphire surface has not been computed, but activation energies of 0.4-0.5 eV have been reported for Pt adatoms on (non-hydroxylated) Al_2O_3/NiAl(110) (52), and computed Pt binding energies for this surface

are ~ 3 eV by LDA (25). Here, however, one CANNOT assume the same ratio between hopping barrier and binding energy, because while hopping on the clean surface might involve an activation barrier similar to the hollow-to-atop energy difference (< 1 eV), hopping on hydroxylated sapphire would involve hopping from the adjacent site to an ad-OH (binding energy ~5.2 eV) to a site away from the ad-OH (clean surface binding energy ~1.8 eV), resulting in an activation energy of > 3 eV. Assuming a reasonable prefactor of $\sim 10^{12}$, this implies rapid diffusion (on experimental time scales) on the clean surface but negligible diffusion on the hydroxylated surface. In addition to slow diffusion, dimerization in the absence of Cu(0) is obviously hindered by Cu(I)-Cu(I) repulsion. These arguments could explain the high temperature stability of Cu(I) at lower coverages. At higher coverages, the presence of Cu(0) would facilitate dimerization and metal island nucleation, the latter of which would irreversibly reduce the Cu(I), as observed.

There has been no information concerning the detailed morphology of the prepared surface, such as the density of steps, point defects, etc. The fact that wetting has been observed on both ordered bulk (sapphire) (14) and disordered (polycrystalline film) surfaces (15), while non-wetting as also been reported for bulk sapphire (18-20) and for epitaxial films(17), indicates that the transition from wetting to non-wetting does not depend on such details of surface topography. In addition, the experimental results reported here are observed to be independent of adventitious carbon, at least up to coverages of ~ 0.5 ML. This indicates that such contamination does not critically impact

wetting behavior under these conditions and therefore the results presented here are of relevance to situations of practical industrial processing.

In view of the above results demonstrating enhanced binding of Cu, as Cu(I), to hydroxylated sapphire surfaces, the mechanical adhesion results for Cu overlayers deposited on unsputtered and pre-sputtered sapphire surfaces are of interest (53). Those studies observed an order of magnitude increase in Cu/sapphire mechanical adhesion for an optimum amount of Ar^+ sputtering of the sapphire surface prior to Cu deposition, followed by annealing of the interface after deposition. The authors concluded that pre-sputtering might induce an interfacial alloy which would lead to enhanced adhesion, as suggested by Cu Auger and photoemission spectra. We must therefore conclude that the effects of hydroxylation explored here are only one aspect of interfacial wetting/adhesion, and that defects (vacancies, dehydroxylation, etc.) induced by sputtering of sapphire or perhaps other alumina surfaces may trigger new interfacial reaction pathways at elevated temperatures.

2.6. CONCLUSIONS

Experimental studies have examined the deposition of Cu on a substantially hydroxylated α-Al_2O_3(0001) (sapphire) substrate at 300 K under UHV conditions. The results agree with a conceptual model from first principles theoretical calculations on Cu adsorption on hydroxylated sapphire. The results include the following:

1. Cu deposition onto hydroxylated sapphire(0001) at 300 K results in initial Cu wetting of the substrate and layer-by-layer growth.

2. The initial Cu adlayer is oxidized to Cu(I), with a maximum surface coverage of ~0.35 monolayers on a Cu/O atom basis. This is in good agreement with theoretical calculations which predict a maximum coverage of Cu(I) of 0.33 monolayers, due to the predominance of Cu-Cu interactions at higher coverages.
3. In the absence of Cu(0), adsorbed Cu(I) is stable on the hydroxylated sapphire surface up to at least 1000 K. In the presence of Cu(0), Cu(I) is destabilized at ~ 500 K or greater, and begins to join in the formation of 3-D Cu(0) nuclei.

2.7. CHAPTER REFERENCES

(1) Lad, R. J. *Surf. Rev. Lett.* **1995,** *2*, 109-126.

(2) Henrich, V. E.; Cox, P. A. *The surface science of metal oxides*; Cambridge university press, 1994.

(3) Ertl, G.; Freund, H.-J. *Physics Today* **1999,** *52*, 32-38.

(4) Stott, F. H. *Rep. Progr. Phys.* **1987,** *50*, 861.

(5) *National Technology Roadmap for Semiconductors*; Semiconductor Industry Association: San Jose, CA, 1997.

(6) Oepts, W.; Verhagen, H. J.; Jonge, W. J. M. d.; Coehoorn, R. *Appl. Phys. Lett.* **1998,** *73*, 2363.

(7) Oepts, W.; Verhagen, H. J.; Coehoorn, R.; Jonge, W. J. M. d. *J. Appl. Phys.* **1999,** *86*, 3863.

(8) Shiga, K.; Komori, J.; Katsumata, M.; Teramoto, A.; Mashiko, Y. *IEICE Trans. Electron.* **1999,** *E82-C*, 589.

(9) Wu, M.-C.; Goodman, D. W. *J. Phys. Chem.* **1994,** *98*, 9874-9881.

(10) Wu, Y.; Garfunkel, E.; Madey, T. E. *J. Vac. Sci. Technol. A* **1996,** *14*, 2554-2563.

(11) Jaeger, R. M.; Kuhlenbeck, H.; Freund, H.-J.; Wuttig, M.; Hoffman, W.; Franchy, R.; Ibach, H. *Surf. Sci.* **1991,** *259*, 235.

(12) Cotterill, G. F.; Niehus, H.; O'Connor, D. J. *Surf. Rev. Lett.* **1966,** *3*, 1355.

(13) Becker, C.; Kandler, J.; Raaf, H.; Linke, R.; Pelster, T.; Draeger, M.; Tanemura, M.; Wandelt, K. *J. Vac. Sci. and Technol.* **1998,** *A16*, 1000.

(14) Varma, S.; Chottiner, G.; Arbab, M. *J. Vac. Sci. Technol. A* **1992,** *10*, 2857-2862.

(15) Chen, J. G.; Colaianni, M. L.; Weinberg, W. H.; Yates, J.T. Jr. *Surf. Sci.* **1992,** *279*, 223-232.

(16) Ohuchi, F. S.; French, R. H.; Kasowski, R. V. *J. Appl. Phys.* **1987,** *62*, 2286-2289.

(17) Wu, Y.; Garfunkel, E.; Madey, T. E. *J. Vac. Sci Technol. A* **1996,** *14*, 1662-1667.

(18) Gota, S.; Gautier, M.; Douillard, L.; Thromat, N.; Duraud, J. P.; Fevre, P. L. *Surf. Sci.* **1995,** *323*, 163-174.

(19) Gautier, M.; Van, L. P.; Duraud, J. P. *Europhys. Lett.* **1992,** *18*, 175-180.

(20) Vijayakrishnan, V.; Rao, C. N. R. *Surf. Sci. Lett.* **1991,** *255*, L516-L522.

(21) Ahn, J.; Rabalais, J. W. *Surf. Sci.* **1997,** *388,* 121-131.

(22) Libuda, J.; Frank, M.; Sandell, A.; Anderson, S.; Bruhwiler, P. A.; Baumer, M.; Martensson, N.; Freund, H.-J. *Surf. Sci.* **1997,** *384,* 106.

(23) Castro, V. D.; Polzonetti, G.; Zanoni, R. *Surf. Sci.* **1985,** *162,* 348.

(24) Johnson, K. H.; Pepper, S. V. *J. Appl. Phys.* **1982,** *83,* 6634.

(25) Verdozzi, C.; Jennison, D. R.; Schultz, P. A.; Sears, M. P. *Phys. Rev. Lett.* **1999,** *82,* 799-802.

(26) Bogicevic, A.; Jennison, D. R. *Phys. Rev. Lett.* **1999,** *82,* 4050.

(27) Bogicevic, A.; Jennison, D. R. *Surf. Sci.* **1999,** *437,* L741.

(28) Powell, C. J. *Surf. Interface Anal.* **1995,** *23,* 121.

(29) Martini, D.; Shepherd, K.; Sutcliffe, R.; Kelber, J. A.; Edwards, H.; Martin, R. S. *Apllied Surf. Sci.* **1999,** *141,* 89-100.

(30) Kresse, G.; Hafner, J. *Phys. Rev. B* **1993,** *47,* 558.

(31) Kresse, G.; Hafner, J. *Phys. Rev. B* **1994,** *49,* 14251.

(32) Kresse, G.; Hafner, J. *Phys. Rev. B* **1996,** *54,* 11169.

(33) Hohenberg, P.; Kohn, W. *Phys. Rev. B* **1964,** *136,* B864.

(34) Kohn, W.; Sham, L. J. *Phys. Rev. A* **1965,** *140,* A1133.

(35) Vanderbilt, D. *Phys. Rev. B* **1990,** *41,* 7892.

(36) Perdew, J. P.; Zunger, A. *Phys. Rev. B* **1981,** *23,* 5048.

(37) Ceperley, D. M.; Alder, B. J. *Phys. Rev. Lett.* **1980,** *45,* 566.

(38) Briggs, D.; Seah, M. P. ; John Wiley & Sons: Chichester, 1983; Vol. 1.

(39) Barr, T. L. *J. Vac. Sci. Technol. A* **1989,** *7,* 1677-1683.

(40) Yu, X.; Hantsche, H. *Surf. Interface Anal.* **1993,** *20*, 555-558.

(41) Pertsin, A. J.; Pashunin, Y. M. *Applied Surf. Sci.* **1990,** *44*, 171-178.

(42) Cazaux, J.; Lehuede, P. *J. Electron Spectrosc. Relat. Phenom.* **1992,** *59*, 49-71.

(43) Pijpers, A. P.; Berreshelm, K.; Wilmers, M. *Fresenius J. Anal. Chem.* **1993,** *346*, 104-109.

(44) Fleisch, T. H.; Mains, G. J. *Appl. Surface Sci.* **1982,** *10*, 51-62.

(45) Lide, D. R.; Frederikse, H. P. R. ; CRC Press: Ann Arbor, MI, 1993.

(46) Somorjai, G. A. *Introduction to surface chemistry and catalysis*; John Wiley & Sons, Inc., 1994.

(47) Zhou, J. B.; Gustafsson, T.; Garfunkel, E. *Surf. Sci.* **1997,** *372*, 21.

(48) Peden, C. H. F.; Kidd, K. B.; Shinn, N. D. *J. Vac. Sci. Technol. A* **1991,** *9*, 1518.

(49) Frederick, B. G.; Apai, G.; Rhodin, T. N. *Surf. Sci.* **1992,** *277*, 337.

(50) Guo, Q.; Moller, P. J. *Surf. Sci.* **1991,** *244*, 228-236.

(51) Bauer, E.; Poppa, H.; Todd, G.; Bonczek, F. *J. Appl. Phys.* **1974,** *45*, 5164.

(52) Ernst, N.; Duncomb, B.; Bozdech, G.; Naschitzki, M.; Freund, H. J. *Ultramicroscopy* **1999,** *in press*.

(53) Baglin, J. E. E. *Nucl. Instrum. Meth. Phys. Res. B* **1989,** *39*, 764.

CHAPTER 3

EFFECTS OF DEHYDROXYLATION ON CU INTERACTIONS WITH α-Al_2O_3(0001)

3.1. INTRODUCTION

This chapter reports on XPS studies which show that dehydroxylation of the α-Al_2O_3(0001) [sapphire(0001)] surface, by Ar^+ sputtering prior to Cu deposition, inhibits the formation of an initial Cu(I) conformal adlayer and promotes the formation of metallic Cu clusters. Furthermore, first principles calculations are used to study several varieties of hydroxylated surfaces and their affect on Cu adsorption at different coverages.

The interaction of metal adatoms with oxide substrates is of broad scientific and technological interest in areas such as heterogeneous catalysis, microelectronics, composite materials, and corrosion. A significant issue concerning the thermodynamics of the metal/oxide interaction is the strength of adatom binding compared with binding in two- or three-dimensional (2D or 3D) clusters on the oxide surface. For alumina surfaces, theoretical calculations indicate that all isolated metal adatoms transfer significant charge to the oxide (1, 2). If the resulting oxidized adatom is sufficiently bound, this then results in layer-by-layer conformal growth of the metal (Frank-van der Merwe, FM, growth mode (3, 4)), at least for the first 1-3 layers (Stranski-Krastanov, SK, mode (3, 4)). A weaker interaction, on the other hand, would result in the formation of 3D metal clusters (Volmer-Weber, VW, mode (3, 4)). An additional issue concerns the kinetics of the deposition process. If the barriers for adatom diffusion are sufficiently large compared

with the sample temperature, adatoms would be unable to diffuse to growing metal islands and a metastable FM structure could thus result.

Cu/Al_2O_3 interactions are of particular interest not only because of the technological relevance of this interface (5-7), but also because of inconsistencies in the reported results (8-18). Combined AES, EELS and LEED studies showed the SK mode of Cu growth and Cu(I) formation (~2Å thick) on α-Al_2O_3(0001) (8-10), and XPS studies yielded similar conclusions (11). In addition, a conformal overlayer of Cu on a thermally grown Al_2O_3 film on Al(111) was observed by AES and HREELS (12). Another study of Cu interactions with a thermal Al_2O_3 film grown on polycrystalline Al indicated Cu-O ionic bond formation at less than 0.5 ML Cu coverage (13). In contrast, some other studies of the Cu/α-Al_2O_3(0001) interface indicated that the interaction between Cu and the surface is weak, that Cu grows via the VW mode, and that metallic particles form from the very early stages of the Cu deposition (15-19). The growth of Cu metallic clusters on ordered Al_2O_3 ultrathin films was also reported (14), and the observed change of X-ray generated Cu(LMM) Auger line shapes and Auger parameters with Cu coverage was explained as being the result of the final state screening effect (14, 16, 18) (19) instead of reflecting different oxidation states.

The above inconsistencies suggest that Cu nucleation and growth on Al_2O_3 is a complex balance between various factors that are not necessarily well-controlled, even in typical ultra high vacuum (UHV) environments. Early cluster calculations (20, 21) suggested that Cu/Al_2O_3 should be a weakly interacting system (resulting in non-wetting and formation of 3D metallic nuclei (VW growth) even at low Cu coverages). However,

recent thick slab calculations of metal/sapphire interactions (1) and ultrathin Al_2O_3 film structure (2) have demonstrated that very large relaxations occur in this system and that these relaxations, not included in the cluster studies (20, 21), are critical for a correct energetic description. The above results have led to a collaborative experimental/theoretical effort (22) to understand "real world" Cu/Al_2O_3 interfaces.

Chapter 2 presents results from both density functional large slab calculations and experimental XPS which demonstrate that Cu will wet a hydroxylated α-Al_2O_3 (0001) (θ_{OH} ~0.47ML) surface at 300 K. An initial Cu(I) adlayer was observed with a maximum coverage of ~0.35ML (on a Cu/O atom basis), in excellent agreement with theory. At higher Cu coverages, a second, metallic Cu overlayer was observed to form over the initial Cu(I) adlayer. The calculations also indicated that thermodynamically and kinetically Cu should not wet a dehydroxylated α-Al_2O_3 (0001) surface at 300K, and suggested that the results should be sufficiently general as to apply to other metal/alumina systems.

In this chapter, XPS data are presented which show that maximum Cu (I) coverage on α-Al_2O_3(0001) at 300 K decreases with decreasing OH surface coverage. Dehydroxylation is accomplished by Ar^+ ion bombardment, followed by annealing in a partial pressure of O_2. Cu (I) formation on dehydroxylated sapphire(0001) is inhibited at 300K, with Cu(0) formation and 3D (VW) growth preferred. On the other hand, after exposure of a partially dehydroxylated surface to either air or ~2 Torr water vapor, the surface hydroxyl coverage recovers, which in turn enhances the formation of Cu(I) at Cu/α-Al_2O_3(0001) interface. These data demonstrate that the degree of surface

hydroxylation is indeed critical to the wetting behavior of Cu on the sapphire(0001) surface. The data also substantiate the predictions (22) of large slab calculations of Cu behavior on dehydroxylated sapphire(0001).

The atomic-scale structure of the hydroxylated sapphire surface in UHV is in fact unknown. However, its stability to over 1000K (22), which is not observed when a clean surface is hydroxylated in vacuum using a water plasma (23), suggests a crystalline form of aluminum hydroxide or oxy-hydroxide, where the greater stability can be explained as arising from a Madelung potential. A recent study of a fully hydrated α-Al_2O_3(0001) surface in the presence of water vapor (p>1 Torr) shows that the surface structure is an intermediate between α-Al_2O_3 and γ–$Al(OH)_3$ (24). This structure is oxygen terminated, with an adsorbed water layer sits above and stablizes the terminal oxgen layer. However, the structure may be different for a surface in UHV, since the adsorbed water layer may desorb. In general, one can conceive of two types of surface OH groups: ad-OH, which exist entirely above the surface, and in-surface OH, which are contained within the surface layer. In the case of water dissociation on sapphire(0001), one would expect one of each type to be made (25), the in-surface species arising from the reaction of H^+ with an O^{2-} ion. Here, using first principles slab calculations, we also investigate how each type of OH species affects the binding of Cu adatoms and a layer of Cu metal.

Section 3.2 contains a description of experimental and theoretical methods. Results are presented in section 3.3, and a discussion is contained in section 3.4. Summary and conclusions are presented in section 3.5.

3.2. EXPERIMENTAL AND THEORETICAL METHODS

Experiments were carried out in a combined UHV analysis/magnetron sputter deposition system which has been described previously in chapter 2. To tolerate high gas loading, the analysis and sputter deposition chambers were independently evacuated by turbomolecular pumps. Pressures in both chambers (in the absence of plasma) were monitored by nude ion gauges placed out of the line of sight from the sample. Base pressures were 7×10^{-10} Torr in the analysis chamber and 2×10^{-8} Torr in the deposition chamber. Typical working pressures were $1\text{-}5\times10^{-9}$ Torr in the analysis chamber and 4×10^{-8} -1×10^{-7} Torr in the deposition chamber. Pressures during plasma induced sputter deposition were monitored with a baratron gauge. A metal gate valve separated the two chambers when the sample was drawn out from analysis chamber to deposition chamber. Chamber isolation during sample analysis was achieved with differentially pumped Teflon seals against the polished double-walled manipulator rod.

The samples were $10 \times 10 \times 0.5$ mm square slabs of α-Al_2O_3 (Princeton Scientific) with one (0001) face polished optically flat. The samples were cleaned by sonication in acetone, methanol and deionized water consecutively prior to being mounted on a tantalum sample holder. The two tantalum leads of the sample holder were in contact with a liquid nitrogen reservoir. A combination of liquid nitrogen cooling and resistive heating of the sample holder permitted a variation of sample temperature between 130 K and 1200 K. Sample temperatures were monitored by a K-type thermocouple, spot-

welded at an edge of the sample holder and bent so that the junction was in contact with the sample surface.

XP spectra were acquired using a VG100AX hemispherical sector analyzer operated at constant pass energy of 50 eV. Calibration of the analyzer energy scale was carried out using sputter cleaned Cu and Au samples according to established techniques (26). Mg Kα X-ray radiation was obtained from a commercial, unmonochromatized source (Physical Electronics, PHI model 1427) operated at 15 kV and 300 W. Software for data acquisition and analysis have been described elsewhere (27). XP spectra were acquired with the sample aligned normal to the analyzer lens axis (normal incidence) and at 60° with respect to the normal incidence (grazing incidence). The sapphire samples showed significant differential charging (28-30), which is common in XPS studies of insulating materials. The details have been discussed in chapter 2. Briefly, the degree of charging for a given peak is a function of the inelastic mean free path (IMFP) and the take-off angle. Greater charging is observed for longer IMFP and normal incidence. Correction for such differential charging is more problematic than that for uniform charging, and this makes it difficult to obtain the exact binding energies. In this chapter, all the binding energies are reported without charging corrections. Characterization of Cu oxidation states is based on X-ray excited Auger spectral line shape instead of the absolute binding energies. The Cu Auger parameters (AP) were calculated according to the following:

$$AP = KE(Cu_{LMM}) + BE(Cu_{2p}) \quad (3.1)$$

$$KE(Cu_{LMM}) = h\nu - BE(Cu_{LMM}) \quad (3.2)$$

where KE and BE are kinetic energy and binding energy respectively. Although Auger parameters are insensitive to uniform charging, our results show that they are affected by differential charging. The AP values reported in this paper are not comparable with literature values. Again, our conclusions depend more on the Cu(LMM) lineshape rather than the absolute AP values.

A sputter ion gun (Physical Electronics, PHI model 04-191) in the analysis chamber was operated by direct argon gas feed into the ionization chamber with a variable excitation voltage of 1 – 5 KV. The samples were first annealed to 1100K for 1 hour in 5 $\times 10^{-6}$ Torr O_2, then exposed to brief Ar^+ bombardment (1 KeV) in order to remove adventitious carbon. Prior to Cu deposition, the samples were again annealed to 1100 K in 5×10^{-6} Torr O_2. Such a procedure is reported (23) to result in a sharp (1×1) hexagonal LEED pattern. Our previous XPS results (22) show that after the above treatment, the Al_2O_3(0001) surface is carbon free but still substantially hydroxylated. Cu deposition was carried out using a commercial water-cooled magnetron source (MiniMak) and an Argon plasma with a partial pressure of 0.015 Torr. The deposition rate could be controlled by adjusting the plasma power, and was shown to be highly reproducible. All Cu depositions reported in this paper were done at room temperature (~300 K).

Deionized H_2O (Biochemical Sciences, Inc.) was used in water exposure experiments. Several freeze-pump-thaw cycles were performed to purify the water. Low pressure ($<1.0\times10^{-5}$ Torr) water exposures were conducted in the main chamber, whereas high pressure experiments were carried out in the sample loading/deposition chamber to

tolerate high vapor loading. The pressure during water exposures was monitored by an ionization gauge in the main chamber and by a baratron gauge in the sample loading /deposition chamber. The pressure was maintained by adjusting water vapor leak-in rate through variable leak valves. Exposures are reported in Langmuir(L), $1L=10^{-6}$ Torr·sec. The reported exposures have not been corrected for pressure gauge sensitivity.

D.R. Jennison and co-workers (Sandia National Laboratories, Albuquerque, NM) performed theoretical work of this study. The theoretical work used density functional theory (31, 32) in the local density approximation (LDA) (33, 34), as implemented in the Vienna Ab-Initio Simulations Package (VASP) (35-37). Ultrasoft Vanderbilt pseudopotentials (38, 39) accurately replaced the core electrons at a plane wave cutoff of only 270 eV. Geometric relaxation was made using a damped molecular dynamics algorithm, until all forces were less than 0.05 eV/Å. The sapphire slab had six layers of

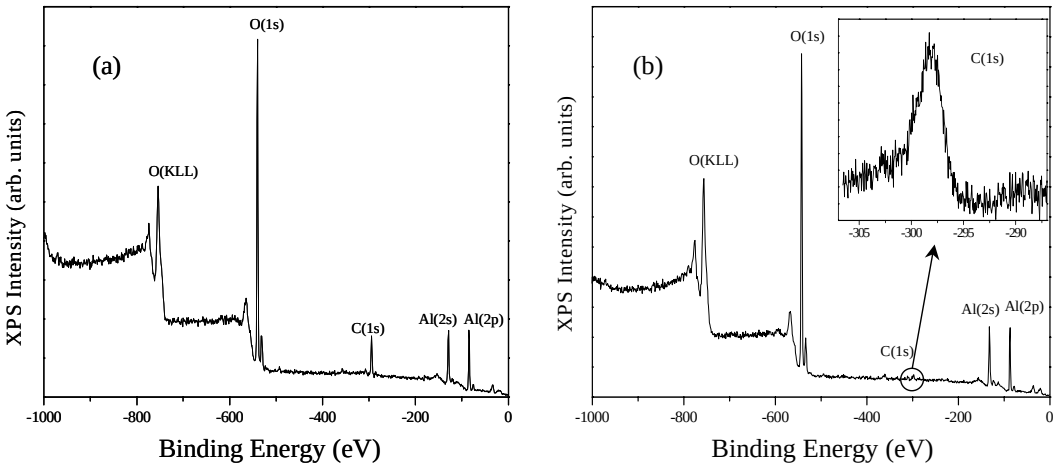

Figure 3.1. XPS survey scans of (a) an initial sapphire(0001) sample and (b) the sample after 1 hour annealing in 5 x 10^{-6} Torr O_2. Annealing removed most contaminants but left ~0.4ML strongly bound carbon on the surface.

the alumina unit cell, thus having six oxygen and twelve aluminum layers. The adsorbates were placed on one side, with the bottom three unit cell layers frozen in position at the bulk LDA geometry, which is within 0.2% of experiment. Because of long-range electrostatic interactions, the vacuum gap between the vertically repeating slabs always exceeded 18 Å.

3.2. RESULTS

3.2.1. Sapphire (0001) Surface Composition Change after Ar Ion Sputtering

Figure 3.1 shows a survey scan (normal incidence) for an initial sapphire sample, and a scan after annealing to 1100 K for 1 hour in 5×10^{-6} Torr O_2. The samples were initially covered by multi-layers of carbon, which indicates that either the ultra-sonic clean with acetone, methanol and deionized water was not enough to remove all the carbon on the sample completely, or carbon containing species saturated the surface

Table 3.1. O(1s)/Al(2p) area ratio($\pm$ 0.1)after various treatment of the sapphire(0001) surface. (Subsequent annealing in O_2 after 1, 2 KeV sputtering did not change the ratio.)

XPS Incidence	Initial sample	Annealed in O_2	Sputtered at 1 KeV	Sputtered at 2 KeV	Sputtered at 5 KeV	5 KeV sputtered+O_2 annealing
Normal	5.9	5.8	5.8	5.8	5.6	5.7
Grazing	6.2	6.4	6.4	6.2	5.8	5.9

immediately after cleaning. The annealing in oxygen significantly reduced the C(1s) signal. However, the remaining 0.4 ML C (based on the C to O atomic ratio, see Figure 1.b) was so stable that another hour of annealing in O_2 could not further reduce it. Ar^+ sputtering at 1KeV excitation energy and 25mA emission current for 6 minutes reduced the remaining carbon to undetectable levels.

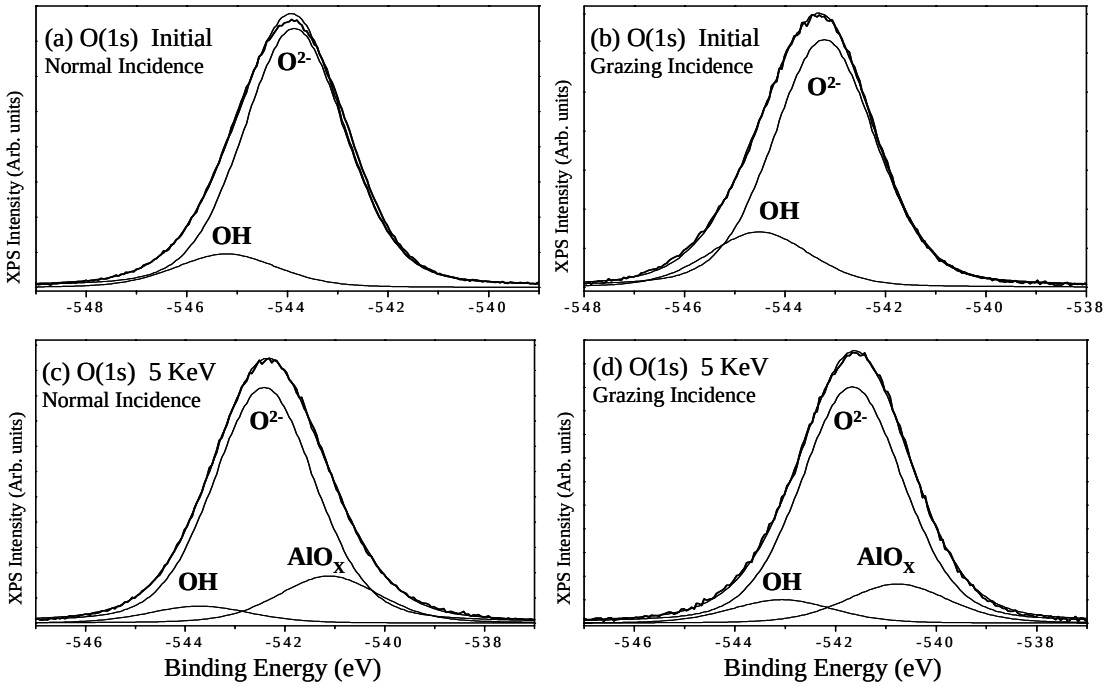

Figure 3.2. O(1s) spectra (without charging correction) of initial and 5 KeV Ar^+ sputtered sapphire (0001) surface: (a) Initial, normal incidence; (b) Initial, grazing incidence; (c) 5 KeV sputtered, normal incidence and (d) grazing incidence. The samples were all annealed in 5×10^{-6} Torr O_2 for 1 hour at 1100K before XPS analysis.

The O(1s)/Al(2p) ratio after various annealing and Ar^+ sputtering treatments are summarized in Table 3.1. In all cases grazing incidence XPS gave a higher O(1s)/Al(2p) ratio. Since the average sampling depth for 60° grazing incidence is only a half of that for

normal incidence, we conclude that there was oxygen enrichment on the surface. Annealing at 1100 K for one hour in UHV or in 5×10^{-6} Torr O_2 resulted in the same O(1s) and Al(2p) spectra and O(1s)/Al(2p) ratio. The O(1s) and Al(2p) spectra are shown in Figure 3.2 and Figure 3.3, respectively. The O(1s) spectra are well fit by two components each with FWHM of 2.4 eV, a main peak and a minor peak at 1.3 eV higher binding energy. In agreement with a previous report (11), the relative intensity of the high-energy peak is increased at grazing incidence, which indicates that this component corresponds to a surface species. Based on the known fact that the sapphire surfaces are difficult to make hydrogen free (25, 40, 41), we attribute this peak to surface hydroxylation. This has been further confirmed by water exposure experiment described in section 3.3.3, which shows that exposure of a partially dehydroxylated sapphire(0001) surface to water vapor results in recovery of this high binding energy feature. The 1.3 eV difference between the OH and main O(1s) features is in good agreement with previous reports (11).

Table 3.2. Cu coverage (ML) for maximum conformal Cu(I) growth and for equal Cu(I) and Cu(0) intensity in Cu(LMM) spectra.

Sample treatment	Annealing to 1100 K for 1 hour in O_2	1KeV Ar^+ sputtering + annealing	2KeV Ar^+ sputtering + annealing	5KeV Ar^+ sputtering + annealing
Conformal Cu(I)	0.24	0.35	0.24	0.12
$I_{Cu(I)} = I_{Cu(0)}$	0.48	0.72	0.48	0.24

These OH groups were sufficiently stable that they could not be removed either by another hour of annealing at 1100 K or by 6 minutes Ar^+ sputtering at 1 KeV. The

hydroxyl coverage was estimated to be ~0.47 ML using a method discussed previously (22). Ar^+ sputtering at 2 KeV for 10 minutes, on the other hand, was able to reduce the OH component to about 2/3 of the original value. The Al(2p) spectra did not change after 1 KeV or 2 KeV sputtering, and could be well fit by a single component. Both the O(1s) and Al(2p) spectra were stable upon subsequent annealing to 1100 K in O_2.

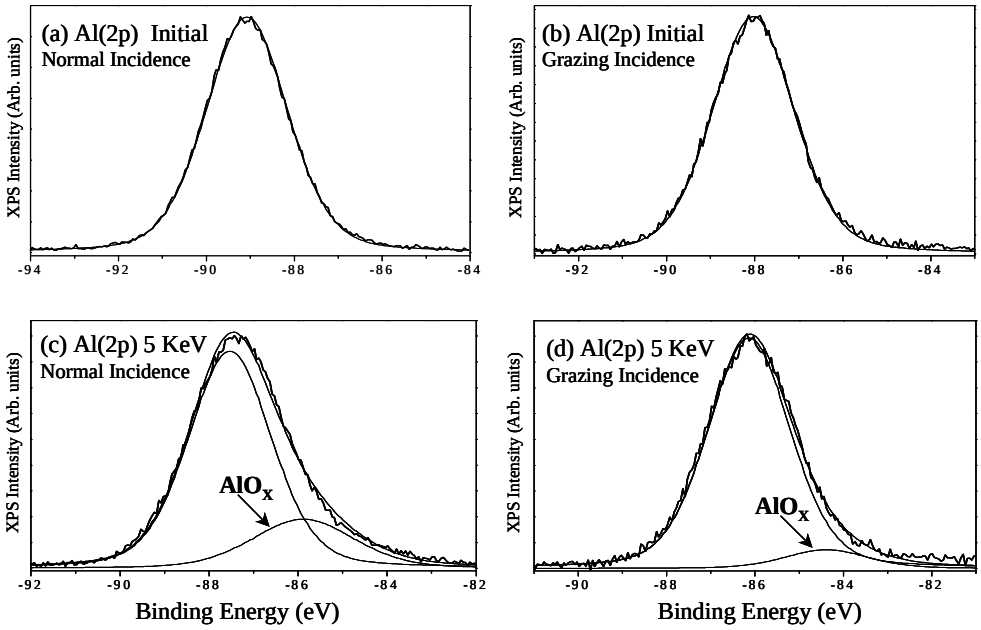

Figure 3.3. Al(2p) spectra(without charging correction) of sapphire(0001): (a) Initial, normal incidence; (b)Initial, grazing incidence; (c) 5 KeV Ar^+ sputtered, normal incidence and (d) grazing incidence. The initial spectra are well fit by a single peak with FWHM of 2.2 eV. After 5 KeV Ar^+ sputtering a metallic Al peak appeared at 1.7eV lower binding energy than the main peak. The percentage of Al(0) peak area (21.3% for normal incidence and 7.5% for grazing incidence) showed that the Al(0) was located beneath the surface layer which itself was fully oxidized.

As shown in Table 3.1, significant changes of the O(1s) and Al(2p) spectra occurred after 10 minutes Ar^+ sputtering at 5 KeV followed by annealing in O_2. The O(1s)/Al(2p) intensity ratio decreased by 10% for grazing incidence (from 6.4 to 5.8). Subsequent annealing in O_2 increased this ratio by 2%, indicating a reaction of O_2 with the sputtered

surface. Sputtering caused both O(1s) and Al(2p) spectra became wider (Figs. 3.2 and 3.3). The OH component decreased to about a half of the initial value. Another component appeared at a binding energy 1.1 eV lower than the main oxygen peak. The emergence of this component coincided with the partial reduction of Al^{3+}, as shown in Figures 3.3(c) and 3.3(d). The metallic Al(2p) feature is more prominent in the normal incidence spectrum, its contribution to the total Al(2p) area being about 21%, in contrast to 8% in the grazing incidence case. This difference is an indication that the metallic Al on the surface was oxidized during O_2 annealing, while that beneath the surface remained. The low binding energy O(1s) peak also showed enrichment beneath the surface, and we assign it to the oxygen bound to the partially reduced aluminum. The charging decreased by ~1.7 eV for both O(1s) and Al(2p) peaks after 5 KeV Ar^+ sputtering, as shown in figs. 3.2 and 3.3, which may be an effect of partial aluminum reduction.

The above results show that Ar^+ sputtering at energies higher than 2 KeV decreases the surface hydroxyl concentration. The changes in the O(1s) and Al(2p) spectra indicate that oxygen vacancies were created by Ar^+ sputtering. Subsequent annealing in O_2 refills the vacancies in the top layer(s), but a significant amount of partially reduced Al remained beneath the surface. Any changes to surface topography, of course, cannot be determined from the data.

3.3.2. Cu Nucleation Studies

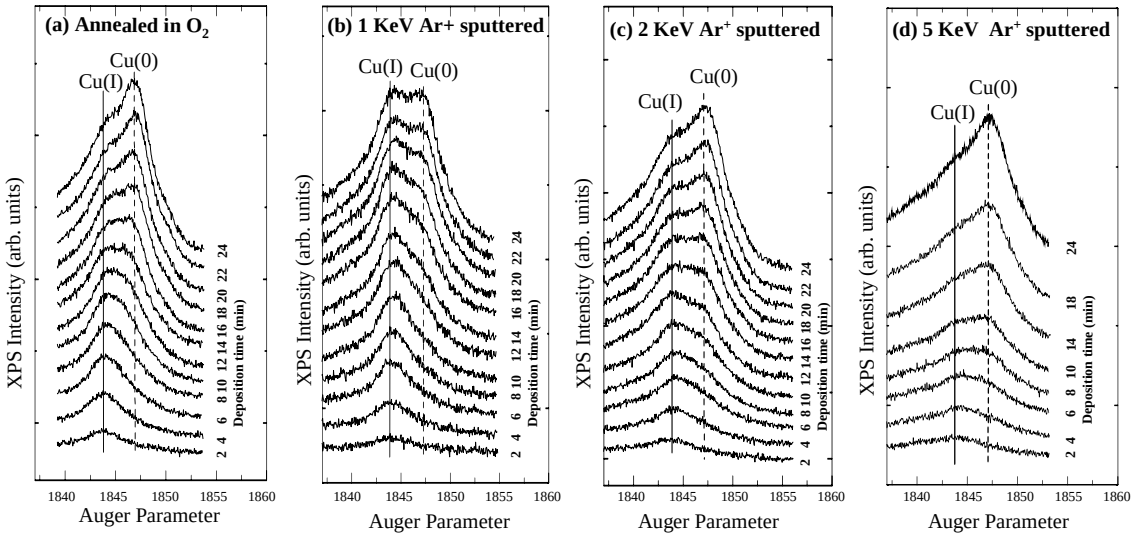

Figure 3.4. X-Ray excited Cu(LMM) evolution during Cu deposition on sapphire(0001): (a) annealed in O_2 only, (b) 1 KeV lightly sputtered, (c) 2 KeV sputtered, and (d) 5 KeV heavily sputtered. All were annealed in O_2 before Cu deposition. Dehydroxylation of the surface resulted in the decrease of the Cu(I) component.

Copper deposition was performed on sapphire (0001) surfaces after different treatments: (a) annealing in O_2 only (θ_{OH} = ~0.47 ML); (b) 1 KeV Ar^+ sputtering , then annealing in O_2 (θ_{OH} = ~0.47 ML); (c) 2 KeV Ar^+ sputtering, then annealing in O_2 (θ_{OH} = ~0.31 ML); (d) 5 KeV Ar^+ sputtering, then annealing in O_2 (θ_{OH} = ~0.23 ML). The deposition rate was controlled to be constant at 0.03 ML per minute. After every 2 minutes of deposition, the sample was transferred to the analysis chamber and XPS was used to monitor the growth of Cu. The evolution of the X-ray excited Cu(LMM) Auger electron spectrum with deposition time is shown in Figure 3.4. There are two distinguishable features with AP (Auger parameter) values of 1843.9 and 1847.3 eV.

Literature (42) AP values for Cu(I) and Cu(0) are ~1849.1 and 1851.3 eV respectively. The difference between observed Auger parameters and literature values is attributed to differential charging, as previously reported (22). No shake-up satellite peaks that are characteristic for Cu(II) (11, 42, 43) were observed in the Cu(2p) spectra (Figure 3.5).

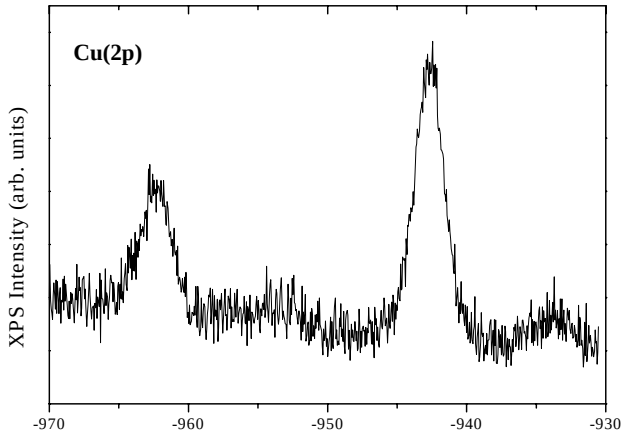

Figure 3.5. Cu(2p) spectrum at Cu coverage of 0.06ML (based on Cu/O atomic ratio). No shake-up satellite peaks that is characteristic of Cu(II) were observed.

After annealing an as-received sample, the remaining 0.4 ML of carbon on the surface apparently occupied some active sites and prevented Cu(I) formation (Fig.3.4a). Brief 1 KeV Ar^+ sputtering resulted in a carbon free surface. The Cu(2p)/O(1s) intensity ratio as a function of Cu sputter deposition time are displayed in Fig. 3.6 for 1 KeV and 5 KeV sputtered surfaces. Results obtained for the 2 KeV sputtered surface were intermediate between the two cases shown, but are omitted in Fig. 3.6 for clarity. In all

cases, the uptake curve shows a sharp break, which indicates the end of a conformal initial growth stage. A comparison of Figs. 3.5 and 3.6 indicates that Cu(I) is initially formed, with subsequent formation of Cu(0). The maximum coverages of Cu(I) are 0.35, 0.24, and 0.12 ML for 1, 2, and 5 KeV Ar^+ sputtered surfaces respectively (Table 3.2).

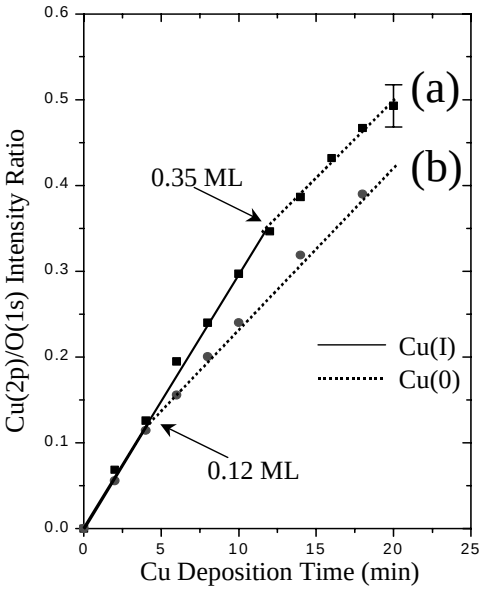

Figure 3.6. Uptake curves of Cu on (a) 1 KeV and (b) 5 KeV Ar^+ sputtered sapphire(0001). The breaks coincided with the Cu(LMM) lineshape changes. The growth of Cu(I) stopped much earlier in the case of 5 KeV sputtered (and dehydroxylated)surface.

3.3.3. H_2O Exposure Effects

To further confirm that the Cu/α-Al_2O_3(0001) interaction is in deed affected by surface hydroxylation, water and air experiments were carried out. Aware of the difficulty of preparing a hydrogen free sapphire(0001) surface(25, 40, 41), we partially dehydroxylated a sapphire sample by 2 KeV Ar^+ sputtering for 30 minutes, followed by

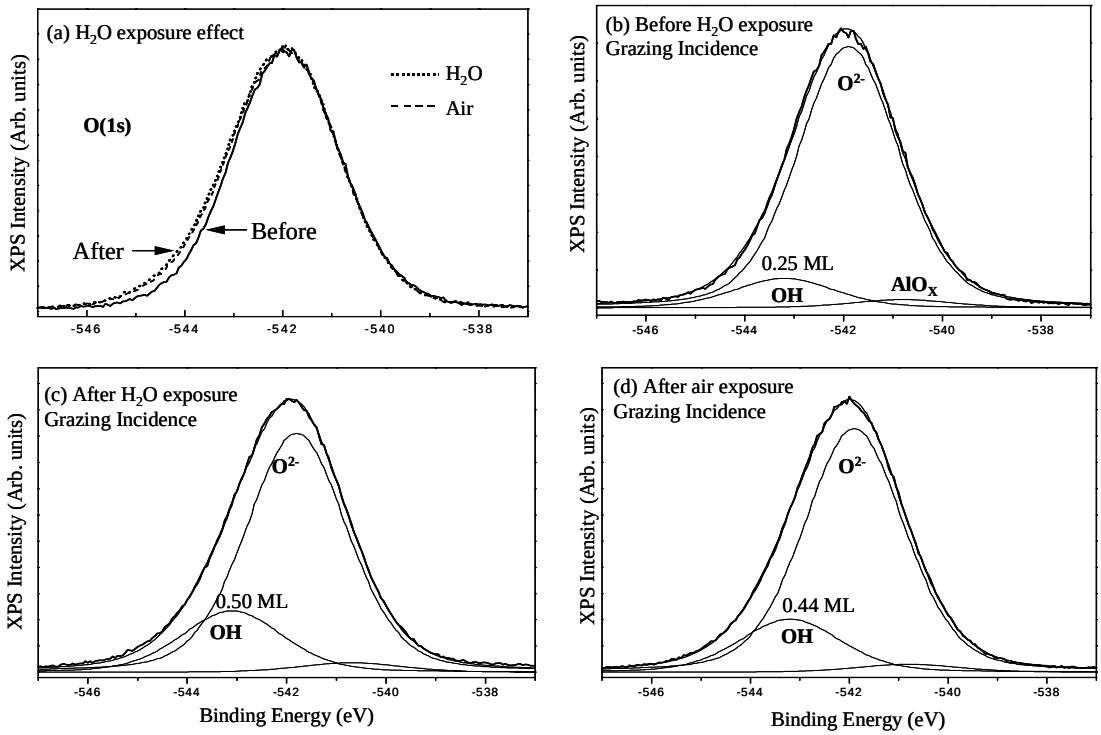

Figure 3.7. Grazing incidence O(1s) spectra for sapphire(0001) surface (without charging correction): (a) 2 KeV Ar^+ sputtered surface before and after exposure to air and 2 Torr H_2O at 300 K, increase of the higher BE side observed; (b) before exposure (dehydroxylated by 2 KeV Ar^+ sputtering for 30 min); (c) after exposure to 2 Torr water vapor; (d) after exposure to air.

annealing at 1100K in 5×10^{-6} Torr O_2 for 1 hour. O(1s) peak fitting (fig. 3.7b) indicates the surface hydroxyl coverage decreased from 0.47 ML to 0.25 ML after the above treatment. A peak corresponding to partially reduced Al_2O_3 was also observed, but its contribution to the total area is lower than 3%. These defects are expected to be located beneath the surface, since those in the top layer(s) of the surface should have been fully repaired after annealing in O_2 (see section 3.3.1).

The above method (2 KeV Ar+ sputtering for 30 minutes) was used to prepare sapphire samples for water exposure experiments. One such dehydroxlated sample was exposed to 5×10^{-7} Torr water vapor in the main chamber for 20 minutes (600L). XP

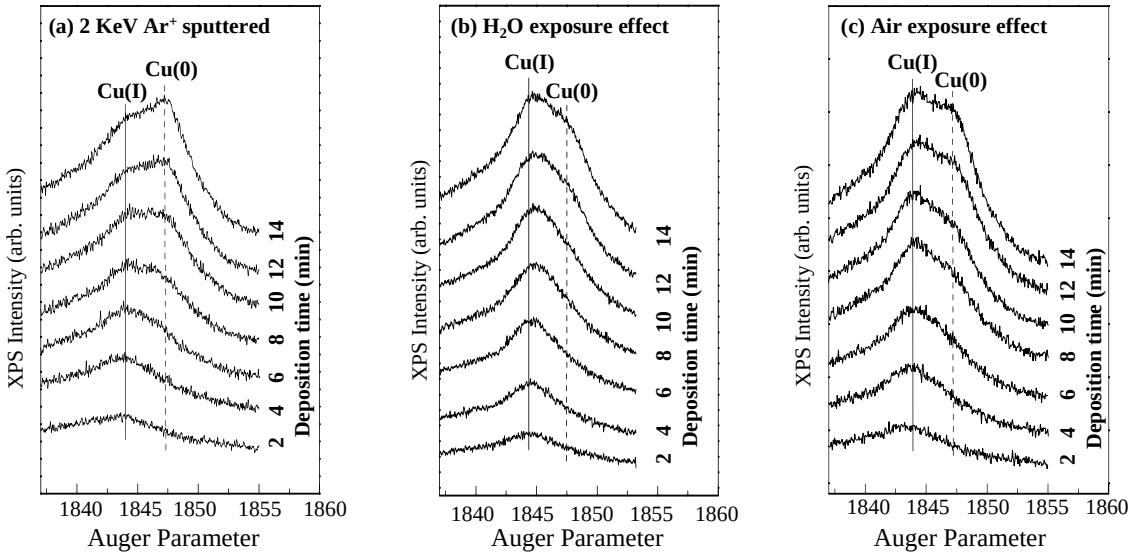

Figure 3.8. X-ray-excited Cu(LMM) evolution during Cu deposition on sapphire(0001): (a) dehydroxylated by 2 KeV Ar^+ sputtering for 30 min; (b) dehydroxylated then exposed to 2 Torr water vapor; (c) dehydroxylated then exposed to air. Increase of surface hydroxylation promotes Cu(I) formation.

spectra of O(1s) showed no change after this low pressure water exposure. The sample was retracted to the sample loading/deposition chamber. Water vapor was then leaked in. After H_2O exposure at 2 torr for 20 minutes, the sample was sent to the main chamber for XPS analysis. A brief 1 KeV Ar^+ sputtering (1 minute) was able to remove carbon contamination completely. The O(1s) peak became wider at the higher binding energy side(fig. 3.7a), which is a direct proof that the higher binding energy feature in O(1s) spectrum is really due to surface hydroxylation. Peak fitting (fig. 3.7c) shows that the OH component increased from 0.25 ML to 0.50 ML. The absence of re-hydroxylation after exposure to 5×10^{-7} Torr water vapor is consistent with recent studies which show

that conversion of α-Al_2O_3 to a hydroxide at ~300 K occurs only at partial pressure of H_2O greater than 1 Torr (24, 44).

For comparison, an air exposure experiment was performed. A partially dehydroxylated sapphire sample was retracted to the loading chamber and exposed to air (by turning off the pumps for the loading chamber). The chamber was pumped down again after 30 minutes. When the pressure in this chamber reached 5×10^{-7} Torr, the sample was sent to the analysis chamber. Brief 1 KeV Ar^+ sputtering (6 min) was performed to remove unavoidable carbon contamination during air exposure. O(1s) peak fitting (fig. 3.7d) shows that the surface hydroxyl recovered from 0.25 ML to 0.44 ML.

Cu deposition was then performed on sapphire samples after the above treatments. Deposition conditions were the same as those described in section 3.3.2. The evolution of the X-ray excited Cu(LMM) Auger electron spectrum is displayed in fig. 3.8. As shown in fig. 3.8a, for the partially dehydroxylated surface, the high Auger parameter Cu(0) feature dominates after Cu deposition for 14 minutes (~0.42 ML Cu coverage). However, for samples exposed to 2 Torr water vapor or air, the low Auger parameter Cu(I) feature still dominates at the same Cu coverage (Figs. 3.8b and 3.8c). It is thus evident that the OH coverage increase results from H_2O or air exposure does improve the Cu(I) formation at the Cu/α-Al_2O_3(0001) interface.

Table 3.3. Cu adatom binding energies, in eV on a per atom basis, for different sapphire (0001) surfaces. OH(a) is ad-OH, OH(s) is in-surface OH; if present, all are at 1/3 ML.

Species	Clean	Clean+OH(a)+OH(s)	Clean + OH(a)
Cu 1/3 ML	1.8	1.8	5.2
Cu 1 ML	0.5	0.3	1.2

3.3.4. Theoretical Studies

Table 3.3 shows the computed LDA binding energies (on a per atom basis) for adsorbed Cu (oxidized adatoms at 1/3 ML coverage and metallic Cu at 1ML coverage) on different surfaces. The following cases were considered: 1) a clean sapphire surface, 2) clean plus 1/3 ML of ad-OH and 1/3 ML of in-surface-OH (as would be produced by the dissociation of 1/3 ML of water [25], and 3) clean plus 1/3 ML of ad-OH. (See Fig. 3.9 for a visualization of these species) It is seen that the in-surface species (cf. surfaces #2 and #3) weakens the adatom binding to the point where it almost exactly counteracts the strengthening affect of ad-OH (cf. #2 and #1). Indeed, the latter species sufficiently strengthens adatom binding (cf. #3 and #1) to: a) reverse the Born-Haber cycle prediction of not wetting the clean surface (22), and b) presumably pin the adatoms at room temperature so diffusion across the surface does not occur. Indeed, it would cost ~ 3 eV in energy for the adatom to separate from the ad-OH.

Finally, noting the strong increase in adatom binding that would occur on surface #2 if the in-surface-OH would give up its hydrogen, D.R. Jennison and co-workers computed the energetics of the reaction $2Cu(a) + 2OH(a) + 2OH(s) \rightarrow 2Cu(a) + 2OH(a)$

+ H_2(g) +2O(s), where a, g, and s stand for adsorbed, gas, and in-surface species, respectively. The results indicate it is exothermic by 0.8 eV (LDA) for the presence of two Cu adatoms to cause the dissociation of neighboring in-surface OH and the evolution of hydrogen gas. However, because LDA overbinds the hydrogen molecule to an unusual extent, it is likely that the actual energy released would be less.

3.4. DISCUSSION

The data show that the extent of Cu(I) formation on α-Al_2O_3(0001) at 300K decreases with decreasing hydroxyl coverage. On a carbon free, substantially hydroxylated surface (θ_{OH} = ~0.47 ML), deposited Cu grows conformally as Cu(I) to a maximum coverage of ~0.35ML, in accord with theoretical predictions (22) of a maximum coverage of 0.33ML, limited by Cu(I) –Cu(I) repulsion (Figs. 3.4b and 3.6). Reducing the initial OH coverage reduces the corresponding maximum Cu(I) coverage at 300K (Table 3.2, Fig. 3.6). This clearly demonstrates that the formation of Cu(I) at the sapphire(0001) surface at 300K is due specifically to the interaction of Cu adatoms with hydroxyl groups. These data therefore provide an explanation for the inconsistencies in the literature concerning Cu(I) observation and also the reports of Cu wetting vs. non-wetting of alumina surfaces (8-18). A related interaction has been reported for Rh on hydroxylated alumina thin films (7), where it has been suggested that ad-OH groups serve to nucleate metal islands. While this claim has been supported by theoretical calculations of metal dimer stability (45), the OH density in Ref. (7) was apparently much less than that reported here.

The nature of hydroxyl groups on sapphire(0001) surfaces, and their thermal stability, is itself a matter of some controversy. Several publications (23, 46) report that all OH groups formed by the exposure of sapphire(0001) surfaces to water vapor in vacuum are removed by heating to ~600K, in agreement with studies on alumina powdered samples and thin films (47). In contrast, ion scattering studies (40) indicate that substantial surface hydroxylation can persist even after heating above 1400K. The latter results are in accord with our previous results (22) and those reported here as, in our experiments, surface hydroxylation was not removed by annealing in UHV to 1100K. At least part of the reason for this discrepancy may be the possibility of several different types of OH containing structures on a sapphire (0001) substrate. Supporting evidence for this explanation derives from the different OH XPS binding energies observed when hydroxylation occurs by different means: when produced by exposure to water vapor under UHV or high vacuum conditions, a binding energy ~2.0eV higher than the main O(1s) peak is found (44); exposure to 10 Torr water vapor results in a binding energy only 1.7eV from the main O(1s) feature, consistent with the formation of an aluminum hydroxide phase (44). The threshold H_2O pressure is found to be ~1 Torr to fully hydroxylate the α-Al_2O_3(0001) surface (44). The OH feature observed in our studies displays a 1.3eV shift from the main O(1s) peak, in agreement with a 1.4eV shift reported in a previous XPS study (11). In our case, surface hydroxylation is certainly due to exposure of the sapphire surface to the atmosphere prior to introduction into the vacuum chamber, rather than to the chamber ambient. In fact, exposure of a dehydroxylated surface to 5×10^{-7} Torr water vapor resulted in no significant increase in surface hydroxyl

coverage. On the other hand, exposure of a dehydroxylated surface to 2 Torr water vapor or to air does increase the surface hydroxyl to about the same level as when the sample was first introduced to the UHV chamber from air. The saturation surface hydroxyl coverage in UHV is about 0.5 ML, which is far less than what has been reported for a fully hydrated α-Al_2O_3(0001) surface (24). A possible explanation is that the adsorbed water layer that sits above and stablizes the terminal oxygen layer desorbs easily in UHV, leaving only hydroxyl groups strongly bound to the surface.

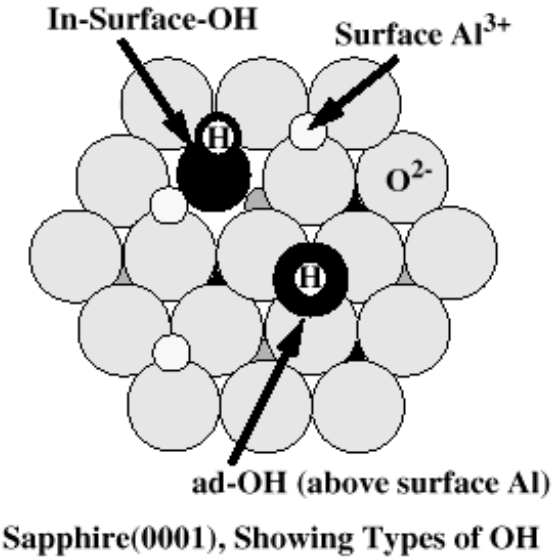

Figure 3.9. The α-Al_2O_3(0001) surface showing an example of the in-surface and the ad-OH species. The ad-OH prefers to sit directly above a surface Al ion, while the in-surface species tilts somewhat to further separate the positive hydrogen region from the neighboring Al sites.

The theoretical results indicate that the increased stability of Cu(I) in the presence of ad-OH is due to a deepening of the electrostatic well in which the oxidized, positively charged, Cu sits. This is caused by the addition of a negatively charged lateral neighbor. In contrast, the presence of a neighboring in-surface-OH reduces the binding compared

with the perfect surface, because a neighboring charge is reduced from ~ –2 (an oxygen ion) to ~ –1 (the OH). The calculations show, if a surface were saturated with even amounts of both types of OH, the net effect on the heat of adsorption of Cu adatoms would be close to zero, in agreement with recent microcalorimetry experiments (48). However, the calculations also indicate that if Cu were to be deposited on such a surface, the in-surface species could be depleted, because it is energetically favorable to dissociate the in-surface species, releasing hydrogen gas, and thus strongly increasing the binding of nearby Cu adatoms.

The data do not reveal any loss in OH due to the Cu/OH interaction. XPS spectra taken after Cu deposition and after annealing (to induce Cu dewetting), show no observable change of OH intensity, whereas a decrease in OH surface coverage is observable after Ar^+ bombardment. The data therefore suggest that Cu(I) formation is not accompanied by OH decomposition. While the lack of resolution of the OH feature in the O(1s) spectra (e.g, Fig. 3.2) limits the definitiveness of such a conclusion, if ad-OH and in-surface-OH were present in comparable numbers, we could not explain the increase in ad-Cu binding necessary to permit Cu(I) to be observed at room temperature and be stable to > 1000K. We therefore suggest that the hydroxylated surface studied here is an aluminum oxy-hydroxide film on sapphire, consisting largely of a close packed plane of O^{2-} (with a normal component of neighboring Al ions) but a substantial coverage of ad-OH above that plane. Further structural details remain unknown.

Finally, since Ar^+ sputtering was used to dehydroxylate sapphire(0001) surface, the implanted Ar^+ has a potential influence on the surface electronic structure. Based on the

Ar(2p) to O(1s) peak area ratio and XPS sensitivity factors provided by the XPS analyzer manufacturer(VG), the atomic concentration of implanted Ar^+ can be estimated. For the worst case, i.e. 5 KeV sputtering for 10 minutes, the calculated atomic percentage of Ar is 4.0% from normal incidence spectra, and 1.8% from 60° grazing incidence spectra, indicating the implanted Ar ions are mainly located below the surface. The concentration of Ar increases with sputtering time. Subsequent annealing at 1100K could not remove the implanted Ar significantly. This is a limiting factor that prevents us from preparing a completely dehydroxylated surface. Small amount of implanted Ar ions, however, do not affect the Cu/α-Al_2O_3(0001) interface behavior. In the water exposure experiment (section 3.3), the three samples were prepared in exactly the same way, and the implanted Ar ions were also at the same level. The only difference between these samples was the degree of the surface hydroxylation. Thus the critical factor that controls the Cu α-Al_2O_3(0001) interactions must be the surface hydroxyl coverage, other than the implanted Ar ions or the surface topography change caused by Ar^+ sputtering.

3.5. CONCLUSIONS

Experimental studies have examined the effects of surface dehydroxylation on the interactions at Cu/α-Al_2O_3(0001) interface. The results indicate:

(1) Ar^+ sputtering at 2 KeV or higher resulted in dehydroxylation of the surface;

(2) Ar^+ sputtering at 5 KeV creates oxygen vacancies in the surface region. Only vacancies in the top layer(s) can recover by subsequent annealing in O_2, while those beneath the surface remain.

(3) Dehydroxylation of sapphire(0001) results in weaker overall Cu/Al_2O_3 interaction. Conformal growth of Cu(I) stops earlier and formation of Cu(0) clusters dominates thereafter.

(4) Exposure of a dehydroxylated sapphire(0001) surface to 2 Torr water vapor or to air results in recovery of surface hydroxyl coverage. Increase of surface hydroxylation promotes the initial Cu(I) formation at the Cu/sapphire(0001) interface.

(5) The hydroxylated surface produced by atmospheric exposure contains ad-OH groups, which stabilize Cu adatoms, while in-surface OH groups, which destabilize Cu adatoms, are absent or are a minority species.

3.6. CHAPTER REFERENCES

(1) Verdozzi, C.; Jennison, D. R.; Schultz, P. A.; Sears, M. P. *Phys. Rev. Lett.* **1999,** *82*, 799-802.

(2) Bogicevic, A.; Jennison, D. R. *Phys. Rev. Lett.* **1999,** *82*, 4050.

(3) Argile, C.; Rhead, G. E. *Surf. Sci. Rep.* **1989,** *10*, 277.

(4) Feldman, L. C.; Mayer, J. W. *Fundamentals of Surface and Thin Film Analysis*; P T R Prentice-Hall, Inc.: Englewood Cliffs, NJ, 1986.

(5) *National Technology Roadmap for Semiconductors*; Semiconductor Industry Association: San Jose, CA, 1997.

(6) Wu, M.-C.; Goodman, D. W. *J. Phys. Chem.* **1994,** *98*, 9874-9881.

(7) Ertl, G.; Freund, H.-J. *Physics Today* **1999,** *52*, 32-38.

(8) Guo, Q.; Moller, P. J. *Surf. Sci.* **1991,** *244*, 228-236.

(9) Guo, Q.; Moller, P. J.; Gui, L. *Acta Physica Polonica A* **1992,** *81*, 647-651.

(10) Moller, P. J.; Guo, Q. *Thin Solid Films* **1991,** *201*, 267-279.

(11) Varma, S.; Chottiner, G.; Arbab, M. *J. Vac. Sci. Technol. A* **1992,** *10*, 2857-2862.

(12) Chen, J. G.; Colaianni, M. L.; Weinberg, W. H.; Yates, J.T. Jr. *Surf. Sci.* **1992,** *279*, 223-232.

(13) Ohuchi, F. S.; French, R. H.; Kasowski, R. V. *J. Appl. Phys.* **1987,** *62*, 2286-2289.

(14) Wu, Y.; Garfunkel, E.; Madey, T. E. *J. Vac. Sci Technol. A* **1996,** *14*, 1662-1667.

(15) Gota, S.; Gautier, M.; Douillard, L.; Thromat, N.; Duraud, J. P.; Fevre, P. L. *Surf. Sci.* **1995,** *323*, 163-174.

(16) Gautier, M.; Van, L. P.; Duraud, J. P. *Europhys. Lett.* **1992,** *18*, 175-180.

(17) Gautier, M.; Duraud, J. P.; Van, L. P. *Surf. Sci. Lett.* **1991,** *249*, L327-L332.

(18) Vijayakrishnan, V.; Rao, C. N. R. *Surf. Sci. Lett.* **1991,** *255*, L516-L522.

(19) Carley, A. F.; Rajumon, M. K.; Roberts, M. W. *J. Solid State Chem.* **1993,** *106*, 156-163.

(20) Castro, V. D.; Polzonetti, G.; Zanoni, R. *Surf. Sci.* **1985,** *162*, 348.

(21) Johnson, K. H.; Pepper, S. V. *J. Appl. Phys.* **1982,** *83*, 6634.

(22) Kelber, J. A.; Niu, C.; Shepherd, K.; Jennison, D. R.; Bogicevic, A. *Surf. Sci.* **2000,** *446*, 76-88.

(23) Elam, J. W.; Nelson, C. E.; Cameron, M. A.; Tolber, M. A.; George, S. M. *J. Phys. Chem. B* **1998,** *102*, 7008-7015.

(24) Eng, P. J.; Trainor, T. P.; Brown, G. E.; Waychunas, G. A.; Newville, M.; Sutton, S. R.; Rivers, M. L. *Science* **2000,** *288*, 1029-1033.

(25) Hass, K. C.; Schneider, W. F.; Curioni, A.; Andreoni, W. *Science* **1998,** *282*, 265-268.

(26) Powell, C. J. *Surf. Interface Anal.* **1995,** *23*, 121.

(27) Martini, D.; Shepherd, K.; Sutcliffe, R.; Kelber, J. A.; Edwards, H.; Martin, R. S. *Apllied Surf. Sci.* **1999,** *141*, 89-100.

(28) Cazaux, J.; Lehuede, P. *J. Electron Spectrosc. Relat. Phenom.* **1992,** *59*, 49-71.

(29) Pertsin, A. J.; Pashunin, Y. M. *Applied Surf. Sci.* **1990,** *44*, 171-178.

(30) Barr, T. L. *J. Vac. Sci. Technol. A* **1989,** *7*, 1677-1683.

(31) Hohenberg, P.; Kohn, W. *Phys. Rev. B* **1964,** *136*, B864.

(32) Kohn, W.; Sham, L. J. *Phys. Rev. A* **1965,** *140*, A1133.

(33) Perdew, J. P.; Zunger, A. *Phys. Rev. B* **1981,** *23*, 5048.

(34) Ceperley, D. M.; Alder, B. J. *Phys. Rev. Lett.* **1980,** *45*, 566.

(35) Kresse, G.; Hafner, J. *Phys. Rev. B* **1993,** *47*, 558.

(36) Kresse, G.; Hafner, J. *Phys. Rev. B* **1994,** *49*, 14251.

(37) Kresse, G.; Hafner, J. *Phys. Rev. B* **1996,** *54*, 11169.

(38) Vanderbilt, D. *Phys. Rev. B* **1985,** *32*, 8412.

(39) Vanderbilt, D. *Phys. Rev. B* **1990,** *41*, 7892.

(40) Ahn, J.; Rabalais, J. W. *Surf. Sci.* **1997,** *388*, 121-131.

(41) McHale, J. M.; Auroux, A.; Perrotta, A. J.; Navrotsky, A. *Science* **1997,** *277*, 788-791.

(42) Moulder, J. F.; Stickle, W. F.; Sobol, P. E.; Bomben, K. D.; Chastain, J.; King, R. C. *Handbook of X-ray photoelectron spectroscopy*; Physical Electronics, Inc.: Eden Prairie, Minnesota, 1995.

(43) Wandelt, K. *Surf. Sci. Rep.* **1982,** *2*, 1.

(44) Liu, P.; Kendelewicz, T.; G.E. Brown, J.; Nelson, E. J.; Chambers, S. A. *Surf. Sci.* **1998,** *417*, 53-65.

(45) Bogicevic, A.; Jennison, D. R. *Surf. Sci.* **1999,** *437*, L741.

(46) Nelson, C. E.; Elam, J. W.; Cameron, M. A.; Tolbert, M. A.; George, S. M. *Surf. Sci.* **1998,** *416*, 341-353.

(47) Frederick, B. G.; Apai, G.; Rhodin, T. N. *Surf. Sci.* **1992,** *277*, 337.

(48) Campbell, C. T. *(unpublished results)* .

CHAPTER 4

INTERFACE OF $Ni_3Al(111)$ AND ULTRATHIN Al_2O_3 FILM UNDER STM-INDUCED HIGH ELECTRIC FIELDS

4.1. INTRODUCTION

The chemical and electronic behavior of ultrathin oxide films on metal substrates is of considerable significance in various fields, including catalysis (1), corrosion (2) and tunneling-based electronics (3-5). The application of even a modest bias (1-3 V) across a thin oxide film leads to an extremely high electric field. Gate oxide dielectric breakdown under high electric field is a major cause of failure for ULSI devices (6). Dielectric breakdown of thin SiO_2 films has been studied extensively (6-14). The breakdown is generally associated with the formation of traps or defects inside the oxide (10, 14, 15) and at the interfaces (8, 15). In order to increase the gate capacitance and the transistor gain, the thickness of the gate oxide in commercial integrated circuits has been reduced to below 4 nm (16, 17), which is within the direct tunneling distance. Due to large leakage current, SiO_2 will have difficulty sustaining further downscaling (16). Al_2O_3 is an attractive alternative with a higher dielectric constant -- 8.5 (18) vs. 3.9 for SiO_2 (19). The same gate capacitance can be achieved by using Al_2O_3 that is twice as thick as SiO_2. Al_2O_3 also has potential use as insulating barriers in magnetoresistance tunnel junctions (4, 5, 20, 21). The thickness of such tunneling barriers is usually 1.0-2.0 nm. In both cases, the behavior of thin Al_2O_3 films under high electric field is of critical importance.

Thin Al_2O_3 films serve as corrosion barriers for aluminum and aluminum alloys. Studies have shown that the current due to the mobile ions in these barriers increases exponentially under high electric field (22, 23). The phenomenon of "pitting" (localized corrosion and dielectric breakdown of the passive films) is often observed under electrochemical conditions (applied potential or anion absorption) that are associated with the generation of electric fields greater than 1MV/cm (24, 25). High field behavior study of such films is directly relevant to understanding corrosion of Al and Ni-Al "superalloys".

Scanning tunneling microscopy (STM) is a promising tool to characterize thin oxide films with thickness in the tunneling regime (<3nm) (26-29). It has been recently utilized to study the dielectric breakdown of ultra-thin SiO_2 films (30-33). Because the probe to sample distance is usually less than 5 nanometers, STM has the ability to generate very high electric fields using modest bias voltages (less than 6 V). High spatial resolution in STM also allows for systematic study of the effects of high electric field on the morphology and composition of a surface, which directly leads to the understanding of the intrinsic dielectric characteristics of the film at nanometer-scale resolution.

Single-crystal Ni-Al alloys have been used as substrates to prepare ultrathin aluminum oxide films (34-38). After exposing the substrates to oxygen (partial pressure $< 10^{-6}$ Torr) and annealing at temperatures of 700 to 1200 K, well-ordered γ'-Al_2O_3 films can be formed with thickness in the sub-nanometer range (34-36, 38-42). In this chapter, we report the use of high electric fields applied via the STM to induce both interfacial voids and dielectric breakdown of ultra-thin γ'-Al_2O_3 films (~7 Å thick) grown on

$Ni_3Al(111)$ substrates. The results show that the critical breakdown field is 12.3 ± 1.0 MV/cm. At lower fields, small voids (or pits) at the metal/oxide interface can be created. The voids grow larger and deeper after prolonged exposure to relatively low electric field. The pitting process degrades the dielectric strength of the γ'-Al_2O_3 film and lowers the threshold field required for dielectric breakdown.

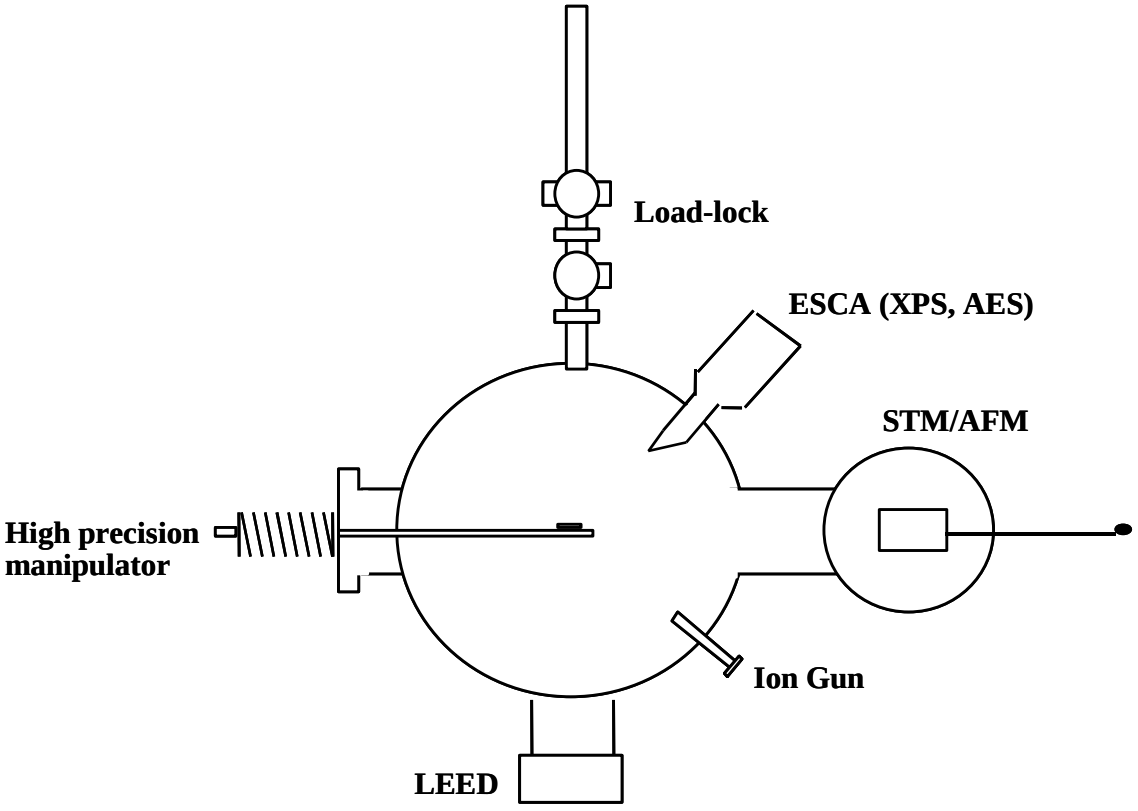

Figure 4.1. Schematic of the top view of the Ultra-High Vacuum system.

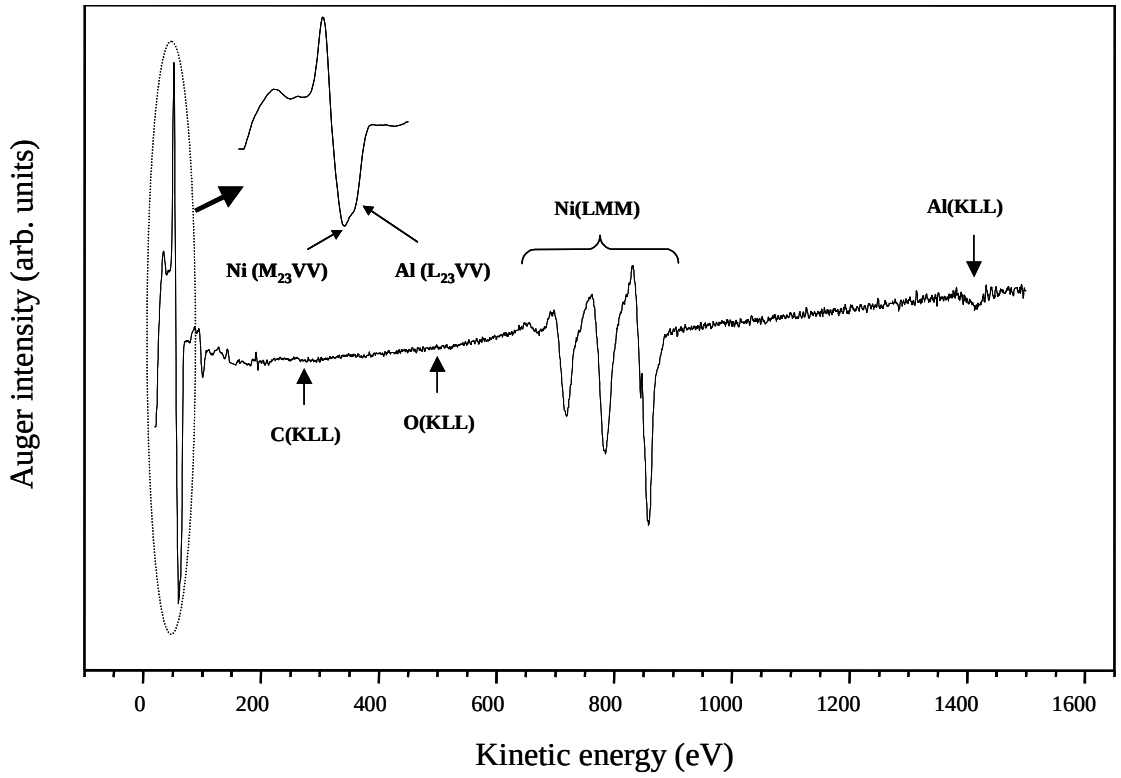

Figure 4.2. Auger electron spectrum of a Ni_3Al sample after sputter-annealing cycles.

4.2. EXPERIMENTAL METHODS

The experiments were carried out in an Omicron UHV-STM system (Fig. 4.1) equipped with Low Energy Electron Diffraction (LEED) optics, a cylindrical mirror analyzer (CMA) for Auger Electron Spectroscopy (AES), and a sputter ion gun. The system was evacuated with a turbomolecular pump, an ion pump, and a titanium sublimation pump. When an ultra high vacuum ($< 1 \times 10^{-9}$ Torr) was achieved, the gate valve between the system and the turbomolecular pump was closed. Ion pump was then

used solely to maintain the chamber vacuum. Base pressure of 5×10^{-11} Torr can be achieved after system bake-out. Typical working pressures range from 5×10^{-11} Torr to 3 $\times 10^{-10}$ Torr. When the experiment was not in session, the titanium sublimation pump was turned on occasionally to help ion pump bring down the chamber pressure to the above working pressure range.

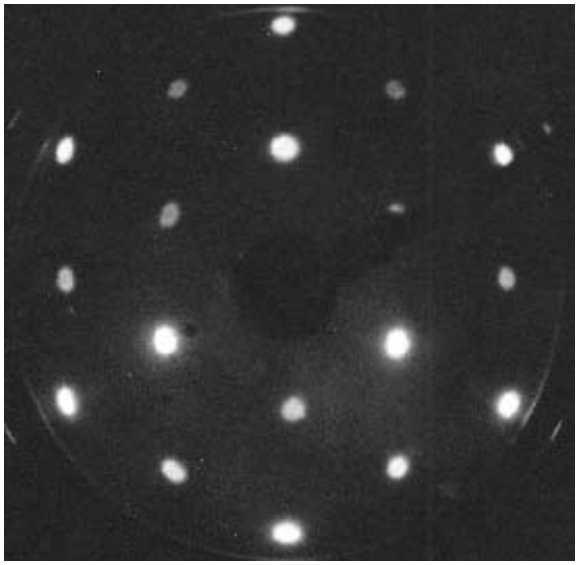

Figure 4.3. LEED pattern of a Ni_3Al sample after sputter-annealing cycles. The pattern corresponds to a 2×2 reconstructed $Ni_3Al(111)$ surface.

The sample was a $Ni_3Al(111)$ single crystal disc with a diameter of 10 mm and a thickness of 0.5 mm. The sample was introduced from air into the UHV system via the load-lock chamber by means of a magnetic linear feedthrough. The load-lock chamber was separately pumped by a turbomolecular pump. Sample transfer to STM stage was accomplished with the use of a wobble-stick. A high precision *x-y-z-*θ manipulator allowed optimal sample positioning within the main chamber.

The cleanness and ordering of the sample were monitored by AES and LEED. After several sputtering-annealing cycles, AES gave no carbon or oxygen signal (Fig. 4.2). A sharp (2×2) LEED pattern (Fig. 4.3) was also observed, indicative of a clean $Ni_3Al(111)$ surface.

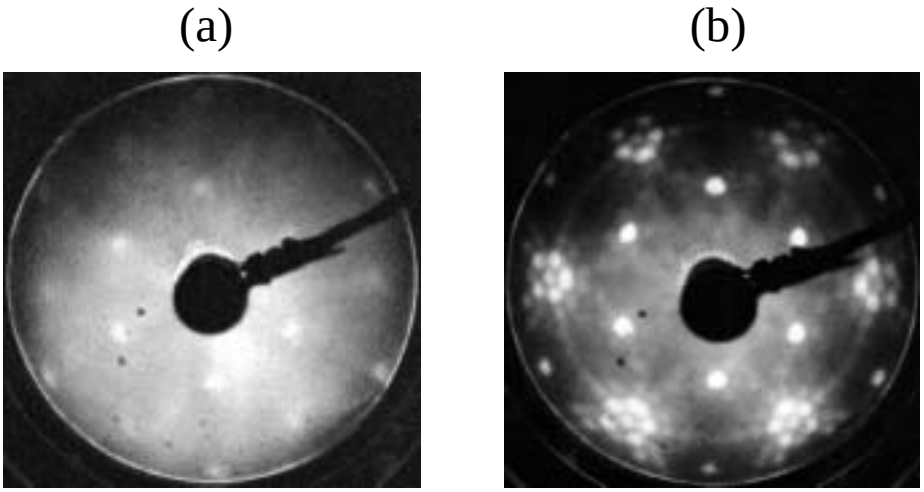

Figure 4.4. LEED pattern after the clean Ni_3Al sample was dosed with 1800 Langmuir of oxygen (a) and then annealed to 1100 K for 2 hours (b).

The Al_2O_3 film was grown by dosing the clean $Ni_3Al(111)$ with 1800 Langmuir O_2 in UHV chamber at room temperature. The sample was then annealed to 1100 K for 2 hours in UHV. LEED pattern change of the sample is shown in Fig. 4.4. Previous experimental (26, 36) and theoretical studies (43) have shown that a well ordered γ'-Al_2O_3 film (~7 Å thick) can be obtained after conducting the above treatment. The overall characteristics of the oxidized and annealed $Ni_3Al(111)$ surface revealed by LEED, AES, and STM were consistent with previously reported results (26). Large-area

STM images showed that the surface was flat on a nanoscopic scale, with steps 2-5 Å high and terraces 10-400 nm wide.

Two methods were used to expose the ordered Al_2O_3 films to high electric fields:

(1) Constant current mode. After imaging a large area of the surface, the tip was directed to a certain point within this area. With the feedback current set at 1 nA, the bias was increased to a desired value in 200 steps. Each step required about 200 μs. At each bias voltage, the corresponding tip/sample displacement (Z) was recorded on a Z vs. V spectrum. A complete Z/V spectrum requires ~0.04 seconds. Each time a Z/V spectrum was taken, the thin oxide film experienced a high field stressing.

(2) Constant height mode. After imaging a large area of the surface, the tip was directed to a certain point within this area. With the feedback loop turned off (tip-sample displacement kept constant), the bias was increased to a desired value in 200 steps. Each step required about 200 μs. At each bias voltage, the corresponding tunneling current was recorded on an I vs. V spectrum. A complete I/V spectrum requires ~0.04 seconds. Each time a Z/V spectrum was taken, the thin oxide film experienced a high field stressing.

For both methods, the field strength (E) at a certain bias voltage (V) was estimated using:

$$E = V / (t_{ox} + d_0 + d) \qquad (4.1)$$

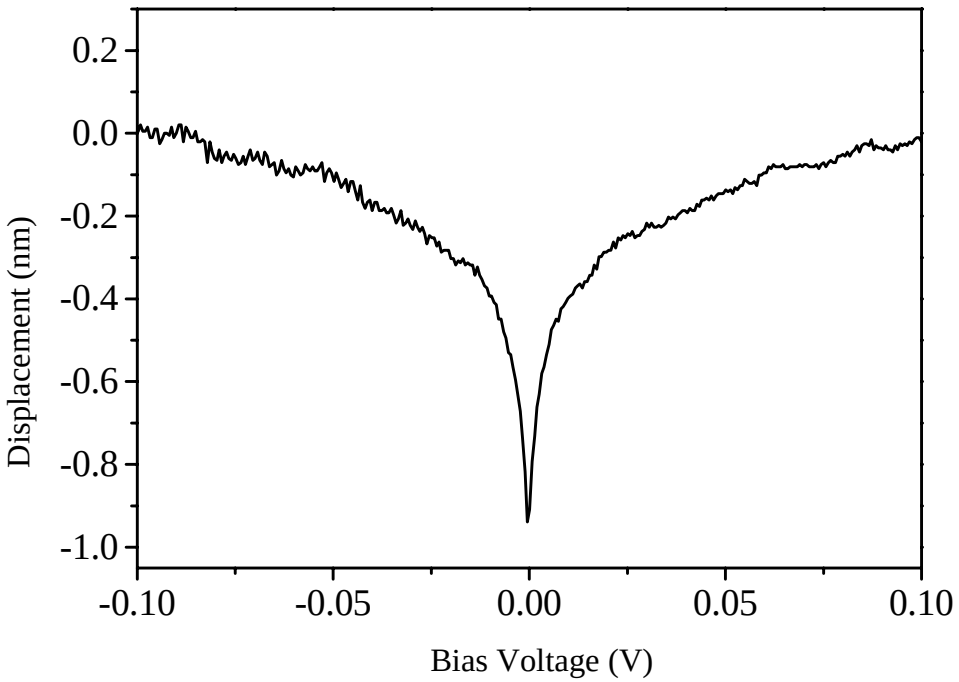

Figure 4.5. Tip-sample displacement vs. bias voltage curve (1 nA feedback current). Tip-sample distance was reduced by ~1nm when bias decreased from 0.1 to 0 V, indicating initial separation to be ~1 nm.

where t_{ox} is the thickness of the oxide film (0.7 nm), d_0 is the initial tip-sample separation (i.e. the tip-oxide distance at 0.1 V bias and 1 nA feedback current), and d is the recorded displacement of the tip from d_0 upon increasing the bias voltage to a specified value (for constant height method d is always 0). The value of d_0 was estimated to be ~1 nm based on the fact that the tip approached the sample by about ~1 nm when the bias was reduced from the initial tunneling bias voltage of 0.1V to 0 V (where minimum tip-sample separation is expected, see Fig. 4.5). After each high field stressing, the surface region was imaged under normal tunneling conditions, i.e. 0.1 V bias voltage and 1 nA constant feedback current.

STM imaging was performed in the Omicron UHV-STM system described previously. STM tips were prepared by electrochemically etching a polycrystalline tungsten wire. Constant current STM topographies were recorded at room temperature by applying a positive bias voltage to the sample (0.1 – 2 V) while maintaining the feedback current at 1 nA. Application of a positive gap voltage denotes the tunneling of electrons from the occupied states of the tip to the unoccupied states of the sample. STM atomic resolution images were calibrated with a HOPG (highly oriented pyrolytic graphite) sample.

4.3. RESULTS

4.3.1. STM Imaging of Ultrathin Al_2O_3 Films and $Al_2O_3/Ni_3Al(111)$ Interface

Bertrams and co-workers have demonstrated that for a thin oxide film grown on a

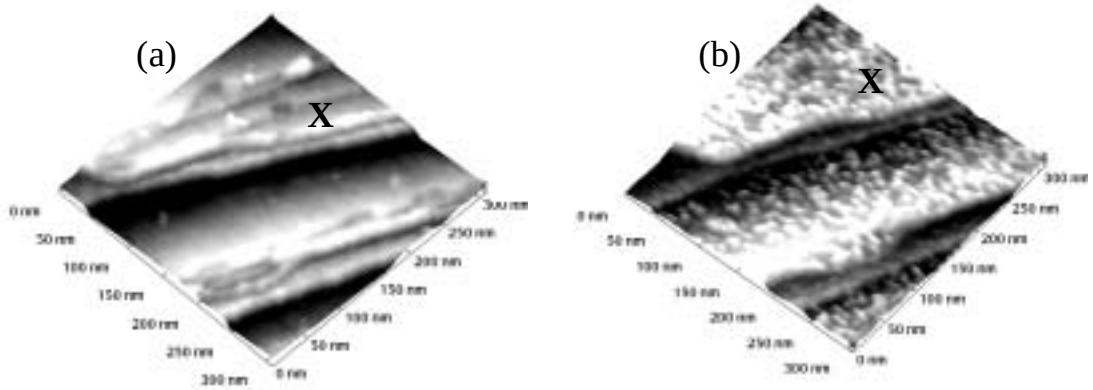

Figure 4.6. Large area STM images of well-ordered Al_2O_3 supported on $Ni_3Al(111)$ acquired at constant current of 1 nA and bias voltages of (a) 0.1 V and (b) 2.0 V.

metallic substrate, STM images differ significantly with bias voltage (42). Low bias images involve only states located close in energy to the metal substrate Fermi level, whereas images at higher voltages will involve tunneling between oxide valence or conduction band states located further from the Fermi surface. Similar results have been obtained in our STM study of the 7 Å γ'-Al_2O_3/Ni_3Al(111) system. Fig. 4.6 displays STM images of the same region (300 nm x 300 nm) of the ultrathin aluminum oxide film acquired at different gap voltages (The images were independent of gap voltage polarity). Figure 4.6a, which was acquired at 0.1 V, shows relatively smooth terraces with average corrugations of 0.6 ± 0.2 Å. The image obtained at 2.0 V (Fig 4.6b), however, contains elevated features that are 100 – 150 Å wide and 2 – 6 Å high.

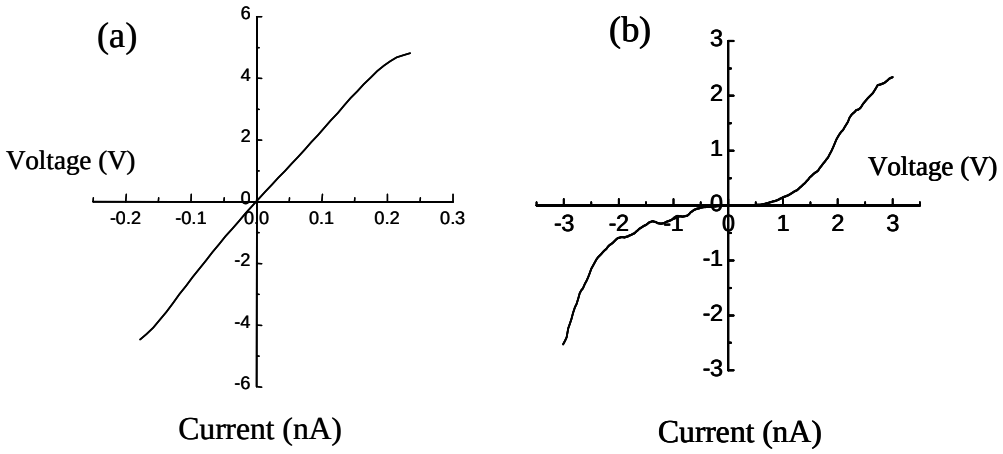

Figure 4.7. I/V curves taken during STM scanning at 1 nA feedback current and (a) 0.1 V and (b) 2 V sample bias.

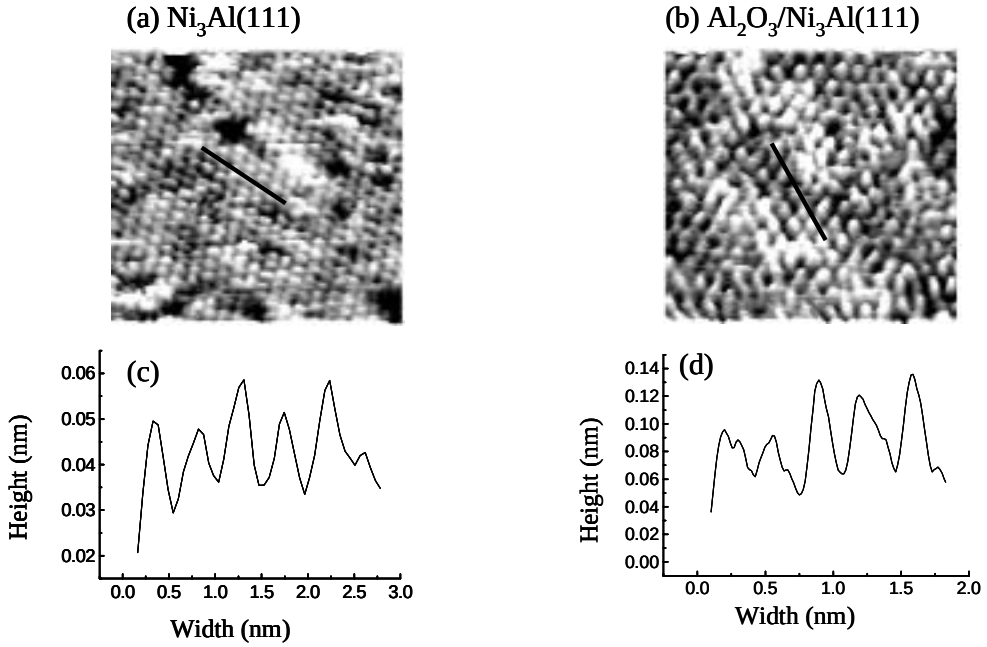

Figure 4.8. Atomically resolved STM images of (a) clean $Ni_3Al(111)$ (10 nm x 10 nm) and (b) Al(111) at the $Al_2O_3/Ni_3Al(111)$ (5 nm x 5 nm) interface obtained at constant current of 1 nA and gap voltages of 0.1 V, and their corresponding line profiles (c and d, respectively).

The I/V characteristics of the sample were also acquired while imaging the surface at 0.1 V (Fig. 4.7a) and 2.0 V (Fig. 4.7b) gap voltages. In this mode, the bias voltage for imaging significantly influences the I/V data obtained. The ohmic behavior shown in Fig. 4.7a is consistent with a metallic behavior. On the other hand, the band gap of ~1.5 eV (Fig. 4.7b) is indicative of an insulating behavior consistent with the presence of an oxide overlayer. This band gap is, however, narrower than that of the bulk Al_2O_3 (8.7 eV). Narrowing of the band gap for ultrathin films of Al_2O_3 has been explained by Density Functional Theory calculations as due to the overlap of wavefunctions of the oxide and

the metal substrate (43). The difference in the I/V characteristics observed for the STM images acquired at 0.1 V (Fig. 4.7a) and 2.0 V (Fig. 4.7b) gap voltages demonstrates further that the image obtained at low and high gap voltages correspond to the Al_2O_3/Ni_3Al (111) interface and the Al_2O_3 overlayer, respectively.

Because tunneling at 2.0 V takes place between the tip and the oxide electronic states, we attribute the elevated features shown in Fig. 4.6b to the Al_2O_3 film surface. In the region marked with **X**, the step structures with step heights (3.0 to 5.0 Å) that are nearly identical with the step heights obtained for the clean Ni_3Al (111) (26) are visible in Fig. 4.6a but not in Fig. 4.6b, indicating that the Ni_3Al (111) substrate in this region (marked X) is covered completely by the oxide overlayer. The height differential between the lowest and the highest terraces in this region is around 6 Å, which is very close to the thickness of the oxide at 7 Å obtained from Auger measurements.

Figure 4.8 displays the atomically resolved STM images of the clean Ni3Al (111) (Fig. 4.8a) and Al_2O_3/Ni_3Al (111) (Fig. 4.8b) obtained at low gap voltage of 0.1 V and constant current of 1nA. The 10 nm $\times$ 10 nm image shown in Fig. 4.8a reveals a hexagonal array, with a corrugation amplitude of 0.3 ± 0.1 Å, and an average inter-atomic distance of 4.9 ± 0.3 Å. Ni_3Al crystallizes in a face-centered cubic lattice with a bulk unit cell length of 3.56 Å, which leads to a lattice constant of 5.03 Å for the Ni_3Al (111)(2×2) surface. This lattice length corresponds to the distance between two neighboring aluminum atoms. Therefore, the inter-atomic distance measured in the atomically resolved image of the clean, well-annealed Ni_3Al (111) sample is in excellent agreement

with the distance between two neighboring aluminum atoms in the Ni_3Al (111)(2×2) unit cell, as previously reported (26, 36).

In Fig.4.8b, a constant current (1 nA) STM image (5 nm × 5 nm) at atomic resolution of the oxidized Ni_3Al (111) at a low gap voltage of 0.1 V also reveals hexagonal arrays of corrugations. The inter-atomic distance calculated from this image, however, is only 3.1 ± 0.2 Å. The protrusions in this image were tentatively assigned to oxygen ions in a previous report (26). The data shown in Figs. 4.6 and 4.7, however, have demonstrated that STM images obtained at low gap voltages correspond to metallic states close to the substrate Fermi level. Therefore, the image shown in Fig. 4.8b is assigned to the Ni_3Al/Al_2O_3 interface and not to the Al_2O_3 film. The hexagonal protrusions in this figure, however, cannot be assigned to the Ni_3Al (111) substrate itself because the atomic

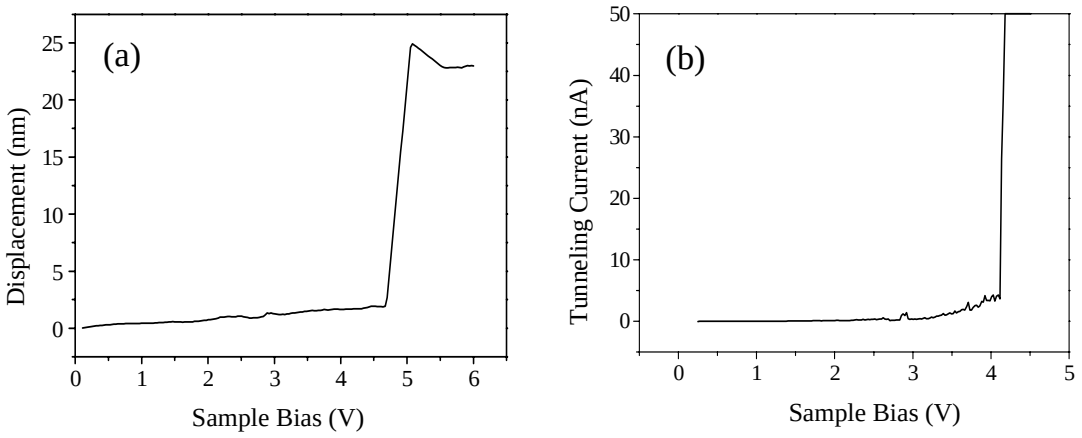

Figure 4.9. Dielectric breakdown of a 7Å γ'-Al_2O_3 film: (a) Z/V spectrum in constant current mode (feedback current 1 nA); (b) I/V spectrum in constant height mode (~3.2 nm). Sudden increase of the tip-sample displacement in (a) or tunneling current in (b) indicates the loss of the insulating nature of the oxide film.

distance of 3.1 ± 0.2 Å calculated from Fig. 4.8b is not consistent with the lattice constant of the Ni_3Al (111) surface. Because the atomic distance calculated from the image acquired at 0.1 V gap voltage is in very good agreement with Al-Al lattice spacing (2.9 Å) in the Al (111) surface, we assign the hexagonal arrays of protrusions in Fig. 4.8b to an Al(111) layer at the Ni_3Al/Al_2O_3 interface. The presence of an Al(111) interfacial layer is consistent with the results obtained from AES measurements reported previously (26). An increase of 60% in the $Al_{(1396)}/Ni_{(848)}$ Auger atomic ratio and the appearance of the metallic $Al_{(68)}$ peak in the Auger surface-sensitive region support the idea that an interfacial layer is formed upon annealing the oxide to ~1100 K.

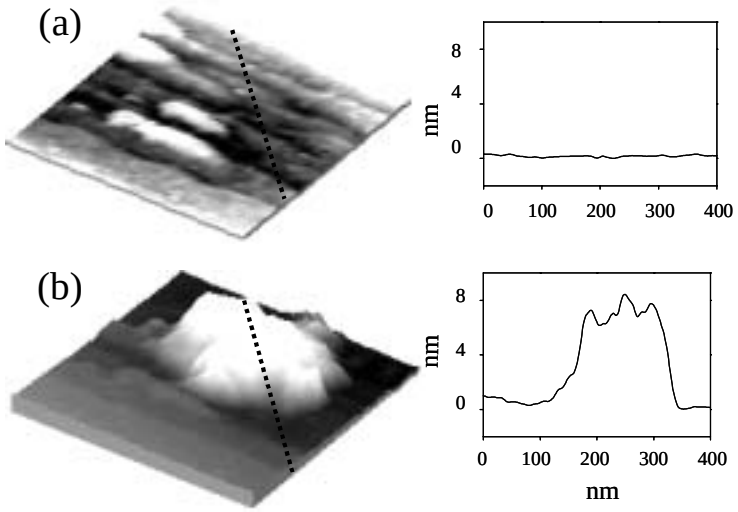

Figure 4.10. 400 nm × 400 nm STM images showing a region (a) before and (b) after dielectric breakdown. Line profiles of the affected region are displayed beside the images. (Bias voltage: 0.1 V; Feedback current: 1 nA)

4.3.2. STM Induced Dielectric Breakdown of Ultrathin Al_2O_3 Films

By increasing the bias between the sample and the STM tip, dielectric breakdown of the ultrathin γ'-Al_2O_3 film can be induced in either constant current mode or constant height mode as described in section 4.2.

Fig. 4.9a shows a typical Z/V spectrum during dielectric breakdown using constant current method. The breakdown is marked by an abrupt increment of the tip-sample displacement. Fig. 4.9b, on the other side, shows a typical I/V spectrum during dielectric breakdown using constant height method. Here the breakdown is marked by a sudden increment of the tunneling current. In either case, subsequent STM constant current imaging showed a new feature at the breakdown site (Fig. 4.10). Such features were typically 8-25 nm in height and 50-250 nm in diameter as given by constant current STM

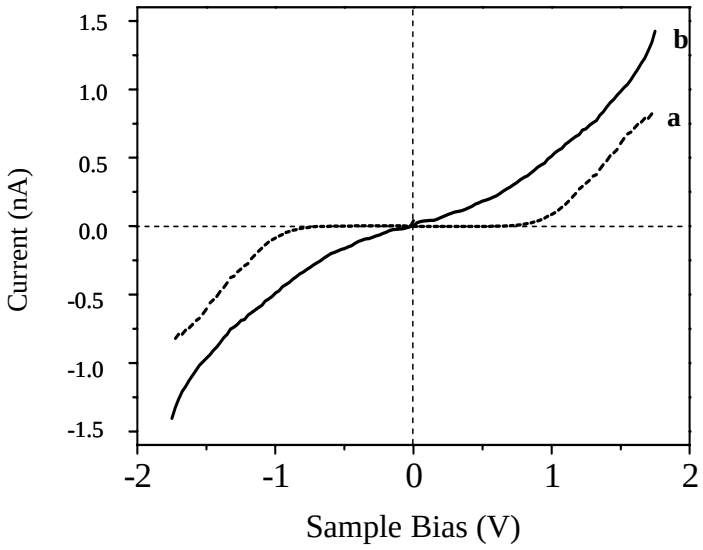

Figure 4.11. I/V spectra for (a) the vicinal oxide film and (b) the same region after dielectric breakdown.

images. Imaging at constant height mode (~1 nm) under high scan speed (up to 5000nm/s) and significantly slowed down feedback, however, did not result in tip crash or topography change of the breakdown site. This indicates that there was no physical contact between the tip and the apparent high feature at the breakdown site during constant height imaging.

Similar results have been reported in a recent study of dielectric breakdown of a diamond film on silicon (44), where much larger breakdown features were observed by STM than by AFM. We conclude, therefore, that the elevated feature in constant current images (Fig.4.10) is not due to mass transport but mainly due to the loss of the insulating characteristics of the oxide film. This conclusion is further corroborated by I/V spectroscopy of the region before and after high field stressing (Fig.4.11). The I/V curves

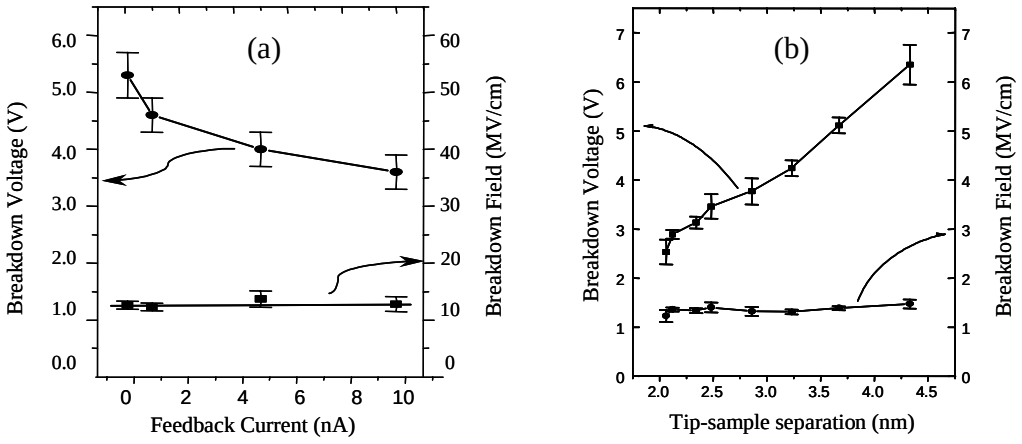

Figure 4.12. Dielectric breakdown voltages and fields obtained using (a) constant current mode and (b) constant height mode. Breakdown voltage changes with the feedback current, yet the breakdown field remains constant.

were obtained by grid mode scanning tunneling spectroscopy (STS) with 1.5 V bias and 1 nA feedback current (feedback loop was off during acquisition of I/V spectroscopy). As shown in Fig.4.11, the vicinal oxide displayed a band gap of about 1.5 eV, while the same region after breakdown displayed an ohmic-like behavior.

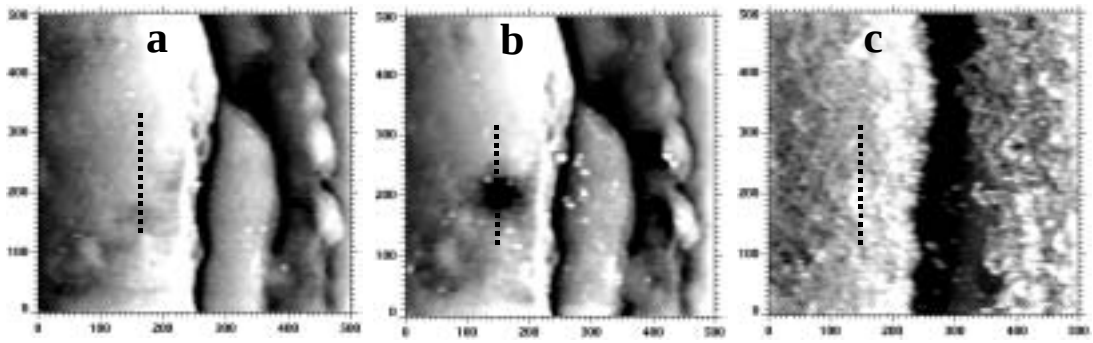

Figure 4.13. STM images showing the effect of lower field stressing (0.1-4 V pulsing with feedback current set at 1 nA during voltage ramp): (a) before stressing (bias 0.1 V); (b) after 30 pulses (bias 0.1 V); (c) after 30 pulses (bias 2 V). Feedback current 1 nA.

.

A series of breakdown Z/V curves were obtained for various regions of the thin oxide film. The average breakdown threshold voltage was 4.6 ± 0.3 V when the feedback current was kept at 1 nA (d_0 1.0 nm). Using equation (4.1), the critical breakdown field was calculated to be 12.3 ± 1.0 MV/cm. The breakdown voltage was found to depend on the feedback current during high field pulsing. Lower breakdown voltage was observed when using higher feedback current (i.e. smaller tip-sample separation), and vice versa. The breakdown field, however, was the same regardless of the feedback current

(Fig.4.12a). Similarly, in constant height mode, the breakdown voltage increases with the tip to sample separation, but the breakdown field remains constant (Fig.4.12b). The critical breakdown field of 12.3 MV/cm is in good agreement with extrapolated values from capacitance measurements on thicker Al_2O_3 oxides (45).

4.3.3. STM Induced Void Formation at the Metal-Oxide Interface

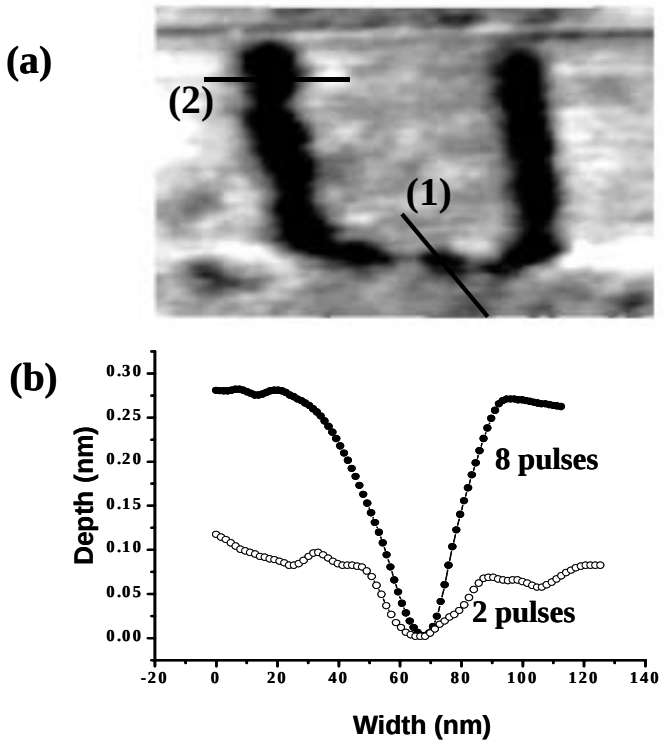

Figure 4.14. (a) STM constant current (0.1 nA, 0.1 V bias) images of pits formed into a "U" with varied numbers of pulses from 0.1 to 3.5 V (sample positive). (b) Cross sectional line profile of different regions of the "U" after application of 2 and 8 pulses, respectively.

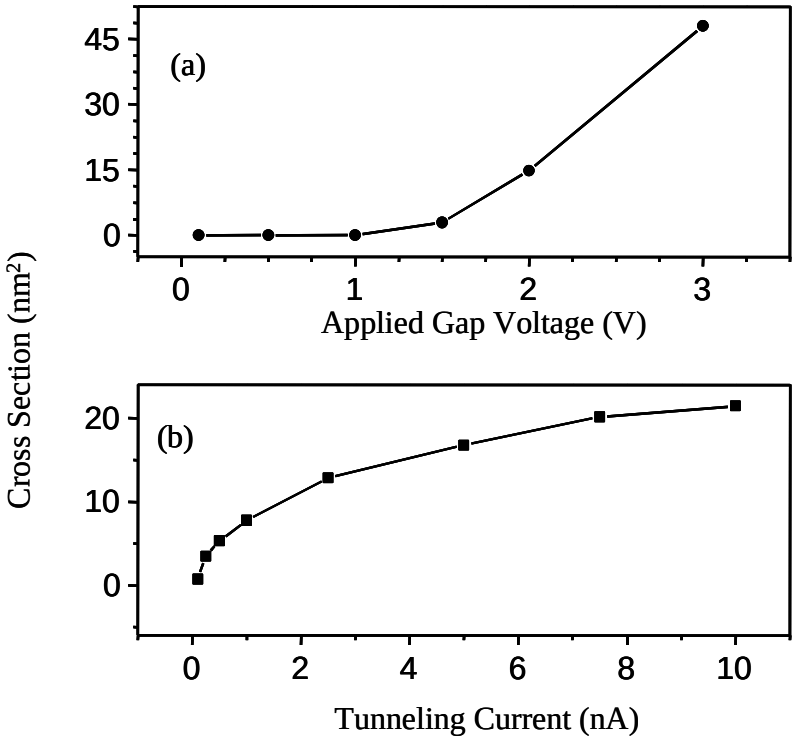

Figure 4.15. (a) Void cross sectional area, after 300 sec exposure, vs. the electric field strength. (b) Void cross sectional area, after 300 sec exposure, vs. tunneling current.

Surprising results were obtained after stressing a surface region with electric fields lower than the threshold breakdown field (12.3 MV/cm). In Fig.4.13a, the marked region prior to stressing was relatively flat as indicated by the line profile. Lower field stressing was carried out under identical conditions as described above except that the bias voltage pulse was set below the breakdown voltage. Fig. 4.13b shows the effect after pulsing the region (marked by a dotted line) from 0.1 V to 4.0 V for 30 times (constant current mode with feedback current of 1 nA). A pit that is about 0.8 nm deep and 150 nm wide was observed in the subsequent STM image recorded at 0.1 V bias and 1 nA feedback current. Using 2 V bias, however, an image was obtained in which the pit was no longer visible

(Fig. 4.13c). As previously observed (41, 42, 44), STM images obtained for thin oxides at low bias involve electrons tunneling between the tip and the metal substrate. At relatively higher bias, however, tunneling takes place between the tip and the electronic states of the oxide. The appearance of a depression only in STM images acquired at low bias indicates a void at the oxide/metal interface.

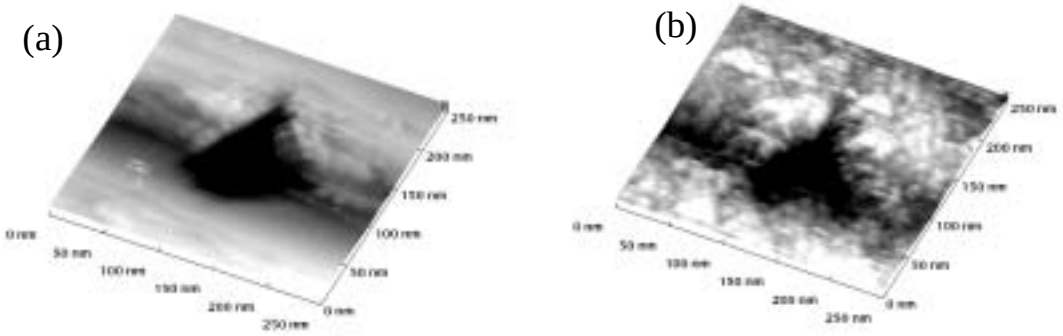

Figure 4.16. STM constant current images showing a large void and collapse of the oxide overlayer. (a) Constant current image (1nA, 0.1V bias) showing the void (30 Å deep and 500 Å wide) present at the oxide/metal interface; (b) Constant current image (1nA, 2.0 V bias) of the same region showing a gap (presumed collapse) in the oxide overlayer.

.

Voids grow further into the metal by increasing the lower field stressing time. Fig. 4.14a displays voids created by voltage pulsing to 3.5 V at various locations at the surface (feedback current 1 nA). The voids at positions 1 and 2 were produced by 2 and 8 pulses, respectively (Fig. 4.14a). It is evident from the line profiles in Fig. 4.14b that the void in position 2 is ~2 Å deeper and ~350 Å wider across the rim than the void in

position 1. Voids can also be created by holding the bias voltage and tunneling current between the sample and the STM tip constant for a specified time at a given location on the oxide surface.

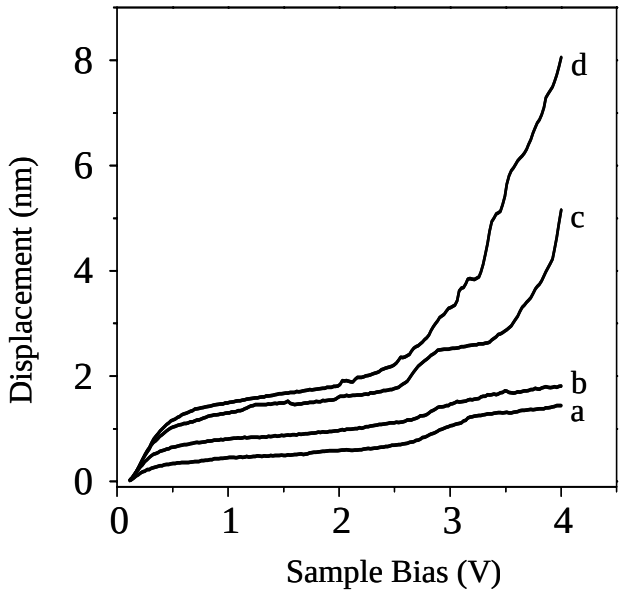

Figure 4.17. Z/V spectrum change during lower field stressing (0.1-4 V pulsing): (a) the 1st pulse, (b) the 5th pulse, (c) the 15th pulse, and (d) the 30th pulse. (feedback current 1 nA)

The dependence of void growth rate on the electric field was characterized by measuring the cross sectional area of the void after exposing the surface to a specified bias voltage at 300 seconds. Results are shown in Fig. 4.15a for void cross sectional area vs. electric field. Under these experimental conditions, the electric field varies approximately linearly with the applied gap voltage. The data in Fig. 4.15a indicate that the rate of void growth increases rapidly above ~5 MV/cm. The threshold for void growth suggested by the data in Fig. 4.15a may be more apparent than real, since voids

can be created even at field strengths below 4 MV/cm provided the surface is exposed to a field for a very long time (≥ 2700 sec). Experiments at constant voltage and varying feedback current indicate that void growth rate also increases with tunneling current at a given applied voltage (Fig 4.15b), although the growth rate apparently approaches an asymptotic value at higher currents.

Upon reaching a certain size, the void may induce a failure of the oxide overlayer. This is shown in Fig. 4.16. The constant current image of the metal substrate (Fig. 4.16a) shows the presence of a void ~ 30 Å in depth and 500 Å wide. Subsequent imaging at 2.0 V bias (Fig. 4.16b) also shows a gap in the oxide overlayer. This result indicates that continued exposure to high bias voltage causes the void to grow wider and deeper into the metal, eventually causing the (assumed) collapse of the oxide overlayer. This behavior has also been observed in an aggressive aqueous environment where the oxide film suffered a local collapse once the void grew to a critical size (46), larger than that observed here because of a thicker oxide layer.

Lower field stressing has significant effect on the Z/V spectrum of the affected region. As shown in Fig. 4.17, the tip-sample displacement (Z) keeps increasing with number of pulses, especially for voltages higher than 2.7 V. This indicates a decrease in the local effective barrier height. In order to maintain a constant feedback current, the tip had to move farther away from the surface.

Another effect of the relatively low field stressing is the decrease of field strength required for dielectric breakdown of the thin Al_2O_3 film. Shown in Fig.4.18 are a series of constant current STM images (bias 0.1 V, feedback current 1 nA) taken during

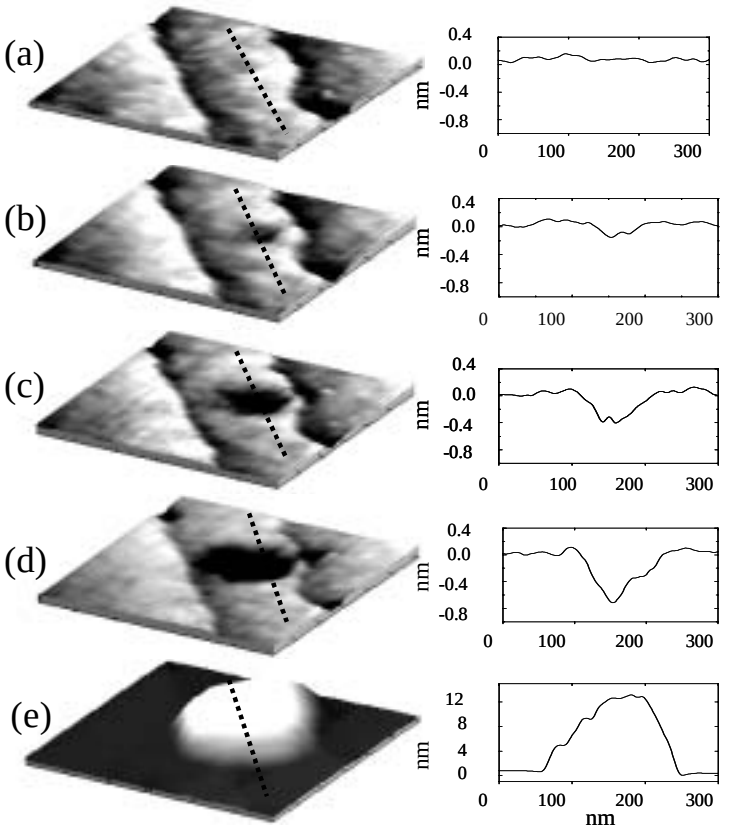

Figure 4.18. 400 nm × 400 nm STM images (0.1 V bias, 1 nA feedback current) showing 0.1 to 4 V pulsing effect: (a) initial surface, (b) after 5 pulses, (c) after 20 pulses, (d) after 40 pulses, (e) after 45 pulses. Beside the images are the line profiles of the affected site. Interfacial void formation resulted in a decrease of breakdown field for the ultra-thin Al_2O_3 film.

continuous 0.1 to 4 V stressing. The void at the interface grew larger and deeper with the number of pulses (Figs. 4.18a-d). At the 45th pulse, the dielectric breakdown of the thin oxide film occurred at 3.8 V as indicated by Z/V spectrum (not shown). Subsequent imaging showed a typical breakdown feature (Fig.4.18e). The breakdown field calculated using equation (4.1) is 7.1 MV/cm. Such field strength, however, could not cause dielectric breakdown anywhere other than at the pitting site.

The data in Figs. 4.16 and 4.18 indicate that void size increases with the number of pulses applied until either a collapse or a dielectric breakdown of the oxide film occurs. Other than voltage pulsing, continuous exposure to bias voltages up to 4.0 V (feedback current 1 nA, estimated field 5-8 MV/cm) for varied length of time yield similar results. For bias greater than 3 V, continuous exposure would result in dielectric breakdown within seconds. Using lower bias, the exposure time required for dielectric breakdown increases substantially to several minutes. For bias voltage less than 2.7 V, most times oxide collapse was observed to occur rather than dielectric breakdown.

4.4. DISCUSSION

The results obtained in this study demonstrate that a threshold field of 12.3 ± 1.0 MV/cm is required to induced dielectric breakdown of the 7Å γ'-Al_2O_3 film grown on $Ni_3Al(111)$. Exposure to lower electric fields, however, results in either oxide film collapse or time dependent dielectric breakdown (TDDB). During the “incubation” time, interfacial voids are formed. The growth of these voids leads to a decrease of the dielectric strength of the thin oxide films.

All the results reported in this paper are based on experiments in which the sample was positively biased relative to the tip. Although systematic study on effects of fields in the opposite direction is yet to be carried out, our preliminary results show that there is no significant polarity effect. Electric fields in either direction can induce interfacial pitting, which leads to time dependent dielectric breakdown of ultra-thin Al_2O_3 films. Two important issues raised by these results are (a) the mechanism for interfacial void

formation and growth, and (b) the relationship between void formation/growth and the decrease in the oxide dielectric breakdown strength.

The apparent lack of a discernable voltage threshold suggests the void formation process is not stimulated by a specific electronic excitation. In addition, bias polarity-independence and current-dependence argue against field-assisted diffusion across the interface. Field induced vacancy diffusion from within the metal can be ruled out because the applied field does not extend far into the conducting substrate. The migration of vacancies from within the oxide is similarly improbable because the oxide film is of high quality and the data clearly demonstrate void growth into the metal.

A possible explanation is localized heating due to inelastic electron-phonon scattering, enabling the system to overcome a kinetic barrier. This mechanism would show a current and field dependence of void growth rate, consistent with the data in Fig. 4.15. A similar mechanism was proposed for Si-H bond-breaking at Si surfaces (47), while electronically stimulated processes within SiO_2 films have a discernable threshold (48).

To help define a mechanism, we turn to *ab initio* theory. This was done by D.R. Jennison at Sandia National Laboratories using DFT (49, 50) and slab calculations. Because energetics are compared, he used the generalized gradient approximation (GGA) known as "PW91" (51), as implemented in the Vienna *Ab-Initio* Simulations Package (VASP) (52-54). Ultrasoft Vanderbilt pseudopotentials (55, 56) accurately removed the core electrons with a plane wave cutoff of only 270 eV. Geometric relaxation used a damped molecular dynamics algorithm until all forces were less than 0.05 eV/Å. The slab

had five layers of aluminum metal, with the bottom two frozen at the bulk GGA lattice constant of 4.035 Å. Because of long-range electrostatic interactions, the periodic vacuum gap due to the plane-wave basis always exceeded 18 Å.

As a model for the real film on $Ni_3Al(111)$ (which cannot be directly studied because of lattice-mismatch relief by domain rotation (36, 57)), computations were performed with three and four O-layer commensurate alumina systems on Al(111), all having chemisorbed oxygen at the interface. This interface, first proposed for ultrathin alumina films on metals made by high temperature annealing in oxygen rich conditions (43), receives further support from our angle resolved XPS results together with those of others (58): two types of oxygen (chemisorbed and oxidic) were found to be present.

Above the layer of chemisorbed oxygen, two different phases of alumina were explored. The first is motivated by the recent observation of θ-alumina on NiAl(100) by A. Stierle, et al. (59). This structure, found using X-ray scattering, supported a computational result (43) predicting that the normal preference for octahedral site Al-ions is reversed at the interface; thus in this extreme model, all Al ions occupy tetrahedral sites. In the second model, the recently determined structure for the κ-phase (60) was used, which has ¼ tetrahedral and ¾ octahedral site Al-ions. This structure is similar to a recent DFT structure for the second O-layer in ~ 5 Å films on close-packed surfaces (61), and is a more realistic model for the so-called (36, 57) γ′ -films. The qualitative results were found to be *independent* of the details of oxide film structure.

In all cases it is found that the REDOX reaction (Fig. 4.19) is preferred energetically. In fact, for Al(111) with this interface, *the entire first layer of Al* prefers to

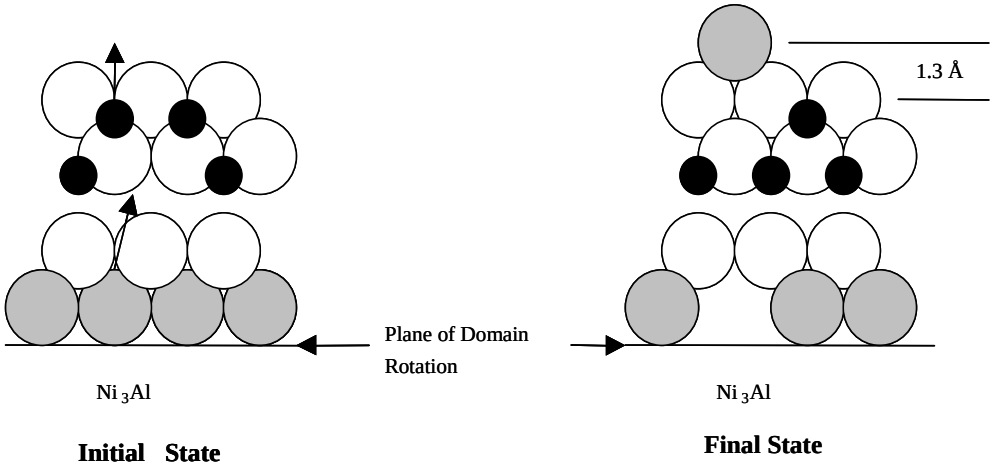

Figure 4.19. Schematic diagram indicating the proposed REDOX mechanism. Atoms are oxygen in white, Al metal in gray, Al ions in black. After the first atom goes, it is easier for the next because of reduced coordination. The reduced Al adatom height is shown .

be taken up into the oxide, even at the expense of becoming non-stoichiometric, with extra Al atoms reduced to adsorbed Al (Fig. 4.19). This movement is preferred by 0.15 (0.21) eV per Al atom in the tetrahedral (κ-phase) film. While these results agree with independent experimental observations of the alumina/aluminum system (58), which show a preference for the incorporation of chemisorbed oxygen into aluminum oxide islands, the results cannot be directly applied to the present case: starting with a perfect interface, the first REDOX reaction breaks 6 Al-Al and 3 Al-Ni bonds, vs. 9 Al-Al in the model systems. Given the melting temperatures of Al metal (660 °C) and Ni_3Al (1390 °C) vs. pure Ni (1455 C), Ni-Al bonds are much stronger than Al-Al, thus reducing the exothermicity. However, these results are consistent with a kinetically limited REDOX mechanism, and one reason for the above energetics is the strong binding of Al adatoms to alumina (62).

Overall, the above results suggest nanovoid formation in the presence of electric field and induced current is a likely critical step in the corrosive pitting of aluminum (and possibly of other metals) and might significantly affect the durability of alumina-based tunneling junctions. Remaining to be addressed are the fundamental mechanisms of total mass transport (both interfacially and *within* the void) and whether only Al or both Al and Ni move across the interface. In addition, it is not known how formation and growth are related to the cohesive energy of the substrate material. However, with respect to the existing experimental and theoretical results, the following conjectures are made:

(1) *The presence of nanovoids at the alumina/aluminum (or aluminum alloy) interface is ubiquitous.* Voids are produced by non-uniform electric fields and currents in the passivating oxide layer; such occur in an electrochemical environment and are supported by the resulting oxide point defects(45) (25). The induced fields are similar in magnitude to those in the present study (25), while the metal cohesive energy is lower. This conjecture is also consistent with recent positron studies of alumina/aluminum interfaces (63) and with new experimental results indicating that Cl^- anions do not penetrate existing oxide films under open circuit conditions, even though pitting can occur under such conditions (64, 65).

(2) *The transition from nanovoids to microscopic corrosion pits is induced by the collapse of, and/or the presence of microcracks in, the oxide, when void growth causes local mechanical failure from factors such as strain.* Cracks allow the transport of anionic species into the void, which grow into pits because metal is etched into soluble

compounds. Local fluid flow conditions, vs. the formation of insoluble scales and/or new oxide films at the pit surface, determine the balance between growth and passivation.

Oepts *et al.* (4, 5) reported a time-dependent breakdown of alumina-based ferromagnetic tunnel junctions upon the application of a field of 4-5 MV/cm. Such a result is consistent with the void initiation and growth, which leads to reduced dielectric breakdown strength. The reason for the decrease in apparent dielectric strength of the oxide film with time of exposure to electric fields below the breakdown threshold is not apparent from these data. One possible explanation is a local enhancement of the electric field in the vicinity of the pit due to geometric factors. The results presented in Fig. 4.17, however, suggest that the tunneling resistance of the oxide itself decreases with time of exposure to the field. This in turn might be due to defects within the oxide induced either by tunneling electrons or by the transport of metal atoms from the substrate into the oxide film.

Nevertheless, more details of the interfacial void formation and dielectric breakdown of thin Al_2O_3 films supported on metals remain to be studied in the future. Such details include the interfacial transport mechanism, chemical reactions during dielectric breakdown, effects of impurities and oxide microstructure (crystalline vs. amorphous), etc. A complete understanding of these processes is essential for the development of tunneling based electronic devices, and the engineering of materials that are resistant to localized pitting corrosion.

4.5. CONCLUSIONS

Scanning Tunneling Microscopy and Scanning Tunneling Spectroscopy have been used to study the high electric field behavior of ultra-thin γ'-Al_2O_3 films grown on $Ni_3Al(111)$. The results indicate:

1) Dielectric strength of the oxide film is 12.3 ± 1.0 MV/cm, which is in good agreement with the results of capacitance measurements on thicker films (45) extrapolated to a thickness of 7 Å.
2) Lower field Stressing of the thin oxide film creates pits at the oxide/substrate interface. The pits grow larger and deeper with time of exposure to electric fields.
3) Dielectric breakdown threshold of the thin oxide film in the "pitting" region is lower than that of the unstressed region.
4) Extended lower field exposure results in either collapse or dielectric breakdown of the thin Al_2O_3 films.

4.6. CHAPTER REFERENCES

(1) Baumer, M.; Freund, H.-J. *Prog. Surf. Sci.* **1999,** *61*, 127.

(2) Magtoto, N. P.; Niu, C.; Anzaldua, M.; Kelber, J. A.; Jennison, D. R. *Surf. Sci.* **2001,** *472*, L157.

(3) Magtoto, N. P.; Niu, C.; Ekstrom, B.; Addepalli, S.; Kelber, J. A. *Appl. phys. Lett.* **2000,** *77*, 2228.

(4) Oepts, W.; Verhagen, H. J.; Jonge, W. J. M. d.; Coehoorn, R. *Appl. Phys. Lett.* **1998,** *73*, 2363.

(5) Oepts, W.; Verhagen, H. J.; Coehoorn, R.; Jonge, W. J. M. d. *J. Appl. Phys.* **1999,** *86*, 3863.

(6) Shiga, K.; Komori, J.; Katsumata, M.; Teramoto, A.; Mashiko, Y. *IEICE Trans. Electron.* **1999,** *E82-C*, 589.

(7) Dumin, D. J.; Mopuri, S. K.; vanchinathan, S.; Scott, R. S.; Subramoniam, R.; Lewis, T. G. *IEEE Trans. Electron Devices* **1995,** *42*, 760.

(8) Yamada, H.; Makino, T. *Appl. Phys. Lett.* **1991,** *59*, 2159.

(9) Fukuda, H.; Yasuda, M.; Iwabuchi, T. *Electronics Letters* **1992,** *28*, 1516.

(10) Hao, M.-Y.; Chen, W.-M.; Lai, K.; Lee, J. C.; Gaedner, M.; Fulford, J. *Appl. Phys. Lett.* **1995,** *66*, 1126.

(11) Eriguchi, K.; Niwa, M. *Appl. Phys. Lett.* **1998,** *73*, 1985.

(12) Chen, C.-C.; Chang, C.-Y.; chien, C.-H.; Huang, T.-Y.; Lin, H.-C.; Liang, M.-S. *Appl. Phys. Lett.* **1999,** *74*, 3708.

(13) Jackson, J. C.; Robinson, T.; Oralkan, O.; Dumin, D. J. *J. Electrochem. Soc.* **1998,** *145*, 1033.

(14) Verwij, J. F.; Klootwijk, J. H. *Microelectronics journal* **1996,** *27*, 611.

(15) Nissan-Cohen, Y.; Shappir, J.; Frohman-bentchkowsky, D. *Appl. Phys. Lett.* **1984,** *44*, 417.

(16) Kolodzey, J.; Chowdhury, E. A.; Adam, T. N.; Qui, G.; Rau, I.; Olowolafe, J. O.; Suehle, J. S.; Chen, Y. *IEEE Trans. Electron Devices* **2000,** *47*, 121.

(17) Ono, M.; Saito, M.; Yoshitomi, T.; Fiegna, C.; Ohguro, T.; Momose, H. S.; Iwai, H. *J. Vac. Sci. Technol. B* **1995,** *13*, 1740.

(18) Kasap, S. O. *Principles of Electrical Engineering Materials and Devices, p.539*; McGraw-Hill, 2000.

(19) Runyan, W. R.; Bean, K. E. *Semiconductor integrated circuit processing technology, p.63*; Addison-Wesley Publishing Company, Inc, 1990.

(20) Park, B. G.; Lee, T. D. *IEEE Trans. on Magnetics* **1999,** *35*, 2919.

(21) Miyazaki, T.; Tezuka, N. *J. Magn. Magn. Mater.* **1995,** *139*, L231.

(22) Metikos-Hukovic, M.; Omanovic, S. *Mat. Chem. Phys.* **1994,** *38*, 55.

(23) Lohrengel, M. M. *Material science and engineering* **1993,** *R11*, 243.

(24) Xu, Y.; Wang, M.; Pikering, H. W. , Toronto 1992; The Electrochemical Society, Inc.; 467.

(25) Sullivan, J. P.; Dunn, R. G.; Barbour, J. C.; Wall, F. D.; Missert, N.; Buchheit, R. G. , Toronto 2000; The Electrochemical Society, Inc.; 24.

(26) Addepalli, S. G.; Ekstrom, B.; Magtoto, N. P.; Lin, J. S.; Kelber, J. A. *Surf. Sci.* **1999,** *442*, 385.

(27) Street, S. C.; Xu, C.; Goodman, D. W. *Annu. Rev. Phys. Chem.* **1997,** *48*, 43.

(28) Gallagher, M. C.; Fyfield, M. S.; Cowin, J. P.; Joyce, S. A. *Surf. Sci.* **1995,** *339*, L909.

(29) Rosenhahn, A.; Schneider, J.; Becker, C.; Wandelt, K. *Appl. Surf. Sci.* **1999,** *142*, 169.

(30) Fukano, Y.; Sugawara, Y.; Yamanishi, Y.; Oasa, T.; Morita, S. *jpn. J. Appl. Phys.* **1993,** *32*, 290.

(31) Watanabe, H.; Fujita, K.; Ichikawa, M. *Appl. Phys. Lett.* **1998,** *72*, 1987.

(32) Yasue, T.; Yoshida, Y.; koyama, H.; Kato, T.; Nishioka, T. *J. Vac. Sci. Technol.* **1997,** *B15*, 1884.

(33) Watanabe, H.; Baba, T.; Ichikawa, M. *J. Appl. Phys.* **1999,** *85*, 6704.

(34) Jaeger, R. M.; Kuhlenbeck, H.; Freund, H.-J.; Wuttig, M.; Hoffman, W.; Franchy, R.; Ibach, H. *Surf. Sci.* **1991,** *259*, 235.

(35) Bardi, U.; Atrei, A.; Rovida, G. *Surf. Sci.* **1992,** *268*, 87.

(36) Becker, C.; Kandler, J.; Raaf, H.; Linke, R.; Pelster, T.; Draeger, M.; Tanemura, M.; Wandelt, K. *J. Vac. Sci. and Technol.* **1998,** *A16*, 1000.

(37) Blum, R. P.; Niehus, H. *Appl. Phys. A* **1998,** *66*, S529.

(38) Franchy, R.; Masuch, J.; Gassmann, P. *Appl. Surf. Sci.* **1996,** *93*, 317.

(39) Klimenkov, M.; Nepijko, S.; Kuhlenbeck, H.; Freund, H.-J. *Surf. Sci.* **1997,** *385*, 66-76.

(40) Viefhaus, H.; Roux, J. P.; Grabke, H. J. *Fresenius J. Anal. Chem.* **1993,** *346*, 69-74.

(41) Libuda, J.; Winkelmann, F.; Baeumer, M.; Freund, H.-J.; Bertrams, T.; Neddermeyer, H.; Mueller, K. *Surf. Sci.* **1994,** *318*, 61-73.

(42) Bertrams, T.; Brodde, A.; Neddermeyer, H. *J. Vac. Sci. Technol.* **1994,** *B12*, 2122.

(43) Jennison, D. R.; Verdozzi, C.; Schultz, P. A.; Sears, M. P. *Phys. Rev.* **1999,** *B59*, R15605.

(44) Ermakov, A. V.; Adamchuk, V. K. *Tech. Phys. Lett.* **1999,** *25*, 200.

(45) Sullivan, J. P.; Barbour, J. C.; Dunn, R. G.; Son, K.-A.; Montes, L. P.; Missert, N.; Copeland, R. G. , Boston, Massachusetts 1998; The Electrochemical Society, Inc.; 111.

(46) Lin, L. F.; Chao, C. Y.; MacDonald, D. D. *J. Electrochem. Soc.* **1981,** *128*, 1194.

(47) Akpati, H. C.; Nordlander, P.; Lou, L.; Avouris, P. *Surf. Sci.* **1997,** *372*, 9.

(48) Jennison, D. R.; Sullivan, J. P.; Schultz, P. A.; Sears, M. P.; Stechel, E. B. *Surf. Sci.* **1997,** *390*, 112.

(49) Hohenberg, P.; Kohn, W. *Phys. Rev. B* **1964,** *136*, B864.

(50) Kohn, W.; Sham, L. J. *Phys. Rev. A* **1965,** *140*, A1133.

(51) Perdew, J. P.; Chevary, J. A.; Vosko, S. H.; Jackson, K. A.; Pederson, M. R.; Singh, D. J.; Fiolhais, C. *Phys. Rev. B* **1992,** *46*, 6671.

(52) Kresse, G.; Hafner, J. *Phys. Rev. B* **1993,** *47*, 558.

(53) Kresse, G.; Hafner, J. *Phys. Rev. B* **1994,** *49*, 14251.

(54) Kresse, G.; Hafner, J. *Phys. Rev. B* **1996,** *54*, 11169.

(55) Vanderbilt, D. *Phys. Rev. B* **1985,** *32*, 8412.

(56) Vanderbilt, D. *Phys. Rev. B* **1990,** *41*, 7892.

(57) Rosenhahn, A.; Schneider, J.; Kandler, J.; Becker, C.; Wandelt, K. *Surf. Sci.* **1999,** *433-435*, 705.

(58) Popova, I.; Zhukov, V.; Jr., J. T. Y. *J. Appl. Phys.* **2000,** *87*, 8143.

(59) Stierle, A.; Formoso, V.; Comin, F.; Franchy, R. *Sur. Sci.* **2000,** *467*, 85.

(60) Yourdshahyan, Y.; Ruberto, C.; Halvarsson, M.; Bengtsson, L.; Langer, V.; Lundqvist, B. I.; Ruppi, S.; Rolander, U. *J. Am. Ceram. Soc.* **1999,** *82*, 1365.

(61) Jennison, D. R.; Bogicevic, A. *Surf. Sci.* **2000,** *464*, 108.

(62) Bogicevic, A.; Jennison, D. R. *Phys. Rev. Lett.* **1999,** *82*, 4050.

(63) Formino, M.; Hebert, K. R.; Asoka-Kumar, P.; Lynn, K. G. , Toronto 2000; The Electrochemical Society, Inc.; 642.

(64) Xu, Y.; Wang, M.; Pickering, H. W. *J. Electrochem. Soc.* **1993,** *140*, 3448.

(65) Marcus, P.; Herbelin, J.-M. *Corros. Sci.* **1993,** *34*, 1123.

REFERENCE LIST

Adamson, A. W. *Physical Chemistry of Surfaces*, 3 ed.; John Wiley and Sons: New York, 1976.

Addepalli, S. G. L.in, J.-S.; Kelber, J.A. *Oxid. Met.* 1999, *52*, 139.

Addepalli, S. G.; Ekstrom, B.; Magtoto, N. P.; Lin, J. S.; Kelber, J. A. *Surf. Sci.* 1999, *442*, 385.

Addepalli, S. G.; Magtoto, N. P.; Kelber, J. A. *Surf. Sci.* 2000, *458*, 123.

Ahn, J.; Rabalais, J. W. *Surf. Sci.* 1997, *388*, 121-131.

Akpati, H. C.; Nordlander, P.; Lou, L.; Avouris, P. *Surf. Sci.* 1997, *372*, 9.

Argile, C.; Rhead, G. E. *Surf. Sci. Rep.* 1989, *10*, 277.

Baglin, J. E. E. *Nucl. Instrum. Meth. Phys. Res. B* 1989, *39*, 764.

Bardi, U.; Atrei, A.; Rovida, G. *Surf. Sci.* 1992, *268*, 87.

Barr, T. L. *J. Vac. Sci. Technol. A* 1989, *7*, 1677-1683.

Bauer, E.; Poppa, H.; Todd, G.; Bonczek, F. *J. Appl. Phys.* 1974, *45*, 5164.

Baumer, M.; Freund, H.-J. *Prog. Surf. Sci.* 1999, *61*, 127.

Becker, C.; Kandler, J.; Raaf, H.; Linke, R.; Pelster, T.; Draeger, M.; Tanemura, M.; Wandelt, K. *J. Vac. Sci. and Technol.* 1998, *A16*, 1000.

Bertrams, T.; Brodde, A.; Neddermeyer, H. *J. Vac. Sci. Technol.* 1994, *B12*, 2122.

Besenbacher, F. *Rep. Prog. Phys.* 1996, *59*, 1737.

Betrabet, H. S.; Reddy, S. N. S.; Purushothaman, S. *Ceramic Eng. Sci. Proc.* 1989, *10*, 1531.

Binnig, G.; Rohrer, H. *IBM J.Res. Dev.* 1986, *30*, 355.

Binnig, G.; Rohrer, H.; Gerber, C.; Weibel, E. *Phys. Rev. Lett.* 1982, *49*, 57.

Blum, R. P.; Niehus, H. *Appl. Phys. A* 1998, *66*, S529.

Blum, R.-P.; Ahlberendt, D.; Niehus, H. *Surf. Sci.* 1998, *396*, 176.

Bogicevic, A.; Jennison, D. R. *Phys. Rev. Lett.* 1999, *82*, 4050.

Bogicevic, A.; Jennison, D. R. *Surf. Sci.* 1999, *437*, L741.

Briggs, D.; Seah, M. P. ; John Wiley & Sons: Chichester, 1983; Vol. 1.

Campbell, C. T. *(unpublished results)* .

Campbell, C. T. *Surf. Sci. Rep.* 1997, *27*, 1.

Carley, A. F.; Rajumon, M. K.; Roberts, M. W. *J. Solid State Chem.* 1993, *106*, 156-163.

Castro, V. D.; Polzonetti, G.; Zanoni, R. *Surf. Sci.* 1985, *162*, 348.

Cazaux, J.; Lehuede, P. *J. Electron Spectrosc. Relat. Phenom.* 1992, *59*, 49-71.

Ceperley, D. M.; Alder, B. J. *Phys. Rev. Lett.* 1980, *45*, 566.

Chen, C.-C.; Chang, C.-Y.; chien, C.-H.; Huang, T.-Y.; Lin, H.-C.; Liang, M.-S. *Appl. Phys. Lett.* 1999, *74*, 3708.

Chen, J. G.; Colaianni, M. L.; Weinberg, W. H.; Yates, J.T. Jr. *Surf. Sci.* 1992, *279*, 223-232.

Chen, L.; Magtoto, N. P.; Kelber, J. A. *Oxid. Met.* 2000, *54*, 285.

Cotterill, G. F.; Niehus, H.; O'Connor, D. J. *Surf. Rev. Lett.* 1966, *3*, 1355.

Dake, L. S.; Lad, R. J. *J. Vac. Sci. Technol.* 1995, *A13*, 122.

Dake, L. S.; Lad, R. J. *Sur. Sci.* 1993, *289*, 297.

Diebold, U.; Pan, J. M.; Madey, T. E. *Physi. Rev.* 1993, *B47*, 3868.

Dumin, D. J.; Mopuri, S. K.; vanchinathan, S.; Scott, R. S.; Subramoniam, R.;

Lewis, T. G. *IEEE Trans. Electron Devices* 1995, *42*, 760.

Elam, J. W.; Nelson, C. E.; Cameron, M. A.; Tolber, M. A.; George, S. M. *J. Phys. Chem. B* 1998, *102*, 7008-7015.

Eng, P. J.; Trainor, T. P.; Brown, G. E.; Waychunas, G. A.; Newville, M.; Sutton, S. R.; Rivers, M. L. *Science* 2000, *288*, 1029-1033.

Eriguchi, K.; Niwa, M. *Appl. Phys. Lett.* 1998, *73*, 1985.

Ermakov, A. V.; Adamchuk, V. K. *Tech. Phys. Lett.* 1999, *25*, 200.

Ernst, N.; Duncomb, B.; Bozdech, G.; Naschitzki, M.; Freund, H. J. *Ultramicroscopy* 1999, *in press*.

Ertl, G.; Freund, H.-J. *Physics Today* 1999, *52*, 32-38.

Ertl, G.; Kuppers, J. *Low Energy Electrons and Surface Chemistry*; Verlag Chemie: Weinheim, 1974.

Eumann, E.; Schmitz, G.; Franchy, R. *Appl. Phys. Lett.* 1998, *72*, 3440.

Fan, J. C. C.; Henrich, V. E. *Appl. Phys. Lett.* 1974, *25*, 410.

Feenstra, R. M.; Stroscio, J. A.; Fein, A. P. *Surf. Sci.* 1987, *181*, 295.

Feldman, L. C.; Mayer, J. W. *Fundamentals of Surface and Thin Film Analysis*; P T R Prentice-Hall, Inc.: Englewood Cliffs, NJ, 1986.

Fleisch, T. H.; Mains, G. J. *Appl. Surface Sci.* 1982, *10*, 51-62.

Fomino, M.; Hebert, K. R.; Asoka-Kumar, P.; Lynn, K. G. *Electrochemical Society Proceedings* 1998, *98-17*, 642.

Formino, M.; Hebert, K. R.; Asoka-Kumar, P.; Lynn, K. G. , Toronto 2000; The Electrochemical Society, Inc.; 642.

Fowkes, F. M. In *Surfaces and Interfaces I*; Burke, J. J., Ed.; Syracuse University Press: New York, 1967, pp 197.

Franchy, R. *Surf. Sci. Rep.* 2000, *38*, 195.

Franchy, R.; Masuch, J.; Gassmann, P. *Appl. Surf. Sci.* 1996, *93*, 317.

Frederick, B. G.; Apai, G.; Rhodin, T. N. *Surf. Sci.* 1992, *277*, 337.

Freund, H. J.; Kuhlenbeck, H.; Staemmler, V. *Rep. Progr. Phys.* 1996, *59*, p. 283.

Fukano, Y.; Sugawara, Y.; Yamanishi, Y.; Oasa, T.; Morita, S. *jpn. J. Appl. Phys.* 1993, *32*, 290.

Fukuda, H.; Yasuda, M.; Iwabuchi, T. *Electronics Letters* 1992, *28*, 1516.

Gallagher, M. C.; Fyfield, M. S.; Cowin, J. P.; Joyce, S. A. *Surf. Sci.* 1995, *339*, L909.

Gautier, M.; Duraud, J. P.; Van, L. P. *Surf. Sci. Lett.* 1991, *249*, L327-L332.

Gautier, M.; Van, L. P.; Duraud, J. P. *Europhys. Lett.* 1992, *18*, 175-180.

Golden, D. A. *(Personal communication).*

Gota, S.; Gautier, M.; Douillard, L.; Thromat, N.; Duraud, J. P.; Fevre, P. L. *Surf. Sci.* 1995, *323*, 163-174.

Graupner, H.; Hammer, L.; Heinz, K.; Zehner, D. M. *Surf. Sci.* 1997, *380*, 335.

Guo, Q.; Moller, P. J. *Surf. Sci.* 1991, *244*, 228-236.

Guo, Q.; Moller, P. J.; Gui, L. *Acta Physica Polonica A* 1992, *81*, 647-651.

Hamers, R. J.; Tromp, R. M.; Demuth, J. E. *Phys. Rev. Lett.* 1986, *56*, 1972.

Hao, M.-Y.; Chen, W.-M.; Lai, K.; Lee, J. C.; Gaedner, M.; Fulford, J. *Appl. Phys. Lett.* 1995, *66*, 1126.

Hass, K. C.; Schneider, W. F.; Curioni, A.; Andreoni, W. *Science* 1998, *282*, 265-268.

Henrich, V. E.; Cox, P. A. *The surface science of metal oxides*; Cambridge university press, 1994.

Henry, C. R. *Surf. Sci. Rep.* 1998, *31*, 231.

Hohenberg, P.; Kohn, W. *Phys. Rev. B* 1964, *136*, B864.

Imaduddin, A.; Lad, R. J. *Sur. Sci.* 1993, *290*, 35.

Jackson, J. C.; Robinson, T.; Oralkan, O.; Dumin, D. J. *J. Electrochem. Soc.* 1998, *145*, 1033.

Jaeger, R. M.; Kuhlenbeck, H.; Freund, H.-J.; Wuttig, M.; Hoffman, W.; Franchy, R.; Ibach, H. *Surf. Sci.* 1991, *259*, 235.

Jennison, D. R.; Bogicevic, A. *Surf. Sci.* 2000, *464*, 108.

Jennison, D. R.; Sullivan, J. P.; Schultz, P. A.; Sears, M. P.; Stechel, E. B. *Surf. Sci.* 1997, *390*, 112.

Jennison, D. R.; Verdozzi, C.; Schultz, P. A.; Sears, M. P. *Phys. Rev.* 1999, *B59*, R15605.

Johnson, K. H.; Pepper, S. V. *J. Appl. Phys.* 1982, *83*, 6634.

Kasap, S. O. *Principles of Electrical Engineering Materials and Devices, p.539*; McGraw-Hill, 2000.

Kelber, J. A.; Niu, C.; Shepherd, K.; Jennison, D. R.; Bogicevic, A. *Surf. Sci.* 2000, *446*, 76-88.

Keller, D. V. In *Surfaces and Interfaces I*; Burke, J. J., Ed.; Syracuse University Press: New York, 1967, pp 225.

Klimenkov, M.; Nepijko, S.; Kuhlenbeck, H.; Freund, H.-J. *Surf. Sci.* 1997, *385*, 66-76.

Kohn, W.; Sham, L. J. *Phys. Rev. A* 1965, *140*, A1133.

Kolodzey, J.; Chowdhury, E. A.; Adam, T. N.; Qui, G.; Rau, I.; Olowolafe, J. O.; Suehle, J. S.; Chen, Y. *IEEE Trans. Electron Devices* 2000, *47*, 121.

Kresse, G.; Hafner, J. *Phys. Rev. B* 1993, *47*, 558.

Kresse, G.; Hafner, J. *Phys. Rev. B* 1994, *49*, 14251.

Kresse, G.; Hafner, J. *Phys. Rev. B* 1996, *54*, 11169.

Lad, R. J. *Surf. Rev. Lett.* 1995, *2*, 109-126.

Libuda, J.; Frank, M.; Sandell, A.; Anderson, S.; Bruhwiler, P. A.; Baumer, M.; Martensson, N.; Freund, H.-J. *Surf. Sci.* 1997, *384*, 106.

Libuda, J.; Winkelmann, F.; Baeumer, M.; Freund, H.-J.; Bertrams, T.; Neddermeyer, H.; Mueller, K. *Surf. Sci.* 1994, *318*, 61-73.

Lide, D. R.; Frederikse, H. P. R. ; CRC Press: Ann Arbor, MI, 1993.

Lin, L. F.; Chao, C. Y.; MacDonald, D. D. *J. Electrochem. Soc.* 1981, *128*, 1194.

Liu, P.; Kendelewicz, T.; G.E. Brown, J.; Nelson, E. J.; Chambers, S. A. *Surf. Sci.* 1998, *417*, 53-65.

Lohrengel, M. M. *Material science and engineering* 1993, *R11*, 243.

Magtoto, N. P.; Niu, C.; Anzaldua, M.; Kelber, J. A.; Jennison, D. R. *Surf. Sci.* 2001, *472*, L157.

Magtoto, N. P.; Niu, C.; Ekstrom, B.; Addepalli, S.; Kelber, J. A. *Appl. phys. Lett.* 2000, *77*, 2228.

Marcus, P.; Herbelin, J.-M. *Corros. Sci.* 1993, *34*, 1123.

Martini, D.; Shepherd, K.; Sutcliffe, R.; Kelber, J. A.; Edwards, H.; Martin, R. S. *Apllied Surf. Sci.* 1999, *141*, 89-100.

Mayer, J. W.; Lau, S. S. *Electronic Materials Science: for Integrated Circuits in Si and GaAs*; Macmillan Publishing Company: New York, 1990.

McHale, J. M.; Auroux, A.; Perrotta, A. J.; Navrotsky, A. *Science* 1997, *277*, 788-791.

Metikos-Hukovic, M.; Omanovic, S. *Mat. Chem. Phys.* 1994, *38*, 55.

Miyazaki, T.; Tezuka, N. *J. Magn. Magn. Mater.* 1995, *139*, L231.

Moller, P. J.; Guo, Q. *Thin Solid Films* 1991, *201*, 267-279.

Moller, P. J.; Wu, M. C. *Surf. Sci.* 1989, *224*, 250.

Morrison, S. R. *The Chemical Physics of Surfaces*; Plenum Press: New York, 1990.

Moulder, J. F.; Stickle, W. F.; Sobol, P. E.; Bomben, K. D.; Chastain, J.; King, R. C. *Handbook of X-ray photoelectron spectroscopy*; Physical Electronics, Inc.: Eden Prairie, Minnesota, 1995.

Murarka, S. P. *Metallization: Theory and Practice for VLSI and ULSI*; Butterworth-Heinemann: Stoneham, MA, 1993.

Nakamura, J.; Rodriguez, J. A.; Campbell, C. T. *J. Condens. Matter* 1989, *1*, SB149.

National Technology Roadmap for Semiconductors; Semiconductor Industry Association: San Jose, CA, 1997.

Nelson, C. E.; Elam, J. W.; Cameron, M. A.; Tolbert, M. A.; George, S. M. *Surf. Sci.* 1998, *416*, 341-353.

Nissan-Cohen, Y.; Shappir, J.; Frohman-bentchkowsky, D. *Appl. Phys. Lett.* 1984, *44*, 417.

Nix, R. M. *An Introduction to Surface Chemistry*; http://www.chem.qmw.ac.uk/surfaces/scc/sccinfo.htm, 1997.

Oepts, W.; Verhagen, H. J.; Coehoorn, R.; Jonge, W. J. M. d. *J. Appl. Phys.* 1999, *86*, 3863.

Oepts, W.; Verhagen, H. J.; Jonge, W. J. M. d.; Coehoorn, R. *Appl. Phys. Lett.* 1998, *73*, 2363.

Ohuchi, F. S.; French, R. H.; Kasowski, R. V. *J. Appl. Phys.* 1987, *62*, 2286-2289.

Ohuchi, F. S.; Kohyama, M. *J. Am. Ceram. Soc.* 1991, *74*, 1163.

Ono, M.; Saito, M.; Yoshitomi, T.; Fiegna, C.; Ohguro, T.; Momose, H. S.; Iwai, H. *J. Vac. Sci. Technol. B* 1995, *13*, 1740.

Pan, J. M.; Diebold, U.; Zhang, L.; Madey, T. E. *Surf. Sci.* 1993, *295*, 411.

Pan, J.-M.; Madey, T. E. *J. Vac. Sci. Technol.* 1993, *A11*, 1667.

Pan, J.-M.; Maschhoff, B. L.; Diebold, U.; Madey, T. E. *Surf. Sci.* 1993, *291*, 381.

Park, B. G.; Lee, T. D. *IEEE Trans. on Magnetics* 1999, *35*, 2919.

Parmaliana, A.; Arena, F.; Frusteri, F. *J. Chem. Soc. Faraday Trans.* 1990, *86*, 2663.

Peden, C. H. F.; Kidd, K. B.; Shinn, N. D. *J. Vac. Sci. Technol. A* 1991, *9*, 1518.

Perdew, J. P.; Chevary, J. A.; Vosko, S. H.; Jackson, K. A.; Pederson, M. R.; Singh, D. J.; Fiolhais, C. *Phys. Rev. B* 1992, *46*, 6671.

Perdew, J. P.; Zunger, A. *Phys. Rev. B* 1981, *23*, 5048.

Pertsin, A. J.; Pashunin, Y. M. *Applied Surf. Sci.* 1990, *44*, 171-178.

Pijpers, A. P.; Berreshelm, K.; Wilmers, M. *Fresenius J. Anal. Chem.* 1993, *346*, 104-109.

Pint, B. A. *Oxid. Met.* 1997, *48*, 303.

Popova, I.; Zhukov, V.; Jr., J. T. Y. *J. Appl. Phys.* 2000, *87*, 8143.

Powell, C. J. *Surf. Interface Anal.* 1995, *23*, 121.

Rosenhahn, A.; Schneider, J.; Becker, C.; Wandelt, K. *Appl. Surf. Sci.* 1999, *142*, 169.

Rosenhahn, A.; Schneider, J.; Kandler, J.; Becker, C.; Wandelt, K. *Surf. Sci.* 1999, *433-435*, 705.

Runyan, W. R.; Bean, K. E. *Semiconductor integrated circuit processing technology, p.63*; Addison-Wesley Publishing Company, Inc, 1990.

Schmitz, G.; Gassmann, P.; Franchy, R. *J. Appl. Phys.* 1998, *83*, 2533.

Seshadri, G. X., H.-C.; Kelber, J. A. *J. Electrochem. Soc.* 1999, *146*, 1762.

Shiga, K.; Komori, J.; Katsumata, M.; Teramoto, A.; Mashiko, Y. *IEICE Trans. Electron.* 1999, *E82-C*, 589.

Somorjai, G. A. *Chemistry in Two Dimensions: Surfaces*; Cornell University Press: Ithaca, NY, 1981.

Somorjai, G. A. *Introduction to surface chemistry and catalysis*; John Wiley & Sons, Inc., 1994.

Stierle, A.; Formoso, V.; Comin, F.; Franchy, R. *Sur. Sci.* 2000, *467*, 85.

Stott, F. H. *Rep. Progr. Phys.* 1987, *50*, 861.

Street, S. C.; Xu, C.; Goodman, D. W. *Annu. Rev. Phys. Chem.* 1997, *48*, 43.

Strongin, D. R.; Bare, S. R.; Somorjai, G. A. *J. Catal.* 1987, *103*, 289.

Stroscio, J. A.; Feenstra, R. M.; Fein, A. P. *Phys. Rev. Lett.* 1986, *57*, 2579.

Stroscio, J. A.; Kaiser, W. J. In *Methods of Experimental Physics*; Celotta, R., Lucatorto, T., Eds.; Academic Press, Inc.: San Diego, 1993; Vol. 27.

Sullivan, J. P.; Barbour, J. C.; Dunn, R. G.; Son, K.-A.; Montes, L. P.; Missert, N.; Copeland, R. G. , Boston, Massachusetts 1998; The Electrochemical Society, Inc.; 111.

Sullivan, J. P.; Dunn, R. G.; Barbour, J. C.; Wall, F. D.; Missert, N.; Buchheit, R. G. , Toronto 2000; The Electrochemical Society, Inc.; 24.

Sushumna, I.; Ruckenstein, E. *J. Catal.* 1985, *94*, 239.

Vanderbilt, D. *Phys. Rev. B* 1985, *32*, 8412.

Vanderbilt, D. *Phys. Rev. B* 1990, *41*, 7892.

Varma, S.; Chottiner, G.; Arbab, M. *J. Vac. Sci. Technol. A* 1992, *10*, 2857-2862.

Verdozzi, C.; Jennison, D. R.; Schultz, P. A.; Sears, M. P. *Phys. Rev. Lett.* 1999, *82*, 799-802.

Verwij, J. F.; Klootwijk, J. H. *Microelectronics journal* 1996, *27*, 611.

Viefhaus, H.; Roux, J. P.; Grabke, H. J. *Fresenius J. Anal. Chem.* 1993, *346*, 69-74.

Vijayakrishnan, V.; Rao, C. N. R. *Surf. Sci. Lett.* 1991, *255*, L516-L522.

Wandelt, K. *Surf. Sci. Rep.* 1982, *2*, 1.

Wang, M.-H.; Hebert, K. R. *J. Electrochem. Soc.* 1999, *146*, 3741.

Watanabe, H.; Baba, T.; Ichikawa, M. *J. Appl. Phys.* 1999, *85*, 6704.

Watanabe, H.; Fujita, K.; Ichikawa, M. *Appl. Phys. Lett.* 1998, *72*, 1987.

Wiesendanger, R. *Scanning Probe Microscopy and Spectroscopy: Methods and Applications*; Cambridge University Press: Cambridge, UK, 1994.

Wit, H. d.; Fransen, T. In *The CRC handbook of Solid State Electrochemistry*; Gellings, P. J., Bouwmeester, H. J. M., Eds., 1997.

Wu, M.-C.; Goodman, D. W. *J. Phys. Chem.* 1994, *98*, 9874-9881.

Wu, Y.; Garfunkel, E.; Madey, T. E. *J. Vac. Sci Technol. A* 1996, *14*, 1662-1667.

Wu, Y.; Garfunkel, E.; Madey, T. E. *J. Vac. Sci. Technol. A* 1996, *14*, 2554-2563.

Xu, Y.; Wang, M.; Pickering, H. W. *J. Electrochem. Soc.* 1993, *140*, 3448.

Xu, Y.; Wang, M.; Pikering, H. W. , Toronto 1992; The Electrochemical Society, Inc.; 467.

Yamada, H.; Makino, T. *Appl. Phys. Lett.* 1991, *59*, 2159.

Yasue, T.; Yoshida, Y.; koyama, H.; Kato, T.; Nishioka, T. *J. Vac. Sci. Technol.* 1997, *B15*, 1884.

Yourdshahyan, Y.; Ruberto, C.; Halvarsson, M.; Bengtsson, L.; Langer, V.; Lundqvist, B. I.; Ruppi, S.; Rolander, U. *J. Am. Ceram. Soc.* 1999, *82*, 1365.

Yu, X.; Hantsche, H. *Surf. Interface Anal.* 1993, *20*, 555-558.

Zhang, L.; Persaud, R.; Madey, T. E. *Phys. Rev. B* 1997, *56*, 549.

Zhang, Z. *Surf. Sci.* 1992, *277*, 263.

Zhao, X. A.; Kolawa, E.; Nicolet, M. A. *J. Vac. Sci. Technol.* 1986, *A4*, 3139.

Zhong, Q.; Ohuchi, F. S. *J. Vac. Sci. Technol.* 1990, *A8*, 2107.

Zhou, J. B.; Gustafsson, T.; Garfunkel, E. *Surf. Sci.* 1997, *372*, 21.